UNIVERSITY of CALIFORNIA

Santa Barbara

Texture evolution during thermomechanical processing in rare earth free magnesium alloys

A Dissertation submitted in partial satisfaction of the

requirements for the degree

Doctor of Philosophy

in

Materials

by

Victoria Mayne Miller

Committee in charge:

Professor Tresa M. Pollock, Chair

Professor Carlos G. Levi

Professor G. Robert Odette

Professor Frederic Gibou

June 2016

The dissertation of Victoria Mayne Miller is approved.

Professor Carlos G. Levi

Professor G. Robert Odette

Professor Frederic Gibou

Professor Tresa M. Pollock, Committee Chair

May 2016

Texture evolution during thermomechanical processing in rare earth free magnesium alloys

by

Victoria Mayne Miller

dedicated to my academic family

Acknowledgements

My journey in science has taken a vastly different path than I would ever have considered, a path that has been filled with challenges and the occasional profound struggle. However, at every stage I have had wonderful allies who have provided support, instruction, and inspiration. With their help, I have grown tremendously both as a researcher and as a person.

First and foremost, I would like to recognize my advisor, Professor Tresa Pollock. She has continuously worked to both expand my horizons and to facilitate the resources I needed to pursue what I find exciting. Similarly, I want to thank my undergraduate research advisor (and unofficial committee member) Professor Wayne Jones. I am grateful to him for many reasons, but I want to particularly thank him for pushing me out of the nest.

On the technical side of things, many people have provided guidance. I would like to first acknowledge my committee–Professor Carlos Levi, Professor Bob Odette, and Professor Frederic Gibou–for challenging me and patiently improving my technical communication skills. I would also like recognize Professor Jian-Feng Nie for hosting my stay at Monash University and sponsoring all of the production of the Mg-Zn material. Professor Irene Beyerlein gave me a crash course in Fortran and VPSC, and has been tremendously supportive of my

ideas (even the far-fetched ones). Dr. Ray Decker and nanoMAG have aided my research for many years, providing both samples and interesting discussions. Finally, the samples and experiments described in this dissertation would not exist without the phenomenal technical expertise of Chris Torbet, Daniel Curtis, and Daniel East.

Many fellow students and post-docs (both at UCSB and earlier at University of Michigan) both taught me new aspect of research and helped to keep me sane. This is particularly true of the Pollock group, especially my very tolerant officemates Dr. Mike Titus, Dr. J.C. Stinville, and Luke Rettberg, as well as Tom Nizolek, who I could always count on to be the other person at lab after midnight. I would also like to thank my graduate research mentor from Michigan, Dr. Tracy Berman, who helped me learn to frame a research project. I also need to express my gratitude to my phenomenal undergraduate research assistant Alex Selimov; I am excited to see where his career takes him.

While not directly involved in my dissertation work, numerous other faculty have consistently gone above and beyond to provide mentorship. Professor Sam Daly always made time to help provide context and advice on the academic job search and work-life balance. Professor Suveen Mathaudhu has always made a point to advocate for me loudly and publicly, ensuring that I always get a seat at the table.

Finally, I want to acknowledge two people who I encountered much earlier in my scientific career but who were instrumental to my success. First, I want to thank Lynn Hensley, my high school chemistry teacher, who helped me apply to the ASM Eisenman Materials Science Camp when I was fourteen. I left that five day camp having fallen in love with metallurgy, and determined to build a career in field. She later also facilitated my internship at Ford Motor Company, where I met James.

Dr. James Boileau at Ford Motor Company put the first magnesium sample in my hand almost a decade ago and sparked a fascination that would not end. He helped me select where I went to undergrad, where I worked during the summers, and also played his own role in pushing me out of the nest. He treated me as an adult and as a colleague from Day 1, even though I was sixteen years old when we met. That independence was empowering, and got me through personal difficulties I could not have otherwise faced.

Curriculum Vitæ

Victoria Mayne Miller

Education

2011–2016 Ph.D. in Materials, University of California, Santa Barbara, CA, USA.

2008–2011 B.S.E. in Materials Science and Engineering, University of Michigan, Ann Arbor, MI, USA.

Publications

11. **V.M. Miller** *et al.*. "Deformation texture modification by intermetallic particle distribution in binary Mg-Zn alloys." In preparation.
10. **V.M. Miller** *et al.*. "Recrystallization texture modification as a function of temperature in a binary Mg-Zn alloy." In preparation.
9. **V.M. Miller** *et al.*. "Polycrystal plasticity simulation of the effect of microtexture on the deformation of titanium alloys." In preparation.
8. L.H. Rettberg, **V.M. Miller**, J.C. Stinville, and T.M. Pollock. "Extended Duration Transverse Creep of Directionally Solidified Nickel-Base Superalloy

GTD444," to be submitted June 2016.

7. J.C. Stinville, M.P. Echlin, **V.M. Miller**, and T.M. Pollock. "Measurement of Fatigue Strain Localization in Nickel-Base Superalloys," to be submitted May 2016.

6. J.C. Stinville, M.P. Echlin, W.C. Lenthe, D. Texier, **V.M. Miller**, N. Vanderesse, F. Bridier, J. Miao, P. Bocher, and T.M. Pollock. "Strain Localization and Fatigue Initiation in a Nickel Base Superalloy," to be submitted May 2016.

5. M.P. Echlin, J.C. Stinville, **V.M. Miller**, W. Lenthe, T.M. Pollock. "Long range plastic strain localization and slip activity in microtextured Ti-6Al-4V." Under review.

4. **V.M. Miller**, T.D. Berman, I.J. Beyerlein, and T.M. Pollock. "Polycrystal plasticity simulation for the prediction of forming behavior in magnesium alloys," submitted December 2015. Under Review.

3. **V.M. Miller** and T.M. Pollock, "Texture Modification in a Magnesium-Aluminum-Calcium Alloy During Uniaxial Compression," *Metallurgical and Materials Transactions A*. 47(4), 1854-1864. [**doi**]

2. **V.M. Miller**, A.E. Johnson, C.J. Torbet, and T.M. Pollock. "Recrystallization and the development of abnormally large grains after small strain de-

formation in a polycrystalline nickel-based superalloy," *Metallurgical and Materials Transactions A*. 47(4), 1566-1574. [**doi**]

1. J. E. Douglas, C. S. Birkel, N. Verma, **V. M. Miller**, M.-S. Miao, G. D. Stucky, T. M. Pollock, and R. Seshadri, "Phase stability and property evolution of biphasic Ti-Ni-Sn alloys for use in thermoelectric applications," *J. Appl. Phys.* **115**, 043720 (2014).[**doi**]

Abstract

Texture evolution during thermomechanical processing in rare earth free magnesium alloys

by

Victoria Mayne Miller

The use of wrought magnesium alloys is highly desirable for a wide range of applications where low component weight is desirable due to the high specific strength and stiffness the alloys can achieve. However, the implementation of wrought magnesium has been hindered by the limited room temperature formability which typically results from deformation processing. This work identifies opportunities for texture modification during thermomechanical processing of conventional (rare earth free) magnesium alloys via a combination of experimental investigation and polycrystal plasticity simulations.

During deformation, it is observed that a homogeneous distribution of coarse intermetallic particles efficiently weakens deformation texture at all strain levels, while a highly inhomogeneous particle distribution is only effective at high strains. The particle deformation effects are complemented by the addition of

alkaline earth solute, which modifies the relative deformation mode activity.

During recrystallization, grains with basal orientations recrystallize more readily than off-basal grains, despite similar levels of internal misorientation. Dislocation substructure investigations revealed that this is a result of enhanced nucleation in the basal grains due to the dominance of prismatic slip.

This dissertation identifies avenues to enhance the potential formability of magnesium alloys during thermomechanical processing by minimizing the evolved texture strength. The following are the identified key aspects of microstructural control:

- Maintaining a fine grain size, likely via Zener pinning, to favorably modify deformation mode activity and homogenize deformation.
- Developing a coarse, homogeneously distributed population of coarse intermetallic particles to promote a diffuse deformation texture.
- Minimizing the activity of prismatic slip to retard the recrystallization of grains with basal orientations, allowing the development of a more diffuse recrystallization texture.

Contents

List of Figures

List of Tables

List of Acronyms

AXJ810 Mg alloy nominally 8wt% Al 1wt% Ca and <1wt% Sr

BSE backscattered electron

CRSS critical resolved shear stress

EBSD electron backscatter diffraction

EDS energy dispersive spectroscopy

FIB focused ion beam

GND geometrically necessary dislocation

GOS grain orientation spread

GROD grain reference orientation deviation

IGMA intragranular misorientation analysis

IPF inverse pole figure

IQ image quality

JMAK Johnson-Mehl-Avrami-Kolmogorov

MGRO maximum growth rate orientation

MRD multiples of random distribution

PDZ particle deformation zone

PSN particle stimulated nucleation

RD rolling direction

RE rare earth

SEM scanning electron microscopy

SIBM strain induced boundary migration

TD transverse direction

TEM transmission electron microscopy

TTMP thixomolded and thermomechanically processed

VPSC viscoplastic self-consistent

Chapter 1

Introduction and motivation

As the lowest density class of structural metals, magnesium alloys are appealing for a wide range of applications where light weight is critical. In particular, Mg alloys have been attractive for high volume applications such as weight reduction in vehicles, where reduced vehicle weight translates to improved fuel economy. For typical passenger vehicles powered by internal combustion engines, a 10% decrease in vehicle weight translates to a 6-8% decrease in fuel consumption [2]. While cast magnesium has been commonly adopted, wrought alloys have lagged behind, at least partially due to their limited room temperature ductility. As such, they typically must be processed at elevated temperature, which results in increased component cost. In recent years, much research has

been devoted to developing strategies for improving the room temperature ductility and formability of magnesium alloys.

The primary cause of the limited ductility in Mg alloys is its hexagonal close packed (hcp) crystal structure and its limited number of slip systems, discussed further in Section 1.1. At room temperature, basal slip ($\langle a \rangle$-type dislocations in the basal (0001) plane) and tension twinning are highly dominant. However, these deformation mechanisms are insufficient to satisfy the von Mises criterion for homogeneous plastic deformation of polycrystalline materials; therefore, the alloys tend to fracture at low strain [3]. The activation of other deformation modes, particularly $\langle c + a \rangle$ slip is highly desirable, because it would greatly increase the number of independent slip systems and allow the von Mises criterion to be satisfied.

Most "conventional" magnesium alloys are based on the AZ, AM, or ZK series, indicating that the major alloying elements are aluminum and zinc, aluminum and manganese, or zinc and zirconium, respectively. More recently, the term "conventional" has been applied to any magnesium alloy that does not contain rare earth (RE) elements. Recently, numerous RE-containing alloys have been designed and studied due to their improved mechanical properties, particularly at elevated temperature, and the improved ductility and formability [3]. However, due to the high cost of RE additions these alloys are unlikely to be

implemented for high-volume consumer applications. As such, the focus of this thesis is on lower cost alloys; however, RE alloying effects on texture evolution will be reviewed in the following sections.

In the following sections, the deformation, recrystallization, and grain growth behavior of conventional magnesium alloys is discussed, accompanied by reported means to modify the standard behavior, thereby improving mechanical properties.

1.1 Deformation in Mg Alloys

Plastic deformation in magnesium alloys is accommodated by a combination of slip and twinning modes, as shown in Figures 1.1 and 1.2. The commonly reported slip systems are basal $\{0001\}\langle 2\bar{1}\bar{1}0\rangle$ slip, prismatic $\{10\bar{1}0\}\langle 2\bar{1}\bar{1}0\rangle$, and pyramidal II $\langle c+a\rangle$ $\{11\bar{2}2\}\langle\bar{1}\bar{1}23\rangle$ [3]; however, a recent study by Xie *et al.*[4] indicated that pyramidal I $\langle c+a\rangle$ $\{10\bar{1}1\}\langle\bar{1}\bar{1}23\rangle$ may be active instead of $\{11\bar{2}2\}\langle\bar{1}\bar{1}23\rangle$. Slip with a $\langle a\rangle$-type burgers vector on pyramidal is also possible, but is usually ignored because the associated deformation can be accommodated by a combination of softer basal and prismatic slip. Additionally, tension twinning $\{10\bar{1}2\}\langle\bar{1}011\rangle$ is activated at relatively low strains in most alloys. Compression and double twinning is relatively uncommon, but is greatly enhanced

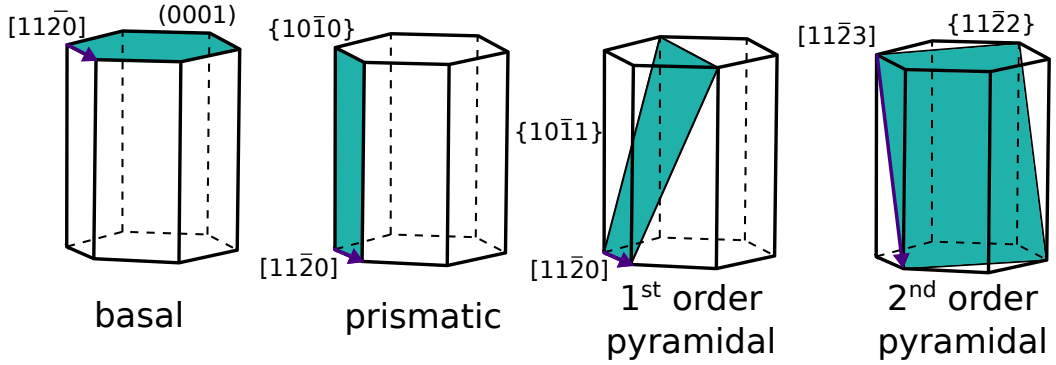

Figure 1.1: Deformation mechanisms typically reported in conventional Mg alloys.

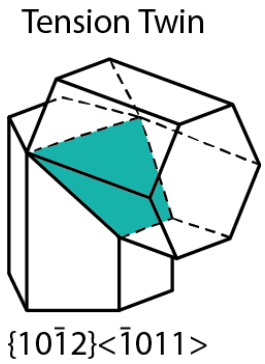

Figure 1.2: The commonly observed tension twinning deformation mode.

in rare earth containing alloys [5–7].

These deformation modes have widely varied CRSS values, particularly near room temperature. Basal slip is easy and effectively athermal at room temperature [8], with reported CRSS values as low as 1 MPa [9]. For non-basal slip, the reported CRSS values depend strongly on measurement technique. Many single crystal deformation experiments performed to examine other slip systems found

little to no evidence of prismatic or first-order pyramidal slip at room temperature prior to fracture [10, 11], while others report non-basal CRSS values two orders of magnitude greater than that of basal slip [12]. Other early single crystal studies reported basal:prismatic CRSS ratios approaching 1:100, even under constrained (plane strain compression) loading conditions in an orientation specifically designed to promote non-basal slip [13]. More recent polycrystal work has suggested basal:prismatic ratios in the range of 1:1.1 to 1:8. In these polycrystal studies, polycrystal plasticity models are parameterized to replicate the plastic anisotropy experimentally observed in strongly textured polycrystals. Various reported ratios from the literature are presented in Table 1.1.

The reported basal slip:tension twin CRSS ratios in the literature are similarly varied. Stanford and Barnett [17] report experimentally determined CRSS ratios for binary Mg-Zn alloys between 1:1.3-2.2. Raeisinia and Agnew [18] discuss ratios primarily in the range of 1:1.5-3 for binary Mg-Zn alloys with varied coarse grain sizes. Raeisinia *et al.* [24] review basal:tension twin CRSS ratios determined for AZ31 via polycrystal plasticity modeling techniques, with values ranging from 1:0.7-33 reported, but most values are near 1:1.8.

Because of the relatively small difference in the CRSS values between basal and prismatic slip, the crystallographic texture is important. As shown in the Schmid factor plots in Figure 1.3, grains which are favorably oriented for pris-

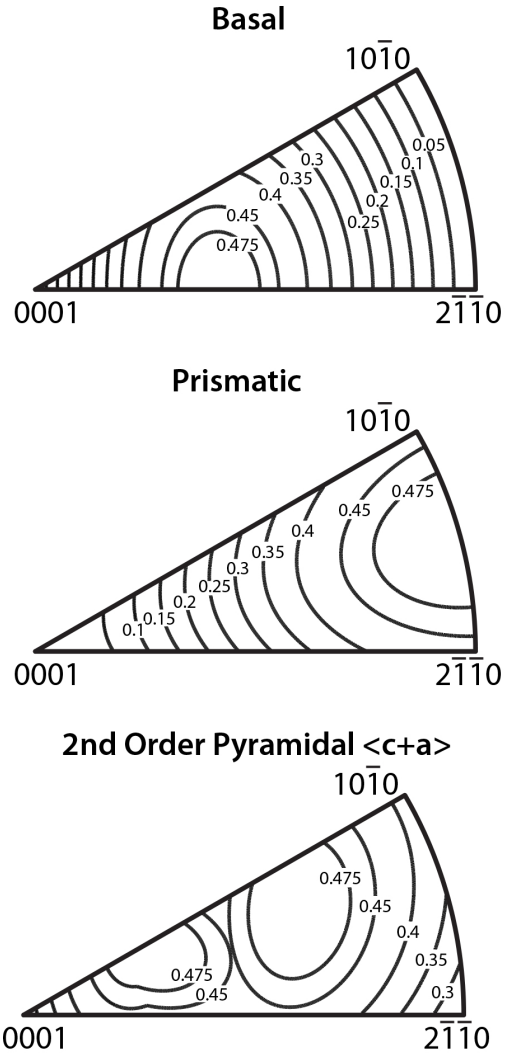

Figure 1.3: Schmid factor plots for the three primary slip systems active during magnesium alloy deformation.

matic slip are unfavorably oriented for basal slip and vice versa. Unfortunately, grains which are favorably oriented for pyramidal $\langle c+a \rangle$ slip are also favorably oriented for basal slip, which has a lower CRSS and will tend to dominate the deformation behavior.

Relative deformation mode activity in magnesium alloys materials is also dependent on grain size. Reduction in grain size below approximately 10μm has been reported to promote non-basal slip, an effect which has been attributed to grain boundary constraint [14]. Additionally, decreasing grain size has been reported to very strongly inhibit tensile twinning, completely suppressing twin formation below a critical threshold reported to be near 1μm [25–27]. The effect of grain size on twinning is typically much stronger than the effects on slip activity, particularly in the fine-grained regime [17, 28, 29].

The combination of dominant basal slip and tensile twinning typically leads to a strong basal texture after rolling or extrusion. During rolling, most magnesium alloys develop a basal texture (basal planes parallel to sheet sheet surfaces) with the (0001) pole figure peak split along the rolling direction. Slight elongation of the texture peaks toward the rolling direction (RD) is also common for pure magnesium and dilute conventional alloys [19, 30]. Spread of the basal pole figure toward the transverse direction (TD) is frequently observed with greater alloy content or the addition of rare earth elements [31]. Conventional

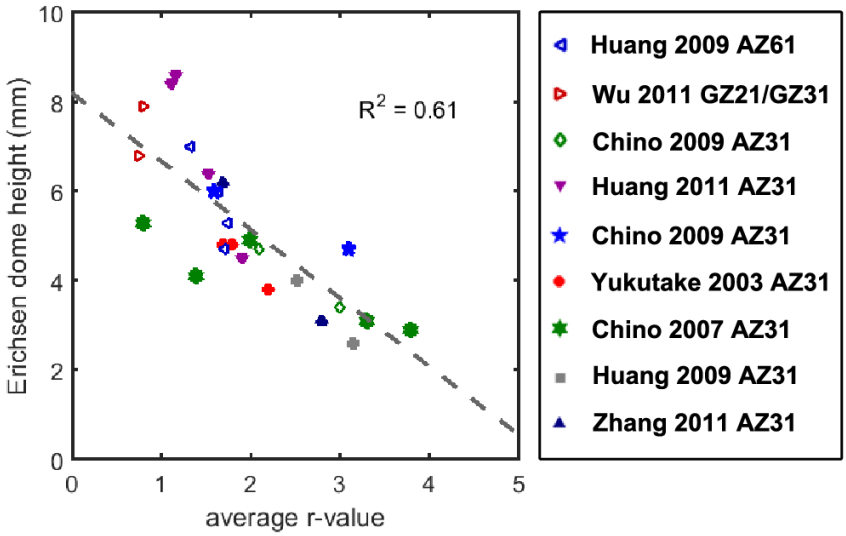

Figure 1.4: Correlation between Erichsen biaxial stretch test maximum dome height and the value of $\bar{r}$. Data obtained from the literature [33–41]. Plot adapted from Berman *et al.* [42].

extrusion textures are characterized by $\langle 10\bar{1}0 \rangle$ or $\langle 10\bar{1}0 \rangle$-$\langle 11\bar{2}0 \rangle$ fibers parallel to the extrusion direction, depending on extrusion conditions and alloy [32].

1.1.1 Formability in Mg alloys

Experimental investigation of formability in magnesium alloys has generally relied on the measurement of r-values, also known as Lankford coefficients. The r-values are defined as the ratio between the strains in the width and thickness directions after tensile straining to a pre-defined strain threshold [43]. This ratio

is calculated for three or more specimen orientations in the sheet plane, usually with the tensile axis angled by 0°, 45°, and 90° from the rolling direction. An average r-value, $\bar{r}$, can be calculated as:

$$\bar{r} = \frac{(r_0 + 2r_{45} + r_{90})}{4} \tag{1.1}$$

In steels and aluminum alloys, a high $\bar{r}$ value indicates that sheet material resists thinning during deformation, indicating good deep drawing behavior [44, 45]. Conversely, in hcp metals (including Mg) large values of $\bar{r}$ are associated with poor forming behavior [46]. This is likely because $\bar{r}$ is an indicator of sheet thinning, and forming failures in Mg alloys are usually fracture dominated, not thinning dominated. This also may indicate why $\bar{r}$ is a better predictor of forming performance than n, the power law hardening exponent. A survey of the available literature for magnesium alloys, adapted from Ref. [42] and shown in Figure 1.4, shows that $\bar{r}$ has a negative linear correlation with the maximum dome height achieved in a standard Erichsen biaxial stretch test, indicating that $\bar{r}$ is a valid indicator of room temperature formability. Values of $\bar{r}$ greater than 3.0 are common in commercial Mg alloys [8, 47], but the best forming behavior is observed in alloys that have $\bar{r}$ values near 1.0.

Formability is dictated by a complex array of factors, including grain size, second phase particle distribution, and alloy composition. In Mg al-

loys, improved forming behavior is typcially associated with decreasing grain size [14, 17, 42, 48, 49]. However, the dominant factor is typically crystallographic texture [50].

A strong basal texture is highly detrimental to formability because the grain orientations are unfavorable for the easiest deformation mode, basal slip. The correlation between basal peak intensity and the $\bar{r}$ values is shown in Figure 1.5, with stronger basal peaks correlated with high r-values and poor formability. Gehrmann *et al.* have reported that materials with a strong basal texture are more susceptible to strain localization and the formation of shear bands [51]. Another study on strongly textured polycrystals mechanically tested in various orientations revealed the striking plastic anisotropy that results from strong basal textures [47]. Numerous studies have also noted that increasing peak intensity of the basal pole figure is correlated with reduced formability [7, 42, 52, 53]. The planar anisotropy of the basal pole figure common in textured magnesium materials has also been noted, though its effects on forming behavior have not been fully explored [16, 54].

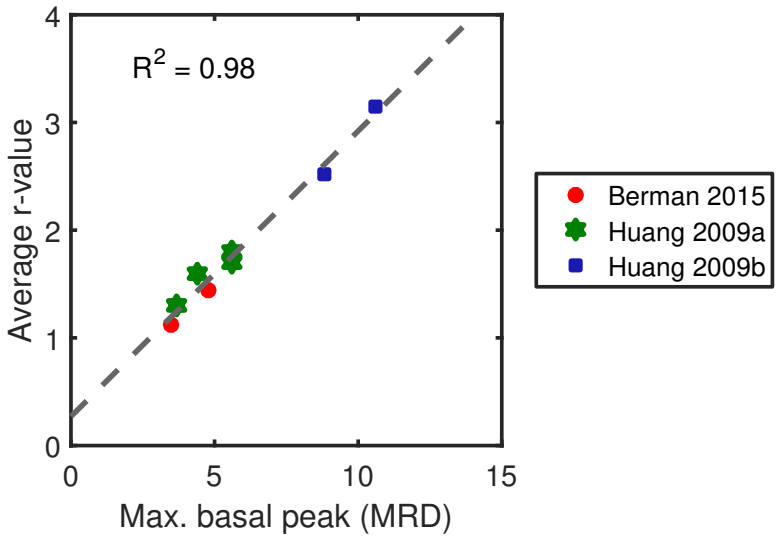

Figure 1.5: Correlation between peak intensity of the basal pole figure and $\bar{r}$values as reported in the literature [33, 38, 40, 42].

1.1.2 Deformation texture modification

Numerous exotic deformation pathways for magnesium alloys have been investigated including asymmetric rolling [55], multi-pass equal channel angular pressing (ECAP) [56, 57], upset forging [58], and high pressure torsion [59]. In general, these pathways have had some success in generating non-basal or weakened basal textures; however, these processing pathways have limited scalability and are unlikely to be viable for commercialization. Therefore they have little chance of seeing widespread practical implementation and will not be discussed further here.

Alloy additions which increase solid solution content and alter the intermetallic particle distribution can also affect the deformation texture. Increased solid solution content can alter the relative CRSS values via both simple size misfit and modification of the electronic structure [60]. Recently, numerous studies have investigated these effects via first principles calculations [61–64]. RE and alkaline earth additions in particular have been reported to promote non-basal slip and activate alternative twinning modes, thereby lowering the overall deformation texture strength. This translates to elongation of the basal pole figure peaks toward the TD instead of the RD during rolling (e.g.[7, 46, 65–69]). The weakening of the deformation texture caused by RE additions is not dramatic, and TD spreading has been observed in some RE-free alloys [31].

Greater alloy content above the solubility limit also leads to an increasing fraction of intermetallic particles, which can also alter texture evolution. Fine precipitates may also change texture evolution by altering the balance of deformation mode activity, because the geometry of different deformation modes and precipitates will determine the frequency of interaction and therefore the increment in hardening for each mode [70, 71]. For coarse particles, relatively little work has been conducted to explicitly consider the dependence of texture on particle distribution during deformation because alloys with large volume fractions of intermetallic particles have historically been considered unsuitable

for wrought applications. However, recent studies [42, 72] have shown this conventional wisdom to be incorrect, as the presence of coarse particles does not necessarily cause premature failure. In conventional magnesium (e.g. AZ series) alloys there is evidence that increasing the fraction of coarse ($>1\mu$m diameter) intermetallic particles may lead to deformation texture weakening [31].

1.2 Recrystallization in Mg alloys

In the literature on microstructural evolution during thermomechanical processing of magnesium alloys, both discontinuous and continuous recrystallization have been reported. Discontinuous recrystallization is a Gibbs type I transformation, characterized by distinct nucleation and growth phases. Conversely, continuous recrystallization is a Gibbs type II transformation which occurs homogeneously throughout the microstructure. Additionally, both static and dynamic recrystallization are commonly reported; however, the mechanisms present in each of these cases are generally not distinct, so their impacts on microstructural evolution are considered together.

In general, the recrystallization mechanisms most commonly reported in magnesium alloys preserve the basal texture, though some reduction in intensity is commonly observed [69, 73–77].

1.2.1 Reported recrystallization phenomena

- *Grain boundary bulging/necklace recrystallization/strain induced boundary migration (SIBM)/rotation recrystallization.* [66, 74, 75, 77–79] In this mechanism, discontinuous recrystallization occurs by preferential nucleation at grain boundaries, forming a "necklace" of recrystallized grains surrounding the deformed parent. Typically, nucleation occurs by the bulging of an existing grain boundary into the neighboring grain. This process is frequently reported to occur via SIBM. Deformation subsequent to bulge formation must maintain compatibility between the two adjacent grains, requiring that the bulge rotate relative to the parent, leading to the term "rotation recrystallization."

- *Twin recrystallization.* [6, 80–82] During dynamic recrystallization, twinned orientations are frequently reported to recrystallize prior to the parent orientations. There has been little discussion to date of the mechanism involved.

- *Shear band recrystallization.* [7, 69, 79, 83–85] Sites of shear localization, such as shear bands, contain an exceptionally high dislocation density and therefore a high local stored energy. Consequently, shear bands are preferred nucleation sites for recrystallization, and sometimes contain differ-

ent orientations than the matrix which may recrystallize to produce a new texture component.

- *Particle stimulated nucleation (PSN) of recrystallization.* [65, 86, 87] PSN is thought to happen at non-deformable second phase particles with diameters greater than approximately 1μm. These particles enhance local deformation due to compatibility constraints and dislocation buildup effects. The enhancement of dislocation density in the particle deformation zone causes a greater local driving force for recrystallization, leading to preferential nucleation.

- *Continuous recrystallization.* [76, 88] Continuous recrystallization via subgrain boundary coalescence has also been reported, though less commonly. In both magnesium and other alloy systems, this mechanism fails to substantially alter the deformation texture [89].

1.2.2 Recrystallization texture modification

One of the most promising strategies for modifying crystallographic texture during recrystallization is the addition of RE alloying elements. Upon recrystallization, RE additions result in the formation of a new texture component which, in rolled sheet, has the basal poles tilted 45° from the sheet normal

direction. The earliest reports of RE element texture modification attributed this effect to PSN during dynamic recrystallization [86]. However, it has recently been demonstrated that single phase solid solution RE-containing alloys also undergo the same evolution in texture, indicating that intermetallic particles are not required [52, 66, 90]. It has been suggested that the new texture component is the result of solute effects [5, 46, 52, 65, 68, 91]. Some authors suggest that RE texture results from preferential growth of recrystallized grains out of the RE-influenced shear bands, which are reported to be more frequent and more diffuse than shear bands in conventional alloys [5, 69, 84, 92]. Also, segregation of RE solute to grain boundaries may inhibit their mobility, slowing grain boundary bulge formation and decreasing the propensity for necklace recrystallization.

In addition to solute effects, the presence of coarse intermetallic particles may also alter the recrystallization behavior. Basu *et al.* [69] observed less texture modification in a particle-containing Mg-Ce alloy compared to a single phase Mg-Gd alloy and suggested it may simply be due to particle pinning restricting the growth of the new texture component; however, no information regarding the particle distribution was reported. Hadorn *et al.* studied the effect of submicron particles on texture evolution in Mg-Nd alloys and found that Zener pinning aided in the development and retention of a RE texture, but that the

presence of the pinning particles was not as critical as solute content [31, 93]. However, many RE elements have very low solubility in magnesium and tend to form intermetallic particles, even at low levels of alloy content. Many studies have failed to discuss the possibility that the intermetallic particles may play an important role in determining the texture and microstructural evolution.

Characterization the particle distribution is a critical aspect of investigating microstructural evolution. Intermetallic particles of different sizes modify texture in dramatically different ways and will have differing degrees of influence on boundary mobility and the nucleation or growth of recrystallized grains via particle stimulated nucleation and Zener drag [89, 94]. Coarse particles in magnesium alloys have been reported to promote PSN, which alters recrystallization kinetics and weakens recrystallization texture [87, 95, 96]. A homogeneous distribution of intermetallic particles has also been reported to inhibit boundary mobility, delaying necklace recrystallization [96]. In magnesium and other alloy systems, fine particle distributions can either strengthen [97] or weaken [81, 98] recrystallization texture development.

1.3 Grain growth in Mg alloys

After the impingement of recrystallized grains, the average grain diameter will continue to increase, driven by a reduction in total grain boundary area. In magnesium alloys, grain growth is typically accompanied by in increase in the intensity of the basal texture [69, 73]. Previously, this was attributed to a mobility dominance caused by the presence of a maximum growth rate orientation (MGRO) [74, 75, 77]. The MGRO is the orientation relationship between the deformed matrix and a recrystallized grain at which a boundary has the maximum mobility. The reasons for the existence of an MGRO are still poorly understood, but it has been attributed in other alloy systems to boundary free volume or a coincident site lattice relationship [89]. For magnesium, the reported orientation relationship is a 30° rotation about the c-axis, which does not alter the orientation of the c-axis and leads to retained basal texture [46]. It should be noted that this misorientation also corresponds to the highest angle boundary possible between two grains with parallel c-axes.

1.4 Research Objectives

With these solute and intermetallic particle effects on deformation and recrystallization in mind, the following research objectives are proposed:

1. Isolate the texture weakening mechanisms that can be attributed to intermetallic particles in comparison to weakening that occurs due to dislocation-solute interactions.

2. Identify promising strategies for formability improvement via texture modification in scalable, commercially relevant alloy and processing systems.

3. Provide tools to accelerate the development of alloy and process development for wrought magnesium by developing strategies to predict forming behavior based on texture and microstructure.

Table 1.1: Room temperature CRSS ratios reported in the literature

Alloy	CRSS Normalized to Basal			Single or Polycrystal	Ref.
	Prism.	Pyr.	Twin		
AZ31	1.1			polycrystal	[14]
AZ61	1.5-2			polycrystal	[15]
AZ31B	2-2.5	2.4-3		polycrystal	[8]
AZ31B	2.4	2.9	0.3	polycrystal	[16]
AZ61L	2.6	3.7	1.1,1.8,3.2	polycrystal	Ch. 6
Mg-0-3wt%Zn	2.5-8		1.3-2.2	polycrystal	[17]
Mg-0-2.3wt%Zn			1.5-3	polycrystal	[18]
AZ31B		3	0.5	polycrystal	[16, 19]
Mg-1.1wt%Zn	30			single crystal	[20, 21]
Mg-0.5wt%Zn	41			single crystal	[20, 21]
pure Mg	50			single crystal	[22]
Mg-0.2wt%Zn	53			single crystal	[20, 21]
pure Mg	90			single crystal	[20, 21]
pure Mg	48-96			single crystal	[13]
pure Mg		73		single crystal	[23]

Chapter 2

Experimental and Simulation Procedures

Two sets of alloys are examined in this work, namely a model binary Mg-Zn alloy system and the commercial alloy AXJ810. The preparation, testing, and characterization of these alloys is described in Sections 2.1 to 2.3. The polycrystal plasticity methods used for analysis of active deformation mechanisms and the prediction of formability are described in Section 2.4.

2.1 Mg-Zn alloy preparation and processing

Three binary Mg-Zn alloys were thermomechanically processed in order to study the effect of alloying and heat treatment temperature on deformation and recrystallization behavior. All three alloys were first subjected to preliminary processing steps, described in Section 2.1.1, in order to develop a microstructure suitable for study of deformation processing and recrystallization, as described in Section 2.1.2.

2.1.1 Preliminary thermomechanical processing

Three binary magnesium zinc alloys with nominal Zn concentrations of 4.5wt%, 6wt%, and 9wt% were received in the as-cast state from Professor Jian-Feng Nie of Monash University. The alloys were heated to 719°Cfor melting and poured into a 30mm by 50mm rectangular steel mold preheated to 200°C. As shown in the phase diagram (Figure 2.1), all of these alloys fall in the two phase α-Mg and MgZn intermetallic region, indicating that they will contain both a magnesium solid solution as well as a population of intermetallic particles at all temperatures below approximately 250°C.

These three alloys were first thermomechanically processed via a four step pathway to develop a microstructure suitable for further study. The as-cast ma-

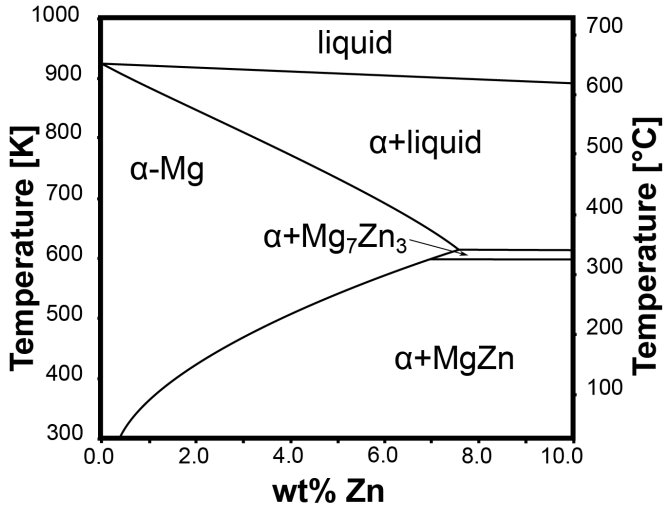

Figure 2.1: Mg-rich section of the binary Mg-Zn phase diagram predicted by Pandat with the PanMagnesium database [1].

terial was first solution treated at 300°C for 2h in air, then cooled at 1.25°C/min to 250°C. The alloys were then isothermally heat treated at 250°C for 16 hours, then quenched in water. The heat-treated material was then extruded at an extrusion ratio of 32:1 into strip with a rectangular cross section 3mm by 10mm at a temperature of 250°C and an extrusion speed of 0.1mm/s. The extruded strip was wrapped in a protective layer of Al foil and heat treated in a 250°C nitrate salt bath for 5 minutes.

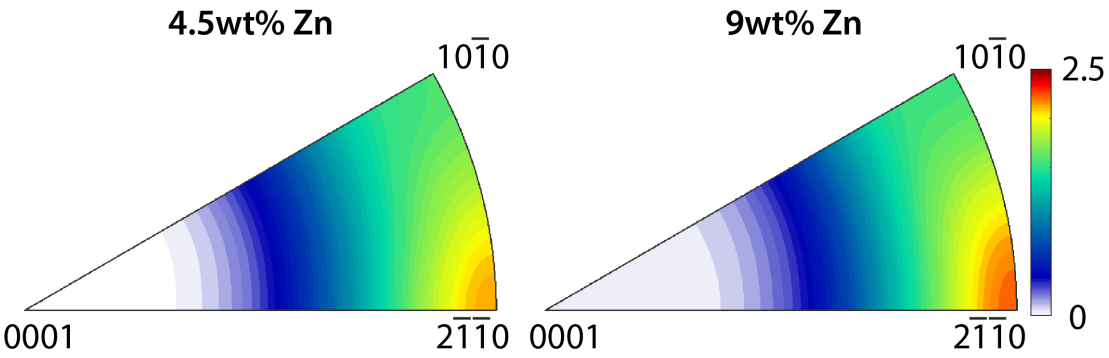

Figure 2.2: IPFs for the α-Mg phase for the 4.5wt% and 9wt% Zn alloys in the extruded and recrystallized microstructural condition, referenced to the extrusion direction.

At the conclusion of this thermomechanical processing procedure, a fine-grained microstructure with a homogeneous distribution of small (approximately 100nm diameter) pinning precipitates alongside a population of coarse intermetallic particles with a volume fraction that varies between alloys is developed. The extruded and recrystallized textures are shown as IPFs in Figure 2.2. These are considered the starting microstructures for the deformation and recrystallization studies described in Chapters 3 and 4.

2.1.2 Mg-Zn deformation and recrystallization processing

Deformation and recrystallization behavior was studied for each of the three alloys after the preliminary thermomechanical processing described in Section 2.1.1. First, sections of the extrudate were preheated in air for 5 minutes at

150°C using a box furnace. These specimens warm rolled to a 40% reduction in thickness in a single pass with a roll temperature of 150°C and an approximate roll speed of 10mm/s. In all cases, the rolling direction is parallel to the prior extrusion direction. The samples were quenched in water at the conclusion of deformation. Additional samples of each alloy were rolled at ambient temperature with no preheat using the same roll speed to a 7% reduction in thickness.

Further heat treatments are conducted to study the static recrystallization behavior post-deformation. Specimens were heat treated at temperatures of 100°C, 150°C, and 200°C in silicone oil baths for varied times, as reported in Section 4.2. Additional specimens were wrapped in a layer of protective Al foil and heat treated at temperatures of 250°C and 300°C for varied times. All specimens were water-quenched upon removal from the heat treatment baths.

Microhardness measurements were acquired to track the progress of recrystallization using a Wolpert Group Micro-Vickers Hardness tester at a 200g load using a 10s dwell time. Ten data points were collected and averaged for each microstructural condition. Fraction recrystallized, f_{RX}, was calculated from microhardness measurements via the relationship:

$$f_{RX} = \frac{H_{max} - H}{H_{max} - H_{min}}$$

where H_{max} is the as-deformed (maximum) hardness, H_{min} is the fully recrys-

tallized (minimum) hardness, and H is the measured partially recrystallized hardness.

2.2 AXJ810 alloy preparation and processing

The simultaneous complementary effects of solute and coarse intermetallic particles were examined in thixomolded AXJ810, with the nominal composition shown in Table 2.1. The additions of Ca and Sr have been shown to be an effective means to improve creep resistance at a lower cost than rare earth additions [99–101]. Thixomolding is semi-solid molding operation that results in a fine-grained starting microstructure. However, due to the semi-solid nature of the processing technique, a small volume fraction (under 10%) of 50-100μmexternally solidified grains result. As-thixomolded bars and thixomolded and thermomechanically processed (TTMP) sheet were received from nanoMAG, LLC. The TTMP sheet was used to study the static recrystallization kinetics from a partially-recrystallized state, as described in Section 2.2.1. The as-molded material was heat treated to develop different intermetallic particle distributions, and was subsequently subjected to warm compression to investigate the effect of particle distribution on dynamic recrystallization behavior, described in Section 2.2.2.

Table 2.1: Nominal composition in weight percent of the commercial AXJ810 magnesium alloy

	Al	Ca	Sr	Mn	Mg
AXJ810	8.0wt%	1.02wt%	0.31wt%	0.2wt%	bal.

The AXJ810 alloy contains nominally three phases, the α-Mg phase, the β-$Mg_{17}Al_{12}$ phase, and a $(Mg,Al)_2Ca$ Laves phase with either the C36 or C15 crystal structure depending on temperature [102, 103]. The solidification pathway predicted by the Scheil model as implemented in Pandat [1] is shown in Figure 2.3. As shown in the equilibrium phase fraction diagram (Figure 2.4), the Laves phase is thermally stable until the onset of melting, while the β phase has a solvus of 356°C, allowing the spatial distribution of this phase to be modified via heat treatment as described in the following section.

2.2.1 Static recrystallization of TTMP AXJ810

TTMP sheet material was produced by nanoMAG, LLC from thixomolded plate with a 3mm thickness. These 3mm plates were warm rolled in one pass at an approximate temperature of 250°C to a 50% reduction in thickness. The sheets were then subjected to a flattening treatment at 270°C for 2 minutes.

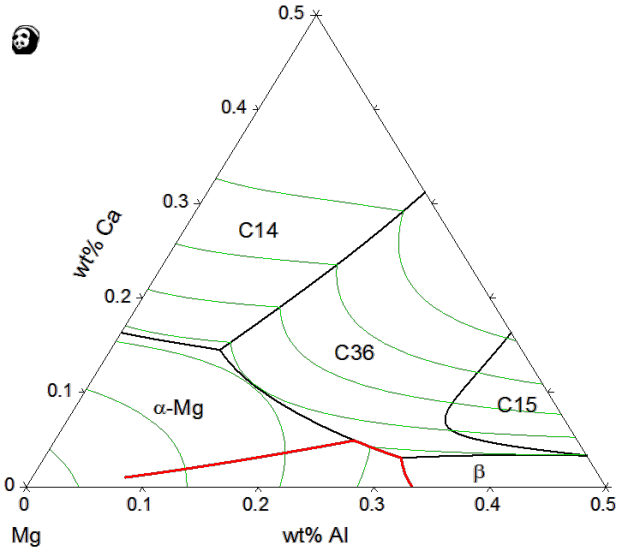

Figure 2.3: The solidification pathway and liquidus surface of the AXJ810 magnesium alloy, as calculated via the Scheil model using the Pandat PanMagnesium database [1].

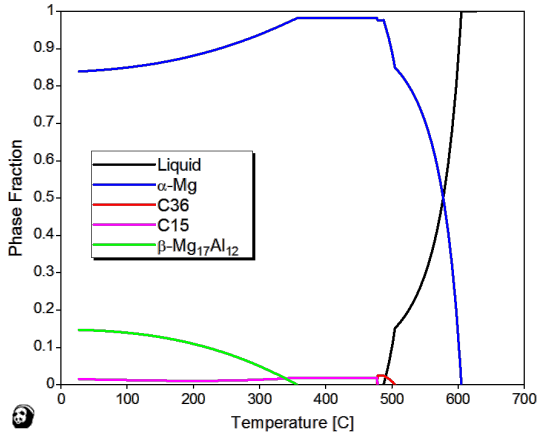

Figure 2.4: Phase fractions as a function of temperature in AXJ810, as calculated using Pandat [1].

The material state after this flattening treatment is considered the as-TTMP microstructure.

Static recrystallization heat treatments were conducted on the as-TTMP material in a tube furnace in air at temperatures above and below the solvus of the β phase intermetallic particles, at 300°C and 450°C, respectively, to study the microstructural and texture evolution during static recrystallization.

2.2.2 Thixomolded compression specimens

Uniaxial compression specimens with dimensions 5mm by 5mm by 10mm were cut from the as-thixomolded bars received from nanoMAG, LLC via electrical discharge machining. Shallow cross-shaped lubrication channels were also machined into the square faces of the compression specimens to minimize barreling during deformation. Two microstructural conditions in addition to the as-molded state were prepared via heat treatment in air using a box furnace. These heat treatments and the predicted resulting composition of the solid solution α phase are summarized in Table 2.2. The as-molded composition is the result of the Scheil solidification model prediction and is an average for all of the α phase, while the predicted compositions for the other heat treated conditions are the equilibrium at the heat treatment temperature.

Table 2.2: Heat treatment schedules for each microstructural starting condition and Pandat-predicted composition (atomic percent) of the α phase [1].

Designation	Heat Treatment	Al	Ca	Mg
As-molded (AM)	—	11.6%	$7{\cdot}10^{-6}$%	88.4%
Equilibrated	16h 200°C	2.4%	$3{\cdot}10^{-6}$%	97.6%
Solutioned	2h 375°C	6.2%	$6{\cdot}10^{-4}$%	93.8%

Elevated temperature uniaxial compression tests were conducted on the machined and heat treated specimens using an Instron 5582 system fitted with SiC dies. Both the compression dies and the specimen faces were lubricated with molybdenum disulfide solid state lubricant to reduce barreling during deformation. Induction heating was utilized to heat specimens to 250°C, and the temperature was held constant for 5 minutes prior to the start of compression. Compression testing was conducted at a constant crosshead speed with an initial strain rate of 0.5/s to final true plastic strains of 0.1, 0.3, or 0.7, controlled to $\pm 100\mu$m of the calculated target height. At the conclusion of deformation specimens were quenched in water. A compressed specimen in the testing fixture is shown in Figure 2.5, with the induction coil moved aside for visibility.

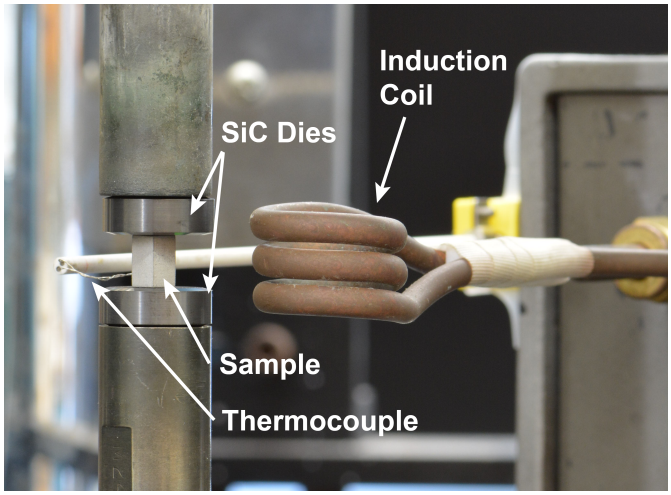

Figure 2.5: Compressed specimen in uniaxial testing fixture. The induction coil is moved aside for visibility. Reproduced with permission from Reference [96].

2.3 Microstructural characterization

Microstructural characterization of both the Mg-Zn binary alloys and AXJ810 alloys was conducted via scanning electron microscopy (SEM) and electron backscatter diffraction (EBSD). All specimens were prepared for microstructural examination via conventional metallographic techniques. First, sections were cut from the bulk specimens using a low-speed diamond saw. These sections were ground on SiC paper, with a final abrasive size of 1200 grit. Then, specimens were polished on diamond lapping films using methanol as a lubricant to a final abrasive size of 1μm. AXJ810 specimens for imaging were then etched with a 1:10 solution of o-phosphoric acid in methanol. All Mg-Zn and

AXJ810 specimens for EBSD characterization were then argon ion milled using the Gatan Precision Ion Polishing System.

Scanning electron microscopy was conducted on several different microscopes. The etched AXJ810 specimens were imaged in secondary electron mode using an FEI DB-235 microscope. Mg-Zn specimens were imaged using an FEI XL30 SEM equipped with a backscattered electron (BSE) detector.

2.3.1 Mg-Zn alloy intermetallic particle characterization

The intermetallic particle volume fraction in the Mg-Zn binary alloys was measured as a function of processing using the MATLAB® image processing toolbox [104]. Eight or more BSE images at sufficient resolution to capture the fine intermetallic particles were captured using the FEI XL30 SEM. They were then analyzed using a simple thresholding algorithm to measure the volume fraction. The threshold value was calculated using Otsu's method via a built-in MATLAB function "graythresh" [105]. This method segments an image using the assumption of a background and a foreground, with the threshold selected to minimize the variance in pixel intensity in both background and foreground.

This methodology was used to characterize the particle volume fraction in the 4.5wt% and 9wt% alloys in the extruded and recrystallized, as-rolled, fully

recrystallized at 100°C, and fully recrystallized at 250°C microstructural conditions. The particles were also classified based on their equivalent circular diameter to compare the volume fractions of fine (<250nm diameter) and coarse intermetallic particles. The results for each microstructural condition are discussed as relevant in Chapters 3 and 4.

These measured volume fraction values should be considered a lower bound, as they will not capture particles smaller than approximately 4 pixels in the image, or approximately 160nm^2. These values can be compared to the equilibrium volume fractions as calculated by Pandat [1] at several processing temperatures, as presented in Table 2.3. In many cases, the Pandat-predicted volume fractions are substantially lower then the measured volume fractions. This may be a result of errors in the thermodynamic database, inconsistencies in measurement of volume fraction, or incorrect alloy compositions. The nominal compositions will still be used as labels throughout the document, but when the effects of intermetallic particles are discussed the measured volume fractions will be explicitly used.

Table 2.3: Equilibrium intermetallic particle volume fractions at selected processing temperatures, as calculated by Pandat [1]

	4.5wt%Zn	**9wt%Zn**
20°C	3.1%	6.6%
100°C	2.5%	6.1%
150°C	1.9%	5.5%
200°C	1.0%	4.5%
250°C	–	3.6%
300°C	–	2.3%

2.3.2 Electron backscatter diffraction techniques

All EBSD characterization was conducted on either an FEI Quanta or an FEI XL30 SEM equipped with a EDAX Hikari high-speed EBSD camera. All EBSD scans were conducted at 20kV with a spot size of 5. Small high resolution maps for visualization were collected with 2 by 2 binning at a fine step size, typically 150nm, on a hexagonal grid with simultaneous electron dispersive x-ray spectroscopy to allow for reliable identification of intermetallic particle location. These small maps were cleaned up using neighborhood orientation correlation in the TSL OIM analysis software.

Larger EBSD maps for quantitative analysis containing at least 10,000 grains were collected at a fixed step size of 300nm on a hexagonal grid using 4 by 4 camera binning. In these large maps, groups of less than five sampling points and sampling points with low band contrast (image quality) were discarded. No other cleanup routines were employed to prevent the introduction of cleanup artifacts into the quantitative microstructural analysis of the deformed and recrystallized microstructures and their textures.

Several types of maps are utilized for presentation of the EBSD data. The majority of maps presented in this work are IPF maps, which color grains based on the orientation of a particular crystallographic axis relative a direction in the sample reference frame and provide information about crystallographic orientation. Additionally, some IQ maps are presented, where the gray value of each point represents the amount of contrast between the bands and the background in the Kikuchi pattern. Brighter pixels indicate good band contrast, suggesting a relatively defect free material element, while darker contrast pixels are not diffracting as uniformly. In addition to the standard mapping techniques, the EBSD data sets collected in this work were analyzed using three different methods: grain orientation spread (GOS), grain reference orientation deviation (GROD), and intragranular misorientation analysis (IGMA). These microstructural metrics are described in the following sections, and were analyzed using

either the TSL OIM Analysis software package (versions 6.0 to 7.2) or the MTEX texture analysis toolbox v4.2.1 for Matlab [106] as noted.

Grain orientation spread

Grain orientation spread for a particular grain is defined as the mean disorientation in degrees of each EBSD sampling point grain from the grain average orientation, or:

$$GOS = \frac{1}{N}\sum_{A=1}^{N} min\left(cos^{-1}\left(\frac{trace\left(g_{ave}\left(h\ g^{A}\right)^{-1}\right)-1}{2}\right)\right), \tag{2.1}$$

where N is the number of points in the grain, A is the index of the point within the grain, g_{ave} is the matrix representation of grain average orientation, h is an element of the symmetry group for the given crystal structure, and g^A is the orientation of point of interest [107]. Grains with large GOS values have a large amount of internal misorientation, indicating a high geometrically necessary dislocation (GND) content and therefore a relatively large amount of stored energy. Conversely, recrystallized grains will have minimal internal misorientation and therefore low GOS values [107]. A GOS threshold can be used to determine fraction recrystallized, and a threshold value of 1° is used throughout this work. This threshold was selected by examining the histogram of GOS values for a

sample partially recrystallized during static annealing. The histogram showed a clear bimodal distribution of GOS values, with one peak below 1° representing recrystallized grains and a second peak above 1° corresponding to the deformed matrix grains. Additionally, the microstructure as a whole can be described by the area/volume fraction of grains that have particular values of grain orientation spread.

Grain reference orientation deviation

Grain reference orientation deviation mapping gives spatial context to the grain orientation spread data by assigning a color value to each EBSD sampling point within a grain based on the disorientation of that sampling point from the grain average orientation. Steep gradients in color correspond to steep misorientation gradients and high local geometrically necessary dislocation densities. GROD maps are particularly useful in multi-modal EBSD/energy dispersive spectroscopy (EDS) datasets, where the presence of sharp misorientation gradients and recrystallized grains can be compared to the location of intermetallic particles.

Intragranular misorientation analysis

While GROD and GOS capture the magnitude of the misorientation *angles* within grains, IGMA captures the misorientation *axes*. This technique was pioneered by Chun *et al.* [108] and first applied to magnesium alloys by Hadorn *et al.* [66]. The internal misorientation axes provides information about the populations of GND belonging to different slip systems. Dislocations of a particular slip system produce lattice curvature around a particular axis, called the Taylor axis. For instance, an array of prismatic dislocations will cause lattice curvature around the c axis in an hcp material. While EBSD cannot capture statistically stored dislocations because they do not result in lattice curvature, it is assumed that the GND present in the deformed microstructure participated in deformation and can offer at least qualitative insight into relative slip system activity. For this analysis, only disorientations between 2° and 4° were considered.

2.3.3 Transmission electron microscopy

Specimens for investigation by transmission electron microscopy (TEM) were prepared by either argon ion milling or site-specific liftout using a focused ion beam (FIB) microscope. Specimens for ion milling were ground on SiC paper to a thickness of 200μm, with a final grinding step of 1200 grit paper.

Disks 3mm in diameter were then punched from the initial specimen. These disks were manually polished on diamond lapping films to a final thickness of 60μm using methanol as a lubricant and with 1μm as a final abrasive size. For specimens cut from sheet less than 3mm thick with the rolling or transverse direction parallel to the foil normal, the flat ground specimen was mounted to a copper support ring with 3mm outer diameter and 2mm inner diameter using a cyanoacrylate adhesive. These disks were then argon ion milled using the Gatan Precision Ion Polishing System in two steps. First, the disks were milled at liquid nitrogen temperatures using 5kV accelerating voltage at gun tilts of $\pm 5^{\circ}$ until perforation. The perforated disks were then milled at 2.5kV and $\pm 2^{\circ}$ gun tilt for 30 min for final cleaning.

Site-specific foils were extracted using a FIB liftout technique in an FEI Helios Dualbeam Nanolab 650 microscope equipped with an OmniProbe system. First, regions of interest were selected using EBSD. Then, a 0.5μm thick layer of electron-deposited platinum was placed, followed by 1μm of ion-deposited platinum. The foil was extracted from the bulk specimen at a thickness of 800nm and attached to a Cu support grid using Pt deposition. It was then thinned to a final thickness of approximately 300nm. Initial thinning was conducted with a 16kV 45pA gallium ion beam, stepping down to final milling parameters of 2kV and 10pA.

2.4 VPSC simulation procedure

In order to rapidly assess deformation mode activity and potential formability of the microstructures and textures developed during processing, a polycrystal plasticity model was employed. Simulation of the plastic response was conducted using the viscoplastic self-consistent approach [109, 110]. In this framework, each grain is considered a plastic Eshelby-type inclusion in a homogeneous effective medium having the properties of the aggregate polycrystal. A macroscopic velocity gradient is imposed and shear rates are calculated for each grain on the relevant slip or twinning systems. These shear rates are used to calculate crystallographic texture evolution, grain-scale hardening, slip activity, macroscopic stress-strain behavior, and r-values. All simulated mechanical tests are conducted at a strain rate of 10^{-3}/s unless otherwise noted.

Hardening on each slip or twinning system is captured using an extended Voce law, where the critical resolved shear stress on system s after strain Γ is given by:

$$\tau^s = \tau_0^s + (\tau_1^s + \theta_1^s \Gamma)\left(1 - exp\left(-\frac{\theta_0^s \Gamma}{\tau_1^s}\right)\right) \tag{2.2}$$

[111] in which the τ_i^s and θ_i^s values are phenomenological hardening parameters for the s^{th} slip or twinning system. The τ_0 parameter is an effective initial critical resolved shear stress. These hardening parameters are selected based such

that the simulated mechanical behavior is in agreement with experiment; the hardening parameters used for particular simulations are reported in the appropriate sections. Twinning is captured using the Predominant Twin Reorientation scheme proposed by Tomé *et al.* [112]. This twinning scheme is a Schmid-type law that accounts for the directionality of twinning and also accounts for the effect of twin activity on texture. Reorientation occurs when twinning contributes 10% of the strain in a given grain, but the results presented were determined to be relatively insensitive to this threshold. The τ_i^s and θ_i^s hardening parameters are selected based on simulated alloy, as noted in each chapter.

2.4.1 VPSC simulation of formability

This VPSC framework is used to simulate r-value tests, described in Chapter 6. Uniaxial tensile tests to 10% plastic strain are simulated for angles between 0° and 90° in increments of 15°, and both r-values and $\bar{r}$ values are calculated as described in Section 1.1.1. This method of calculating r-values is compared to experimental results in Figure 2.6 for TTMP AZ61L [42]; the experimental values are accurately reproduced [113, 114]. Additionally shown are r-values calculated from the ratio of instantaneous strain rates instead of accumulated strains, as utilized by the standard VPSC code [109]. The instantaneous (strain

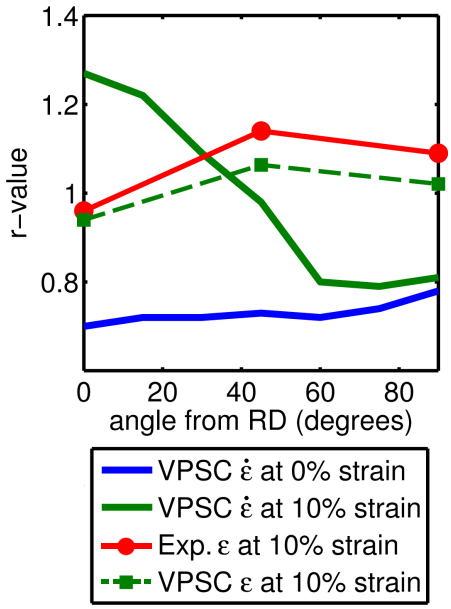

Figure 2.6: Various methods of calculating r-values in a simulated tensile test compared to experimental data. The VPSC model is parameterized to TTMP AZ61L, and the experimental r-values are from the same material [42, 113]. Figure reprinted with permission from Reference [113].

rate based) r-values do not accurately reproduce the experimental observations and therefore are not used.

Chapter 3

Control of texture during deformation

Due to the tendency of common recrystallization mechanisms in magnesium alloys to preserve the deformation texture (Section 1.2), minimizing the texture strength developed during mechanical processing is a critical consideration. As discussed in Section 1.1, alloying may alter the balance of deformation mechanisms via both solid solution effects as well as particle effects, thereby altering the deformation texture evolution. The effects of particle versus those of solute have proven difficult to decouple due to the low solubility of many alloying elements studied to date, including most RE additions. In this section, texture

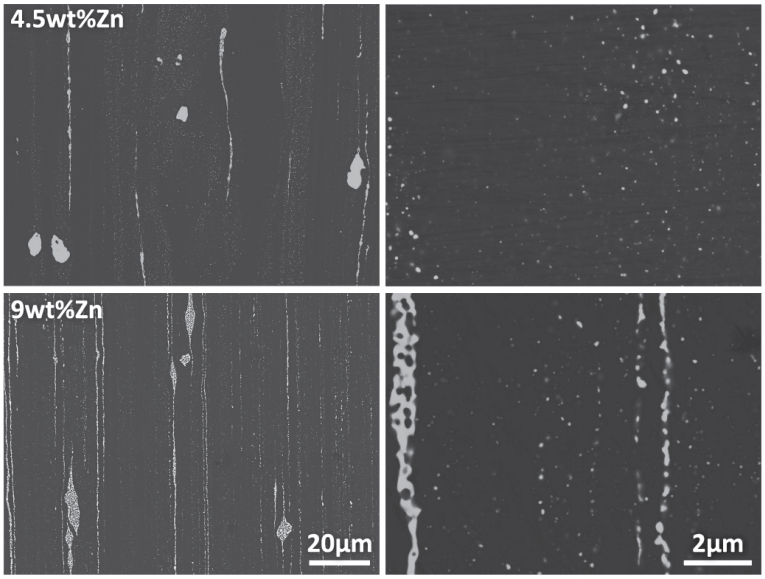

Figure 3.1: Particle distributions in the pre-deformation microstructures for the nominally 4.5wt% (top) and 9wt% Zn (bottom) alloys.

evolution in two-phase binary Mg-Zn alloys with varied Zn content is examined in order to isolate the effect of intermetallic particles on deformation behavior. The VPSC polycrystal plasticity model is utilized to examine potential sources of differences in deformation mechanisms on texture evolution.

3.1 Experimental microstructural evolution during rolling

The deformation behavior during warm rolling of the 4.5wt% and 9wt% Zn alloys is compared. The initial microstructural condition resulted from the preliminary thermomechanical processing procedures described in Section 2.1.1. The particle distributions present in the initial microstructures are shown in BSE micrographs Figure 3.1. In the initial state, the particle distribution is strongly bimodal, with populations of fine (less than 100nm diameter) near-spherical particles throughout the microstructure and long stringers of coarse intermetallic particles aligned with the prior extrusion direction present at grain boundaries.

The volume fractions of coarse and fine particles, measured as described in 2.3, are presented in Table 3.1 for each alloy. The median fine particle diameters in the 4.5wt% Zn alloy are 84nm and 96nm, respectively. While the fine particles distributions differ slightly, the predicted increment in resolved shear stress via the Orowan bowing mechanism is nearly equal for any selected slip system, differing by a maximum of 2MPa. More complex treatments based on precipitate geometry (e.g. [70, 71]) are not necessary due to the spherical shape of the precipitates. As such, the fine particle distributions are not predicted to

Table 3.1: Measured volume fraction Mg-Zn intermetallic particles in several processed conditions. Fine particles are defined as having an equivalent circular diameter less than 500nm.

	4.5wt%Zn			**9wt%Zn**		
	fine	coarse	total	fine	coarse	total
extruded & recrystallized	0.67%	0.50%	1.17%	2.46%	4.98%	7.44%
as-rolled	0.80%	0.47%	1.27%	2.18%	4.90%	7.08%

cause substantially different hardening behavior during deformation of the various alloys. Additionally, the 4.5wt% Zn and 9wt% Zn alloys have similar starting grain sizes of 5.7μm and 6.2μm, respectively, further suggesting that Hall-Petch related differences in deformation behavior are unlikely. Nevertheless, the possibility of differences in hardening behavior is still examined in Section 3.2.1.

The initial microstructures were produced by warm rolling at 150°C to a 40% reduction in thickness in a single pass. The texture evolution is compared in Figure 3.2. As shown, both alloys initially have a weak asymmetrical basal texture with strong TD spread resulting from the prior extrusion processing. In both cases, rolling results in strengthening of the basal texture and the development of a split basal peak. Both alloys also undergo a depletion of TD-tilted ori-

entations. In the as-rolled state, the 4.5wt% Zn alloy has greater basal intensity and less TD spread in the basal pole figure than the 9wt% Zn alloy, suggesting poorer forming behavior.

Representative EBSD maps of the as-rolled state are shown in Figure 3.3. In the as-rolled state, the grains are elongated, have very low IQ, and contain large internal orientation gradients. These characteristics demonstrate that dynamic recrystallization has not occurred, thus the observed texture evolution is attributed to deformation, not recrystallization. The underlying mechanisms that may cause the observed differences in rolling texture are examined in the following section.

3.2 VPSC simulation of texture evolution

Several possible mechanisms which may have resulted in the development of different rolling textures for each alloy are examined. Differences in hardening behavior of the slip systems, differences in starting texture, and particle stabilization of TD-tilt orientations are examined.

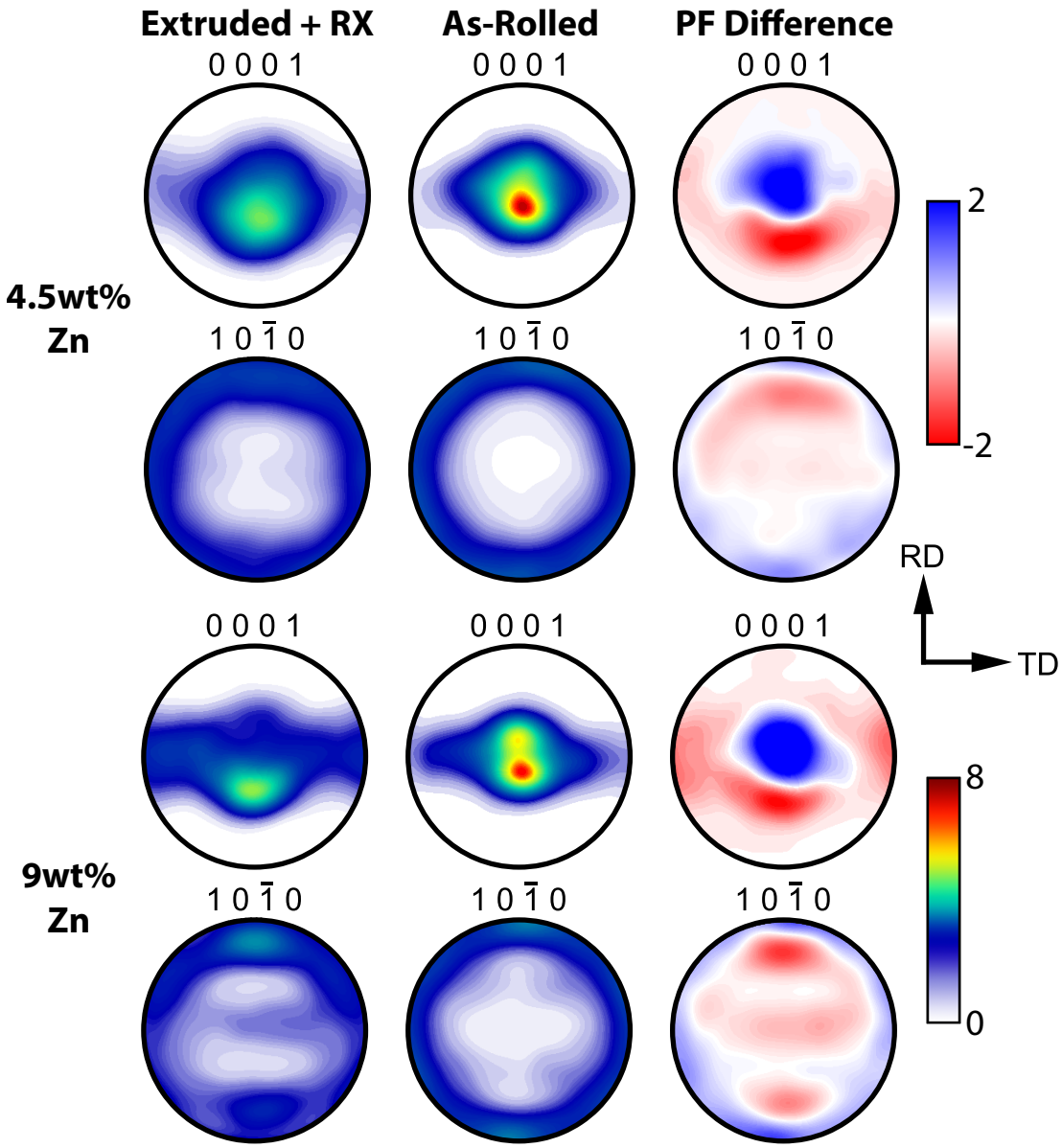

Figure 3.2: Basal and prismatic PFs and PF difference plots showing the experimentally observed texture evolution during rolling for the 4.5wt% and 9wt% alloys.

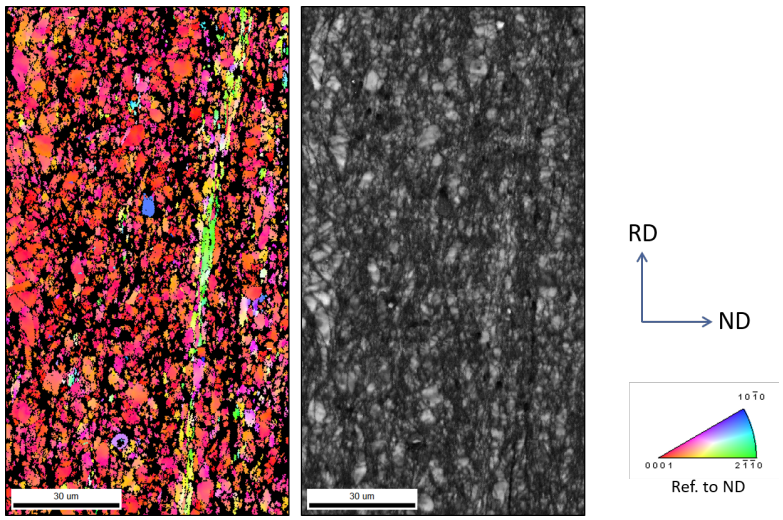

Figure 3.3: IPF and IQ map of the as-rolled structure for the Mg-9wt%Zn alloy. No dynamic recrystallization was observed during warm rolling.

3.2.1 Hardening behavior during deformation

The VPSC polycrystal plasticity model was parameterized using mechanical data from the nominally 4.5wt% Zn and 9wt% Zn alloys in the pre-deformation microstructural condition. Uniaxial compression texts were conducted on specimens with the loading direction parallel to the RD and TD, allowing selection of hardening parameters to capture the experimentally observed plastic anisotropy.

The selected Voce hardening parameters for the α-Mg phase are presented in Table 3.2. For the two alloys, the values of τ_1, θ_0, θ_1, A^{th1}, and A^{th2} are identical. The ratios of τ_0 for each slip system are constant, but the magnitudes increased by 50% for the 9wt% alloy. The resulting curves are shown in Figure

3.4. As shown, in both cases the simulated anisotropy between the RD and TD is smaller than in the experimentally observed case; however the sigmoidal shape of the stress-strain curve and the increased hardening rate along the TD is reproduced. This slight mismatch may result from the high aspect ratio of the coarse intermetallic particles, which is not addressed in this VPSC simulation.

Initial attempts at parameterization utilized a two-phase model, representing the deformable α-Mg phase and the non-deforming intermetallic particle phase, with the volume fractions selected based on the experimental characterization of the coarse particle fraction. The Voce hardening parameters determined above were used for α-Mg, while arbitrarily high CRSS values were selected for the particle phase such that they did not contribute to the accumulated strain. The increase in hardness provided by the greater volume fraction of intermetallic particles in the 9wt% Zn alloy resulted in only an approximately 20MPa increase in strength at yield, not the experimentally observed increase of nearly 100MPa. In order to achieve the observed difference in yield strength, a particle fraction of more than 30% would be necessary; this particle fraction is both unrealistically high and results in hardening behavior that no longer agrees with experiment. This additional hardening may result from either dislocation-pinning in the elastic-plastic transition regime, which cannot be captured using the VPSC model, or from the high particle aspect ratio.

Table 3.2: Voce hardening parameters utilized for the 4.5wt% Zn alloy simulations. For the 9wt% Zn alloy, the values of τ_0 were increased by 50%.

		τ_0 (MPa)	τ_1 (MPa)	θ_0	θ_1
basal	$\{0001\}\langle 2\bar{1}\bar{1}0\rangle$	40	100	225	0
prismatic	$\{10\bar{1}0\}\langle 2\bar{1}\bar{1}0\rangle$	110	100	500	0
pyramidal	$\{11\bar{2}2\}\langle\bar{1}\bar{1}23\rangle$	250	100	1500	0
tensile twin	$\{10\bar{1}2\}\langle\bar{1}011\rangle$	75	0	5	10
		$A^{th1} = 0.15$		$A^{th2} = 0.80$	

The similarity of Voce hardening parameters for both alloys indicates that the assumption of minimal hardening differences as a result of grain size and the fine particle distribution is likely to be valid. As a result, the observed differences in texture evolution should not be attributed to differences in hardening behavior. Additionally, this analysis justifies the use of the same set of Voce hardening parameters for all considered alloys. While the absolute flow stress values will not be comparable to experiment, the relative slip activities and the texture evolution can be directly compared.

For these alloys, the combination of Zn solid solution content and Mg-Zn intermetallic particles results in a basal:prismatic:pyramidal:twin CRSS ratio of

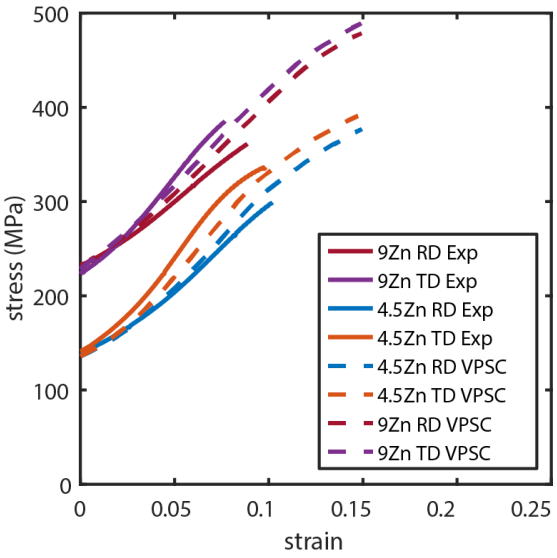

Figure 3.4: Experimental and VPSC-simulated stress-strain curves for the nominally 4.5wt% and 9wt% Zn alloys. The values of Voce parameters τ_1, θ_0, θ_1 are constant, and the τ_0 ratios of the slip systems are constant for the two alloy compositions.

1:2.75:6.25:1.88, which falls within the range reported for other polycrystal plasticity studies summarized in Table 1.1. While the strengthening effects of solute and the particle distributions cannot be deconvolved using this method, the technique does allow the effects of the coarse intermetallic particles to be isolated.

3.2.2 Differences in initial texture

Differences in the deformation texture may also result from differences in the initial texture. As the starting material had previously been extruded at 250°Cwith an extrusion ratio of 32:1, it is not randomly textured. The rolling deformation, a 40% reduction in thickness in a single pass, was simulated using a plane strain compression deformation gradient to a total reduction in thickness of 40% for each of the experimentally measured alloy starting textures. The hardening parameters determined for the 4.5wt% Zn alloy were utilized for both alloys.

The VPSC-predicted deformation textures are shown in Figure 3.5. As shown, the primary differences in texture evolution between the two alloys, namely the weaker basal peak and greater retained TD spread in the 9wt% Zn alloy, are both present in the VPSC textures. This suggests that, under these

deformation conditions, the observed differences in texture evolution may be primarily attributed to the differences in starting texture. The VPSC model over-predicts the strength of texture evolution, as commonly reported elsewhere in the literature [115–119].

3.2.3 Orientation stabilization by intermetallic particles

While the difference in starting texture is the primary reason for the difference in alloy deformation texture, it should be noted that the differences in starting texture for this material was also the result of deformation during extrusion. Assuming that the original ingot textures were similar and near random, the presence of an increased fraction of intermetallic particles did produce the observed differences in starting texture during the more severe extrusion deformation condition.

Comparison of the pre-deformation and as-rolled microstructures show that rolling has minimal effects on the particle distribution, particularly for the coarse population of intermetallic particles, as illustrated in Figures 3.1 and 3.6, respectively. It is possible that the α-Mg grains near these coarse particles experience restricted crystal rotation during deformation. This hypothesis is supported by the observation that a large number of the off-basal grains are located adjacent

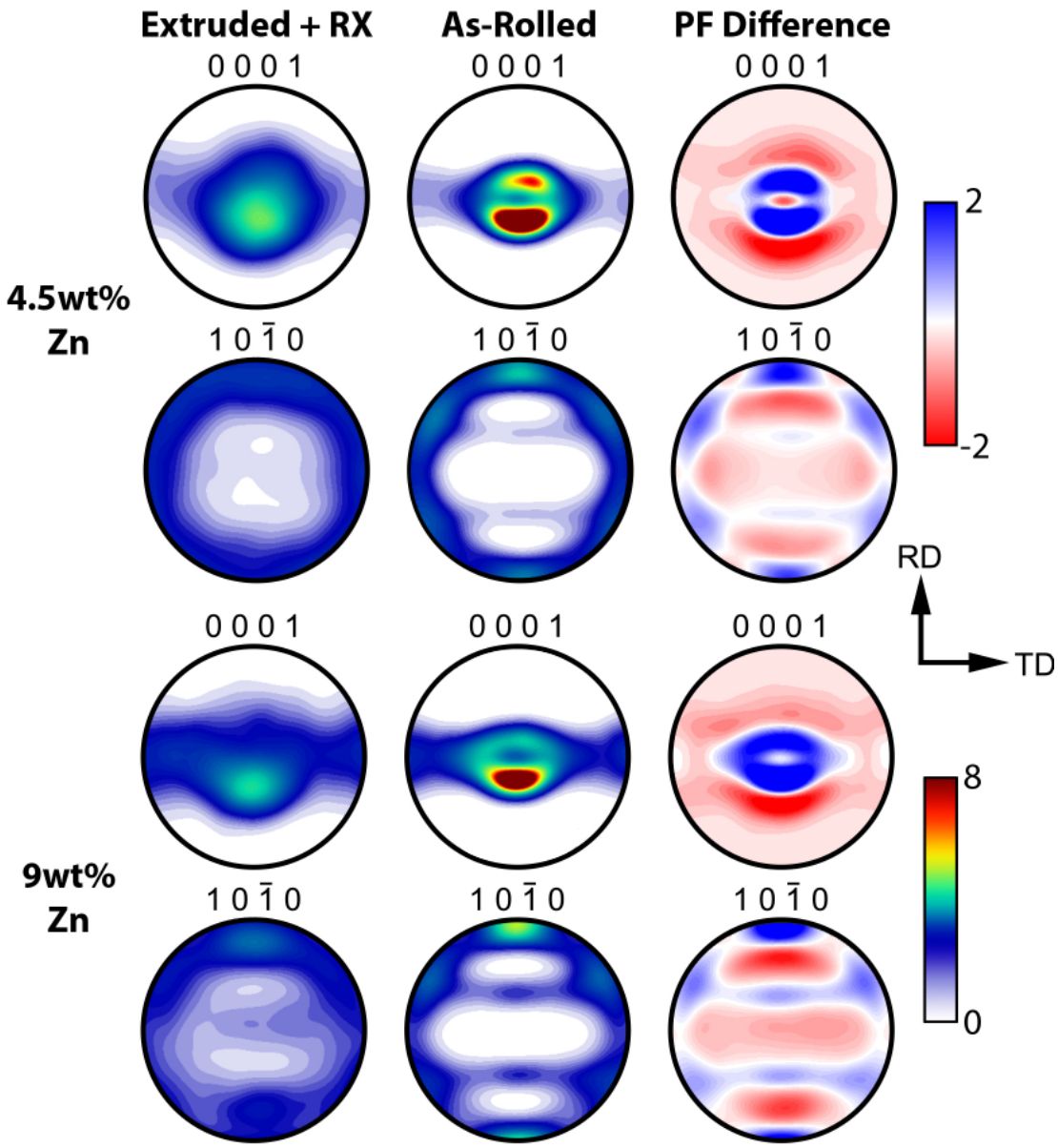

Figure 3.5: VPSC-calculated basal and prismatic PFs and PF difference plots showing texture evolution during plane strain compression to a total reduction in thickness of 40% for the 4.5wt% and 9wt% alloys. Identical hardening parameters were used for both simulations; the only difference is in starting texture.

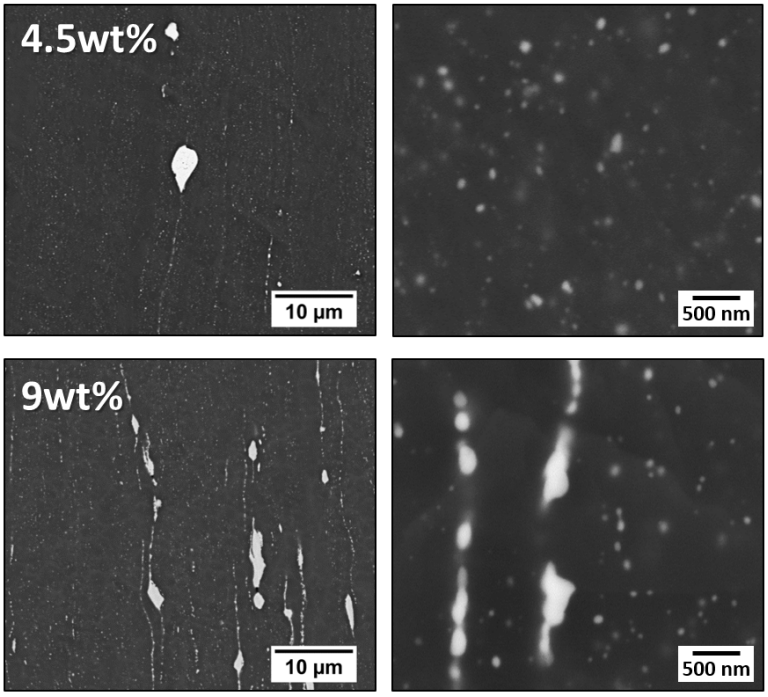

Figure 3.6: The as-rolled microstructures for the nominally 4.5wt% and 9wt% Zn alloys showing the distribution of intermetallic particles.

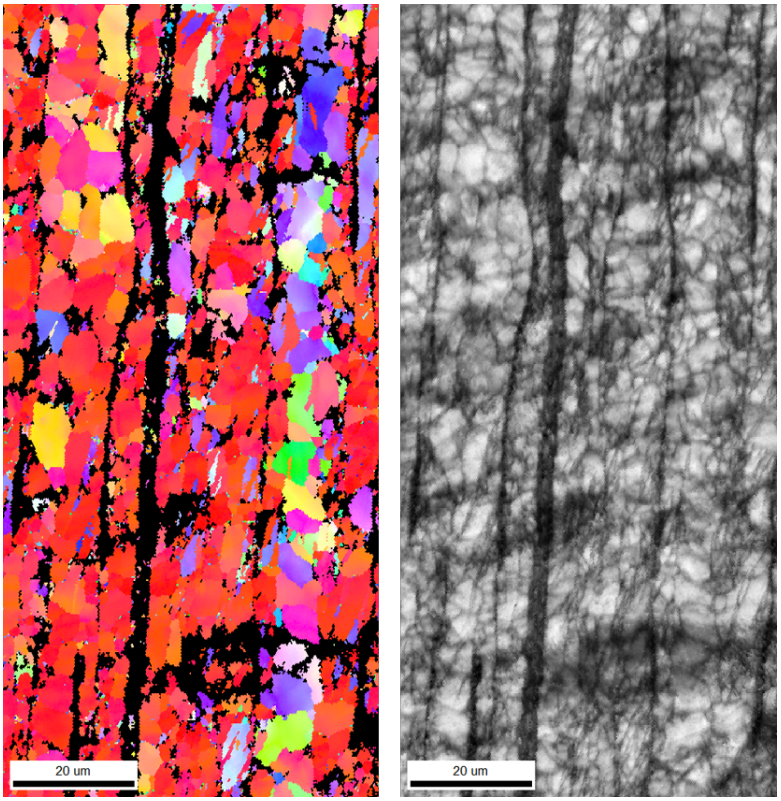

Figure 3.7: IPF and IQ maps illustrating the frequent spatial association between coarse intermetallic particles and grains with off-basal orientations. This sample is the 9wt% Zn alloy cold rolled to a 7% reduction in thickness.

to these stringers of intermetallic particles, as illustrated in Figure 3.7.

To examine the possibility of particle stabilization, a non-random neighbor assignment scheme was implemented in the VPSC model. This model was originally developed to account for the presence of microtextured regions in Ti alloys [120], and was modified to preferentially assign grains with off-basal ori-

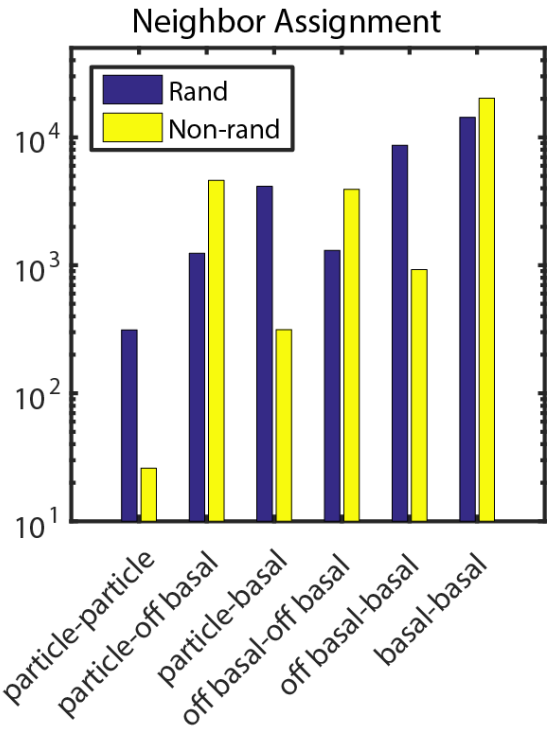

Figure 3.8: A comparison of neighbor pair frequency for random and non-random neighbor assignment schemes.

entations hard particle or other off-basal grains as neighbors. For this analysis, "off-basal" grains are defined to have an angle greater than 60° between the c-axis and the sheet normal direction. The distribution of neighbor assignments for random versus non-random neighbor assignment is compared in 3.8.

The effects of texture evolution are compared for the two neighbor assignment schemes under high strain rolling deformation conditions. A rolling pathway, as represented by plane strain compression, is selected because it has a

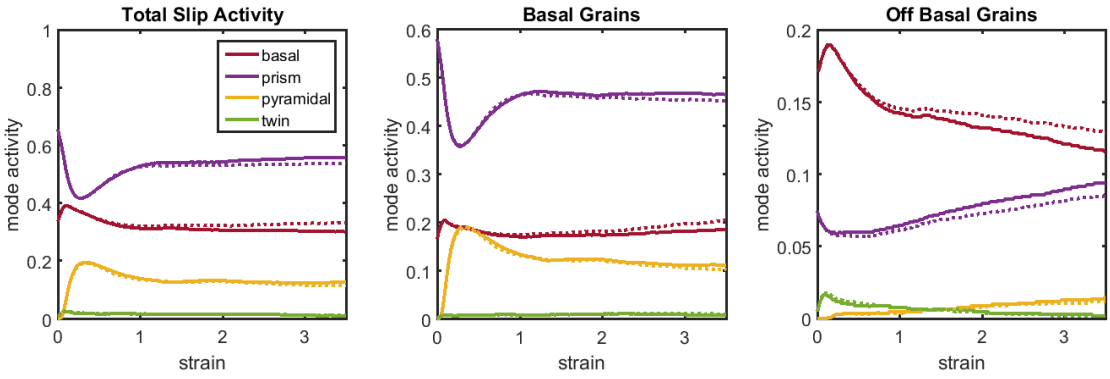

Figure 3.9: Differences in slip activity for basal and off-basal grains with the different neighbor assignment schemes. Solid lines represent the simulation with randomly assigned neighbors, while dashed lines indicate non-random neighbor assignment.

better-defined velocity gradient than extrusion into a rectangular cross section. The total strain is 3.5, similar in magnitude to the strain of extrusion with an extrusion ratio of 30. The analysis is performed with a particle volume fraction of 10%.

The slip activity for each neighbor assignment scheme is compared in Figure 3.9. As shown, the preferential assignment of off-basal and particle neighbor pairs increases basal slip and decreases prismatic slip in all grains, with the effect being much stronger in grains with off-basal orientations. The changes in pyramidal slip and tension twin activity are much smaller. Additionally, note that the observed particle stabilization effect is negligible at small and intermediate deformations, only becoming substantial after strains of approximately

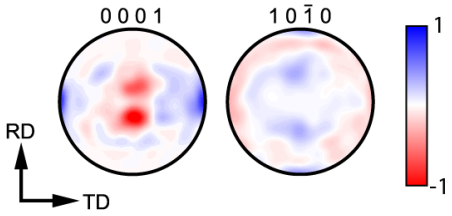

Figure 3.10: Pole figure difference map between the deformation texture of the particle stabilized and the random neighbor simulation. Blue areas indicate orientations more common in the particle-stabilized case, while red areas indicate areas that are weaker with particle stabilization.

1.5. This could explain why particle stabilization did not play a major role in the experimental rolling deformation discussed in Section 3.1, but does appear to have played a role in the preceding extrusion deformation.

Pole figure difference maps between the deformed textures for each neighbor assignment scheme are shown in Figure 3.10. In these maps, blue areas represent orientations that are more prevalent with non-random neighbor assignment while red areas indicate orientations that are less prevalent. As shown, under

this deformation pathway the particle stabilization effect promotes a substantially weaker basal peak and increased stability for many off-basal orientations. Due to the nature of the starting texture, this effect is strongest for grains with c-axes nearly parallel to the TD direction.

3.3 Application of existing particle deformation zone (PDZ) theory

The classical literature on PSN contains many descriptions of the formation of PDZs. Early descriptions relied on continuum plasticity models [121] or single slip dislocation configurations [94]. Later models utilized interaction rules for multiple slip systems, including fully independent deforation, vector-additive simultaneous deformation, and sequential deformation [122, 123]. More recently, crystal plasticity finite element modeling has also been attempted [124]; however, no generalized description of PDZ formation exists, even for the simplest case of a single large spherical particle embedded within a single crystal.

In the alloys used in this study, there are the additional complications of the coarse particles falling in high aspect ratio stringers primarily present at grain boundaries. Because of this spatial distribution, the influence of the coarse par-

ticles is highly inhomogeneous and the classical PDZ literature has limited relevance. This will be further demonstrated in Section 4.2, where the increased fraction of coarse intermetallic particles with increased Zn content had a negligible effect on the measured recrystallization kinetics. This is in contrast to the behavior of an alloy containing a homogeneous distribution of intermetallic particles, described in Chapter 5.

3.4 Summary of intermetallic particle effects on texture evolution

Experimental measurement of the as-rolled textures for the 4.5wt% Zn and 9wt% Zn alloys reveal that the material with lower Zn content develops a stronger basal peak and less TD spread in the basal pole figure after deformation. Microstructural characterization reveals that the starting material for each alloy has a similar distribution of fine intermetallic particles and initial grain size; polycrystal plasticity simulations reveal that the mechanical behavior of each alloy can be described by the same CRSS ratios and identical hardening parameters. Using these hardening parameters, it is demonstrated that the primary reason for the difference in deformation texture after small-deformation

rolling is a difference in the pre-deformation texture, not an effect of the intermetallic particles.

However, for large-strain deformation pathways such as the extrusion used to homogenize the starting material, differences in deformation texture still develop even starting with an near-random ingot texture. A non-random neighbor assignment scheme is implemented in the VPSC polycrystal plasticity model, which preferentially assigns off-basal grains to have non-deforming intermetallic particles or other off-basal grains as neighbors. This particle stabilization is demonstrated to be a plausible explanation for the increased frequency of the TD tilt orientations in the 9wt% alloy during large deformations.

Chapter 4

Control of texture during recrystallization

The static recrystallization behavior of the Mg-Zn binary alloys from the deformed state discussed in Chapter 3 is examined as a function of recrystallization temperature. These alloys were processed such that they maintain approximately equal grain sizes and fine particle distributions, with varied distributions of coarse ($>1\mu$m) intermetallic particles. Differences in texture evolution, recrystallization kinetics, and the underlying dislocation structure mechanisms are examined.

4.1 Static recrystallization textures of Mg-Zn binary alloys

The recrystallized texture is observed to vary strongly with recrystallization temperature, as shown in Figure 4.1 for the 9wt%Zn alloy. These textures correspond to the end of recrystallization as determined by microhardness measurements, before any grain growth occurred. As shown, recrystallization at lower temperatures results in stronger basal textures and less spread of the basal peak toward the transverse direction retained from the as-deformed state. Recrystallization at higher temperatures results in a more diffuse, weakened basal texture with greater retained TD spread. This trend was observed for all three Mg-Zn alloys, but it is most pronounced in Mg-9wt%Zn due to the greater TD spread of the basal pole figure in the as-deformed state (Chapter 3).

However, recrystallization at 300°C, where there is substantial dissolution of the fine intermetallic particles, results in substantial texture strengthening as shown in Figure 4.2. Almost no TD spread is retained in the basal pole figure. Additionally, recrystallization is accompanied by an increase in average grain diameter to 24.9μm. Strengthening of the basal peak is commonly reported during grain growth in magnesium alloys, as discussed in Section 1.3. Despite the substantial grain growth observed minimal strengthening of the six-

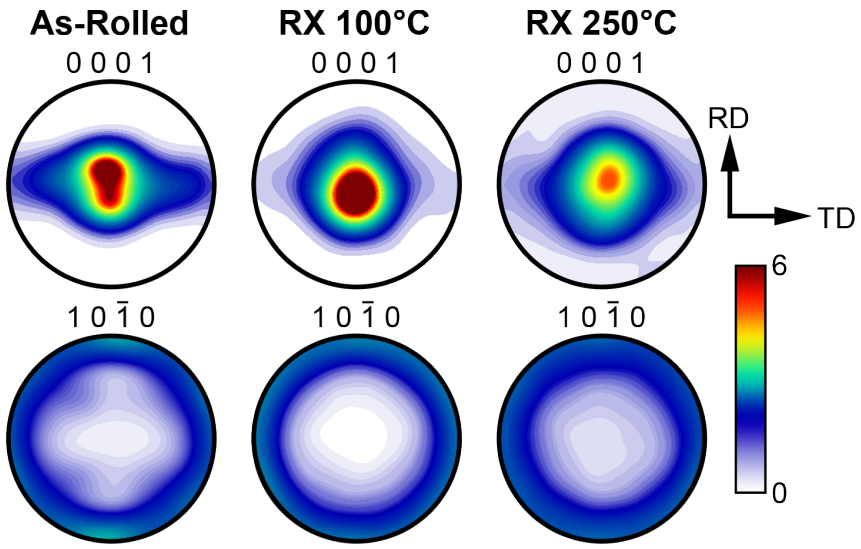

Figure 4.1: Textures for the Mg-9Zn alloy at the completion of recrystallization for two temperatures, 100°C and 250°C.

fold symmetry is observed in the prismatic pole figure. This is in contrast to recent observations by Bhattacharyya *et al.* [73], where sixfold symmetry of the prismatic pole figure was observed during grain growth subsequent to recrystallization. While this microstructural condition highlights the importance of impeding grain growth, it is not comparable to recrystallization at the other considered temperatures. As a result, it is not considered in the mechanisms discussed in Section 4.3.

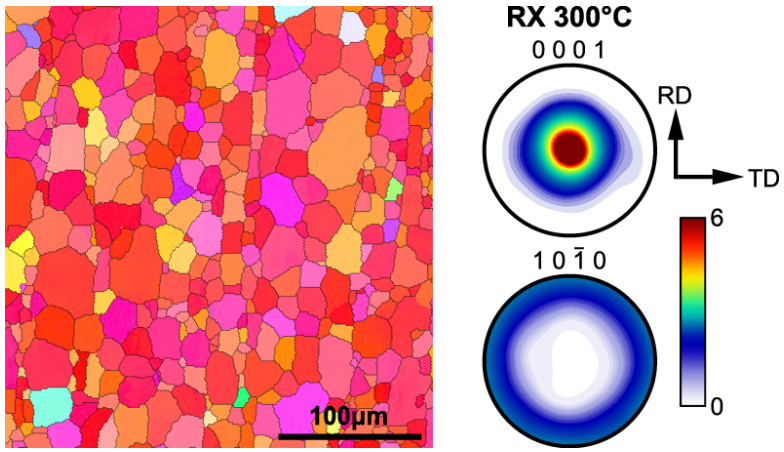

Figure 4.2: IPF map and pole figures for 9wt% Zn material recrystallized at 300°C.

4.2 JMAK kinetics measurement

The kinetics of recrystallization at temperatures ranging from 100°C to 300°C in 50°C increments were examined using Vickers microhardness measurements to capture the fraction recrystallized, as described in Section 2.1.2. Each data point in Figure 4.3 is the average of 10 measurements. Error bars are not shown in the figure for clarity, but the average standard deviation of the measurements for a data point is 3HV. The evolution of microhardness over time for each of the three binary Mg-Zn alloys is presented in Figure 4.3. As shown, the rate of the decrease in hardness over time is much greater at higher temperatures. For all temperatures below 300°C, the hardness plateaus at similar values, indicating the conclusion of recrystallization. At the 100°C and 150°C an initial plateau in hardness is observed, likely corresponding to a recovered mi-

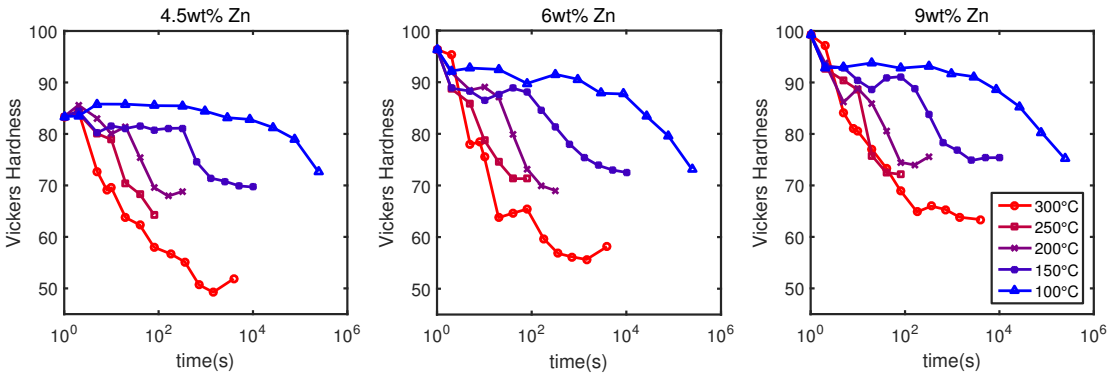

Figure 4.3: Evolution of Vickers microhardness during heat treatment at temperatures between 100°Cand 300°C.

crostructure.

These microhardness measurements were subsequently converted to fraction recrystallized, as discussed in Chapter 2, and the recrystallization kinetics were analyzed using the JMAK model [89]. In this model, the fraction recrystallized, X_V, is related to the annealing time, t, by the equation:

$$X_V = 1 - exp(-Bt^n) \tag{4.1}$$

where B contains geometric terms and the nucleation and growth rates in the analytical form and n is the Avrami exponent. Experimentally, B and n are used as a fitting parameter. The Avrami model assumes that nucleation and growth rates are spatially and temporally constant during recrystallization and that the nuclei are randomly distributed. The limiting cases of site-saturated nucleation and a constant nucleation rate in three dimensions result in Avrami exponents

Table 4.1: Avrami exponent for each alloy composition at each recrystallization temperature

	4.5wt%Zn	6wt%Zn	9wt%Zn	Avg.
100°C	0.52	0.54	0.47	0.51
150°C	0.68	0.89	0.81	0.79
200°C	1.39	1.45	1.31	1.38
250°C	2.07	2.56	2.28	2.30
300°C	0.35	0.34	0.38	0.35

of 3 and 4, respectively.

Linearized plots of fraction recrystallized versus time are presented in Figure 4.4 for all considered alloys and temperatures, and the calculated Avrami exponents are presented in Table 4.1. As shown, there is no substantial variation in recrystallization kinetics between the three Mg-Zn binary alloys. This suggests that, under these conditions, PSN of recrystallization is not playing an important role in determining the recrystallization kinetics. This is in contrast to the results presented for a different alloy and processing path in Chapter 5, where a highly homogeneous distribution of particles substantially accelerates the progress of recrystallization.

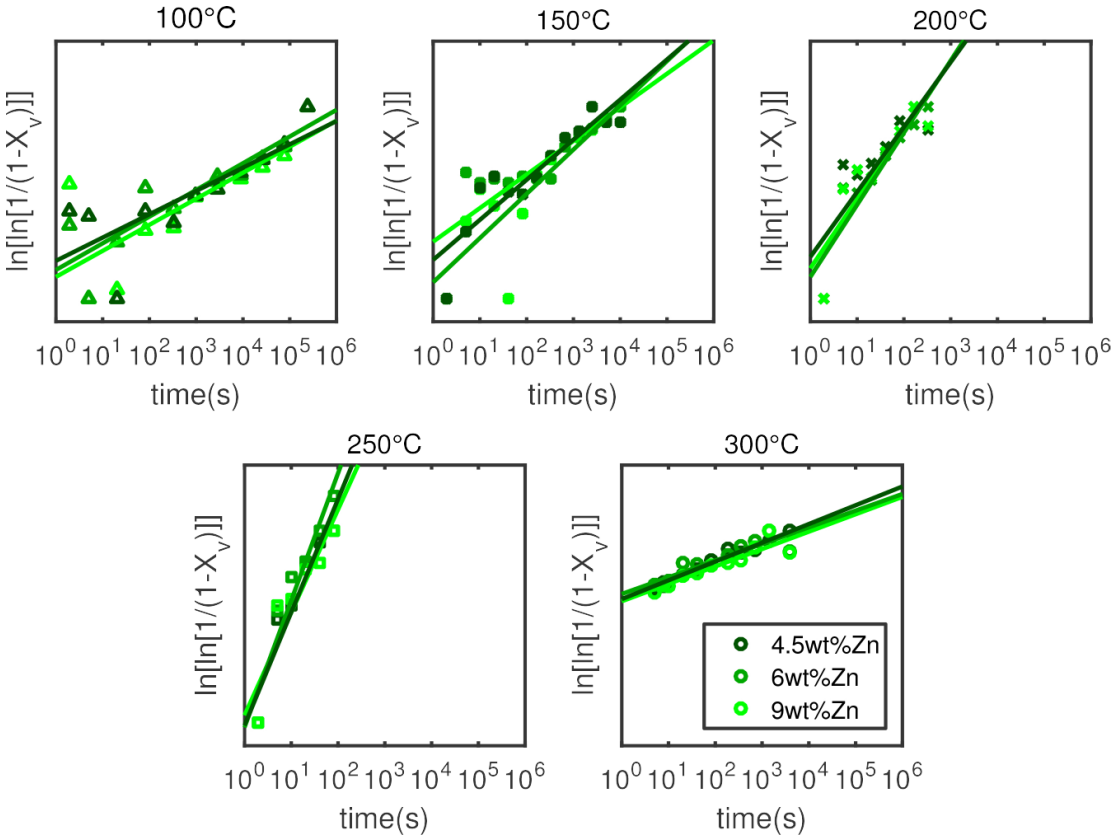

Figure 4.4: JMAK kinetics as a function of temperature for each Mg-Zn binary alloy.

Interestingly, the slope of the linearized plot (i.e. the Avrami exponent) increases with increasing temperature from 100°C to 250°C, then dramatically decreases for 300°C. However, even at the highest value of the Avrami exponent at 250°C, the observed values are substantially lower than the theoretical values of 3 for site-saturated nucleation and 4 for constant nucleation rate.

Values of the Avrami exponent lower than the theoretical values are commonly reported in the literature for alloy classes including magnesium, alu-

minum, copper, and iron-based alloys [42, 89, 125–128]. Low values of the Avrami exponent indicate that the assumptions made in the Avrami model (spatially and temporally constant nucleation and growth rates) are incorrect for the considered system. Because the Avrami assumptions are unrealistic for real materials, deviation from the model is unremarkable [89].

However, the Avrami exponents generally reported in the literature do not depend sensitively on temperature. Near-constant Avrami slopes have been reported for an Fe-Si alloy over a 500°C range [129]. The observed variation indicates that substantial changes in the spatial and temporal homogeneity of recrystallization occur with varied heat treatment temperature, with the nucleation and growth becoming more heterogeneous at lower temperatures. This was investigated via EBSD, as described in Section 4.3.1.

4.3 Microstructure evolution during recrystallization

The differences in texture evolution observed between the different examined temperatures, particularly those below 300°C, are likely to result from the variation in recrystallization kinetics. To investigate the underlying mechanisms

resulting in this shift in kinetics, EBSD measurements were conducted on microstructures partially recrystallized at varied temperatures. Additionally, TEM investigation was conducted on the material cold rolled to approximately 7% reduction in thickness to probe the early stages of dislocation substructure development.

4.3.1 EBSD measurement

The microstructures of Mg-9wt%Zn heat treated to near complete recrystallization at different recrystallization temperatures were examined to investigate the changes in spatial and temporal homogeneity of recrystallization with varied heat treatment temperature.

The microstructure of rolled material heat treated for 16 hours at 150°C, a relatively low temperature, is shown in Figure 4.5. The basal grains (near-red in the IPF map) are approximately equiaxed and bright contrast in the IQ map, indicating that they are recrystallized. However, many of the off-basal grains (yellow-green in the IPF map) remain elongated and dark in the IQ map, indicating that recrystallization is delayed in comparison to the basal grains.

In comparison, the microstructure of rolled material heat treated for 5 minutes at 250°C is shown in Figure 4.6. In this case, both the basal and off-basal

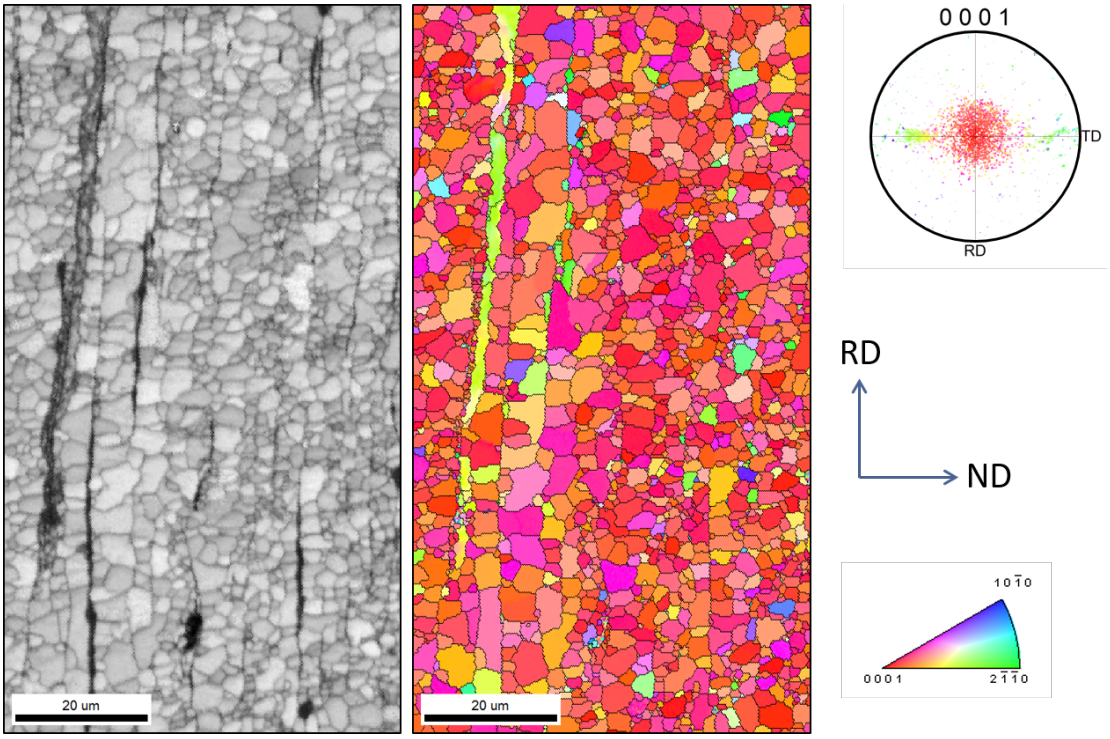

Figure 4.5: Mg-9wt% Zn alloy heat treated at 150°C for 16 hours. An IQ map, an IPF map referenced to the normal direction, and the discrete basal pole figure with the same coloring as the IPF map are shown. The basal grains (near-red) are fully recrystallized, while the off basal grains (yellow-green) remain in the as-deformed state.

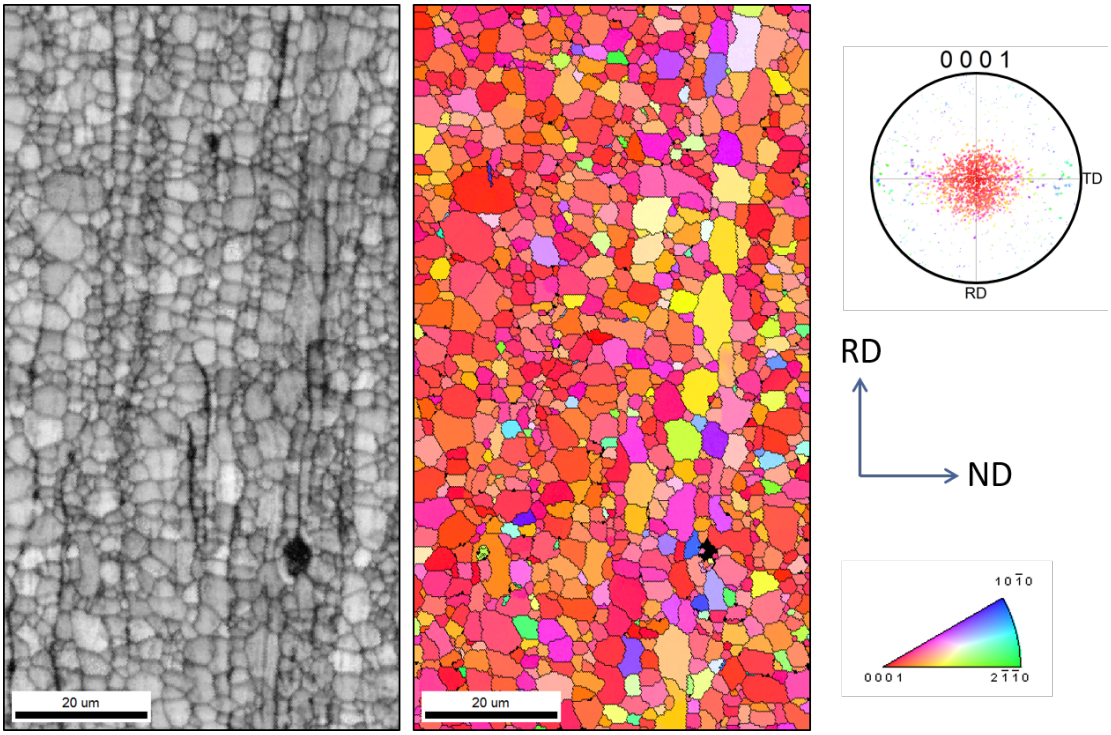

Figure 4.6: Mg-9wt% Zn alloy heat treated at 250°C for 5 minutes. The basal grains (near-red) are fully recrystallized, while the off basal grains (yellow-green) remain in the as-deformed state.

grains are approximately equiaxed and appear bright in the IQ map, indicating that recrystallization has occurred in all orientations. Additionally, many of the off-basal grains have a relatively large grain diameter, suggesting that there is little inhibition to their growth after nucleation occurs.

At lower temperatures, the delay in recrystallization of the off-basal grains likely contributes to their depletion during recrystallization. The additional time required for nucleation in the off-basal regions allows the already-recrystallized basal grains to grow into the high-energy deformed off-basal grains, increasing the volume fraction of material with basal orientation and depleting the off-basal orientations from the microstructure and thereby contributing to texture strengthening.

One possible explanation for the differences in recrystallization behavior between the basal and off-basal grains would be a difference in thermodynamic driving force for recrystallization. The recrystallization process is driven by stored energy from prior deformation processes. Because grains of different orientations are favorable for different deformation processes, it is possible that they may have different levels of stored energy at the conclusion of deformation. While it is challenging to directly measure the stored deformation energy of a single grain, it is likely to correlate with measures of local misorientation that may be measured via EBSD such as GOS as described in Section 2.3.2.

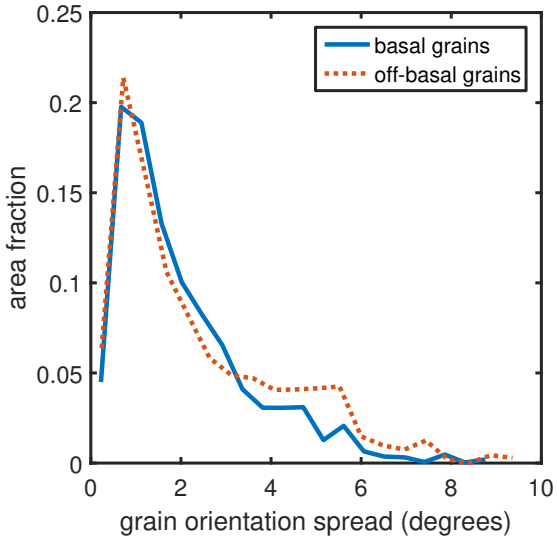

Figure 4.7: Grain orientation spread profiles for grains with basal pole tilt below (basal) and above (off-basal) 25°. The grain orientation spread profiles are approximately equal.

The a plot of area fraction of grains with particular values of GOS is presented in Figure 4.7, comparing grains with basal and off-basal orientations. As shown, the profiles are nearly identical, indicating that the difference in recrystallization behavior between basal and off-basal grains is not likely to be a result of different thermodynamic driving forces. This suggests that the more likely cause of differences in recrystallization behavior is in the kinetics of dislocation nucleation, which is related to dislocation substructure.

4.3.2 Dislocation substructures

The dislocation substructure developed after cold rolling to a 7% reduction in thickness is compared for basal and off-basal grains in Figure 4.8 with TEM micrographs and explanatory schematic diagrams. In the basal grain, multiple non-parallel low angle grain boundaries composed of dislocation walls are present. The wall on the left is primarily composed of basal dislocations, while the wall on the right is composed of prismatic dislocations with multiple $\langle a \rangle$-type Burgers vectors which cooperatively contribute to a single dislocation wall. In the off-basal grain, a twin is present in bright contrast. Also visible are large number dislocations in the non-twin region. These dislocations organize themselves into bands of high density near horizontal in the image. These bands

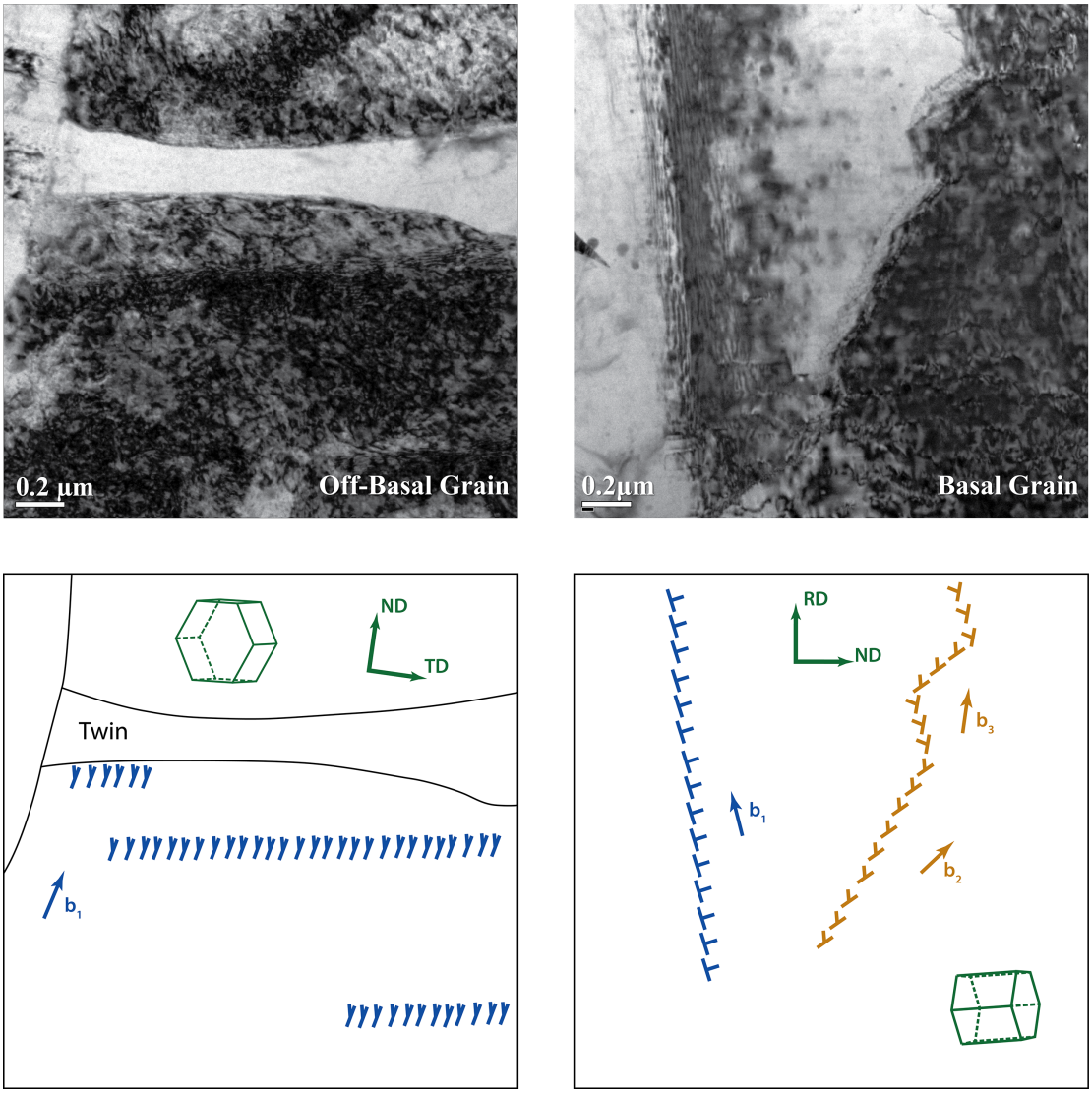

Figure 4.8: Comparison of dislocation substructure in basal versus off-basal grains. Upper images show TEM bright field images, and the lower images are schematic representations showing the locations of low angle boundaries and the orientation of the foil and the crystal.

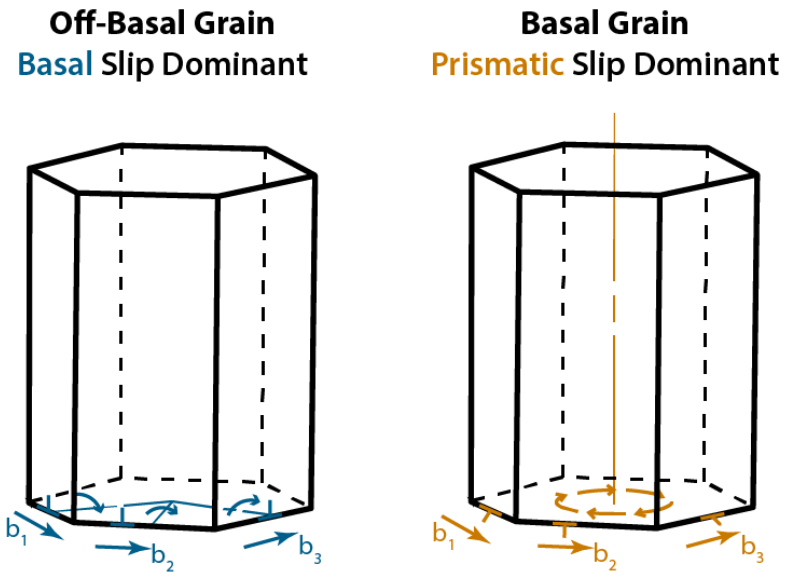

Figure 4.9: Comparison of the preferred Taylor axes in basal and off-basal grains, based on the active deformation mechanisms. In basal grains, prismatic dislocations of all three Burgers vectors share a common Taylor axis, while in off-basal grains the three basal Burgers vectors have different Taylor axes.

of high dislocation are primarily composed of dislocations of a single Burgers vector, as shown schematically.

These differences in substructure result directly from the active deformation mechanisms in grains of basal and off-basal orientations, as discussed in detail in Chapter 3. In grains near a perfect basal orientation, easy basal slip is unfavorable during rolling; instead, prismatic slip must accommodate deformation under this stress state. However, in off-basal grains basal slip is heavily favored

due to its lower CRSS. Basal and prismatic dislocations also have distinct Taylor axes, as shown in Figure 4.9. Basal dislocations have Taylor axes parallel to $\langle 10\bar{1}0\rangle$, perpendicular to the Burgers vector and in the basal plane. However, prismatic dislocations all share a common Taylor axis parallel to the $\langle c\rangle$-axis. As discussed by Hadorn *et al.* [66], with populations of dislocations with different Burgers vectors acting cooperatively it is possible to accumulate greater subgrain misorientation before rotation is limited by elastic strain than in the case of only a single population of dislocations.

This difference in Taylor axes results in differences in the efficiency of subgrain formation in basal versus off-basal grains, as demonstrated in Figure 4.8. The off-basal grain successfully forms dislocation walls, however, they are long and parallel, which does not result in a viable recrystallization nucleus. In the basal grain, the presence of multiple non-parallel dislocation walls which may have greater possible misorientations enable more efficient sub-division of the deformed grain, leading to more effective nucleation of recrystallization in the basal grains (which preferentially contain prismatic dislocations). This variation in relative nucleation rates with temperature may explain the differences in recrystallization kinetics between the basal and off-basal grains observed via EBSD in Section 4.3.1 and ultimately explain the temperature-dependent texture evolution during recrystallization.

This orientation-dependent nucleation may provide an explanation for another recrystallization phenomenon commonly reported in Mg alloys, twinning-related recrystallization [6]. This recrystallization mechanism, discussed in Section 1.2.1, is most frequently reported in coarse-grained material, particularly during dynamic recrystallization. During deformation, grains are observed to twin, and the material within the twin preferentially recrystallizes substantially prior to the parent grain. As discussed in Chapter 6, the tension twin that is favored in conventional Mg alloys reorients the crystal to a near-basal orientation during common deformation pathways. This near-basal orientation would rely on prismatic slip during deformation, allowing it to evolve substructure favorable for nucleating recrystallized grains before the parent grain.

4.3.3 Grain growth after recrystallization

At all heat treatment temperatures, the recrystallized grain size is approximately constant, with the median grain size varying between 3.5 and 4.0μm from 100°C to 250°C. This similarity in grain size is likely the result of Zener drag [130]. According to the Zener analysis, when the particle pinning pressure is equal to the driving pressure for grain growth a limiting grain size is achieved. This limiting grain size can be calculated using the relationship [89]:

Table 4.2: Zener-limiting grain size for various values of α

	α=0.25	α=0.50	α=1	Exp.
9wt% Zn	0.8μm	1.7μm	3.4μm	3.5-4.0μm

$$D_{Zener} = \frac{4\alpha r}{3F_V} \tag{4.2}$$

In this equation, r is the particle radius, F_V is the particle volume fraction, and α is a geometric parameter near one. While there have been numerous attempts to refine the Zener analysis [131], most of the predictions result in a limiting grain size relationship similar to that predicted by the Zener equation, with the value of α between 0.25 and 0.5.

For the fine particle distribution in the 9wt% Zn alloy, as described in Chapter 3, the Zener analysis produces the values shown in Table for several values of α. As shown, the experimentally observed grain diameters are very near the predicted Zener limit for values of α near 1.0 as in the original Zener analysis. This suggests that the distribution of fine intermetallic particles is effective in restricting the recrystallized grain size. As discussed in Section 1.3, the prevention of grain growth after impingement is critical to prevent texture strengthening.

4.4 Summary of texture evolution during recrystallization

Recrystallization at varied temperature of rolled Mg-Zn binary alloys is demonstrated to alter the strength and TD spread of the basal pole figure of the recrystallized material, with stronger textures resulting from lower temperatures. Lower temperatures also resulted in lower Avrami exponents, suggesting greater spatial and temporal inhomogeneity in the nucleation of recrystallization. No dependence of the Avrami exponent on the fraction of coarse intermetallic particles was observed. EBSD measurements near the completion of recrystallization demonstrate that off-basal regions of the microstructure nucleate recrystallization substantially later than regions with basal orientations. This delay in off-basal nucleation of recrystallization is exacerbated at lower temperatures, resulting in growth of the basal recrystallization front into the off-basal deformed regions which promotes texture strengthening. TEM observations of the deformed state developed in basal versus off-basal grains reveal differences in dislocation substructure. In basal grains, high prismatic slip activity allows multiple non-parallel dislocation walls to subdivide the parent grain, resulting in efficient nucleation. Conversely, in off-basal grains easy basal slip leads to only a single population of dislocation walls and inefficient nucleus formation. This

mechanism may also be responsible for observations of preferential recrystallization within twins in comparison to the parent grain in coarse-grained material.

Chapter 5

Texture evolution in commercial alloy AXJ810

The texture modification mechanisms investigated in Chapters 3 and 4 are investigated during warm deformation in a commercial alloy, AXJ810 supplied by nanoMAG, LLC. The use of this alloy allows for further investigation of the simultaneous and complementary solute and intermetallic particle effects. In Section 5.1, the as-molded starting material was heat treated to produce three different microstructural starting conditions, and the texture and microstructural evolution was examined during warm compression. Subsequent static recrystallization behavior is also discussed. Section 5.2 describes the static recrys-

Table 5.1: Nominal phase fractions at selected processing temperatures in the AXJ810 alloy, as calculated using Pandat [1].

Phase	20°C	300°C	450°C
α-Mg	84.4%	93.6%	98.2%
C36/C15	1.3%	1.3%	1.8%
β-$Mg_{17}Al_{12}$	14.3%	5.1%	0%

tallization behavior of commercially thermomechanically processed sheet and compares it to the laboratory processed material. Finally, the influence of pinning particles during recrystallization is examined by comparing the recrystallization behavior of the particle-containing matrix with the externally solidified grains in Section 5.3.

5.1 Hot compression of as-molded AXJ810

Three different microstructural conditions for the AXJ810 alloy, shown in Figure 5.1, were developed by heat treatment, as described in Section 2.2.2. These microstructures sample the spectrum of decreasing intermetallic particle volume fraction and increasing solid solution content.

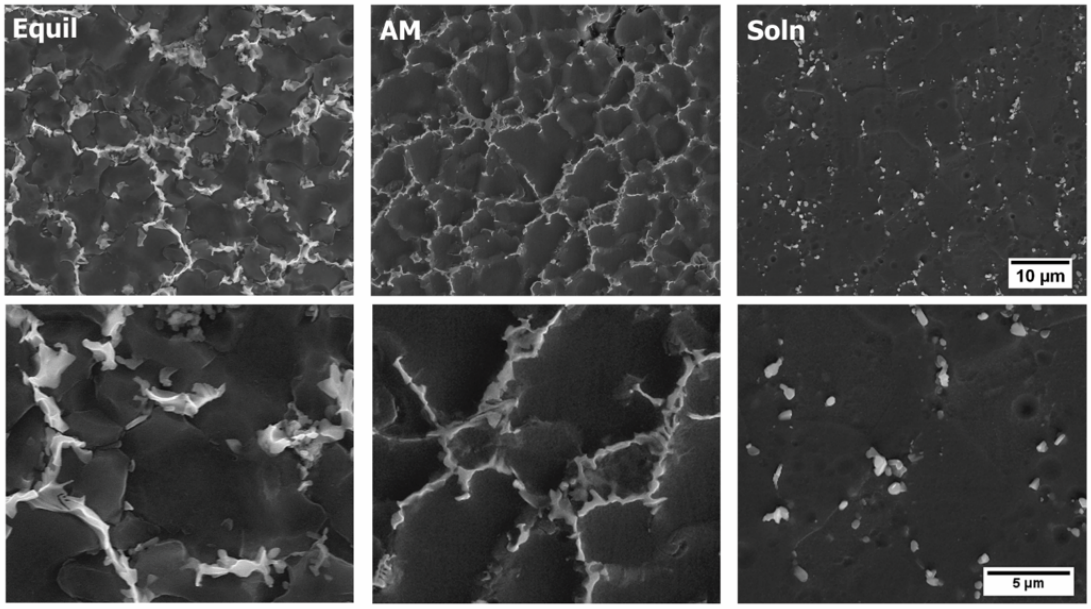

Figure 5.1: Microstructures of the three initial heat-treated conditions: equilibrated, as-molded (AM), and solution-treated, each shown at two magnifications. Reprinted with permission from Reference [96].

In the "as-molded" (AM) condition, the material contains both non-equilibrium solute content as well as β and Laves phase intermetallic particles. In this state, the particles are present as clusters of individual particles 1-2μm in diameter at the grain boundaries and elongated in the boundary plane. The "equilibrated" heat treatment was selected to reduce the inhomogeneity and the quantity of non-equilibrium solute content present at the end of solidification. This condition contains the least solid solution content and the greatest fraction of intermetallic particles, with the increase in volume fraction primarily occurring as thickening of pre-existing particles in the boundary plane. The "solutioned" heat treatment condition fully dissolved the β phase, while the Laves phase particles remain intact. This condition represents the greatest solid solution content and the smallest fraction of intermetallic particles. The thixomolding process results in a fine initial grain size [132, 133] of 5.9μm, and minimal increase was observed during the equilibration treatment to 6.3μm. A slightly greater increase to 9.7μm was observed during the solution heat treatment, but the Laves phase prevented more substantial grain growth.

Compression tests at 250°C, as described in Section 2.2.2, were conducted to three levels of total plastic strain. Representative IPF maps of longitudinal sections at 0.3 strain are shown in Figure 5.2, with the compression direction vertical and the map coloring referenced to the compression direction. Defor-

mation in the externally solidified grains includes extensive twinning and shear localization. However, no macroscopic shear bands were observed in the fine-grained matrix at any measured strain level. In the fine-grained regions minimal twinning is observed; less than 2% of the the total boundary length outside of the externally solidified grains has a twin misorientation at any strain level. Substantial internal misorientation is observed in within the fine grains.

Substantial fractions of dynamically recrystallized (DRX) grains are observed in samples strained to 0.3 and 0.7 for all initial microstructures, with occasional dynamically recrystallized grains observed at 0.1 strain. The average dynamically recrystallized grain size is compared at 0.7 strain for the three starting microstructures in Table 5.2. The equilibrated structure contained the smallest recrystallized grain size, while the AM and solutioned microstructures contained DRX grains of nearly the same size. Due to the fine grain size in the starting microstructures, the DRX grains are only a factor of 3-4 smaller than the initial grain size.

Texture evolution at each of three strain levels was measured via EBSD, with the resulting basal pole figures displayed in Figure 5.3. All measured samples developed basal deformation textures, but the texture strength and rapidity of evolution varied between the initial microstructural conditions. Texture evolution in the solution-treated material was most rapid, with the basal peak in-

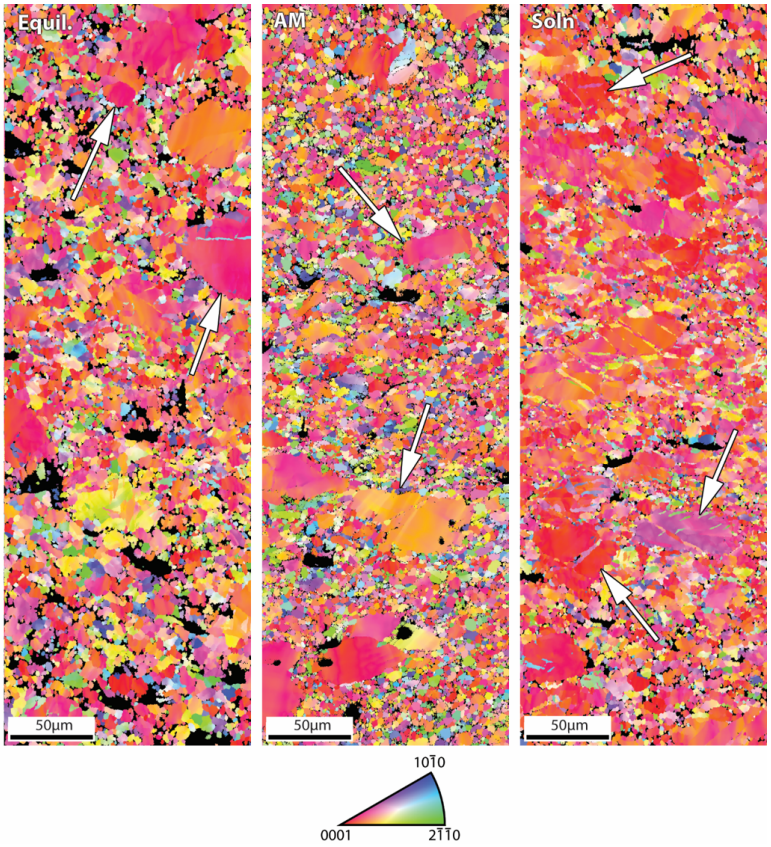

Figure 5.2: IPF maps showing longitudinal sections of the three microstructural conditions at 0.3 strain. Color with reference to the compression direction. Arrows indicate examples of externally solidified grains. No shear bands are observed outside of the externally solidified grains. Reprinted with permission from Reference [96].

Table 5.2: Average recrystallized grain size after 0.7 strain for each initial microstructural condition.

Designation	Initial grain size (μm)	DRX grain size (μm)
Equlibrated	6.3±2.2	1.5±0.6
As-molded	5.9±2.6	2.5±1.0
Solutioned	9.7±2.8	2.3±1.0

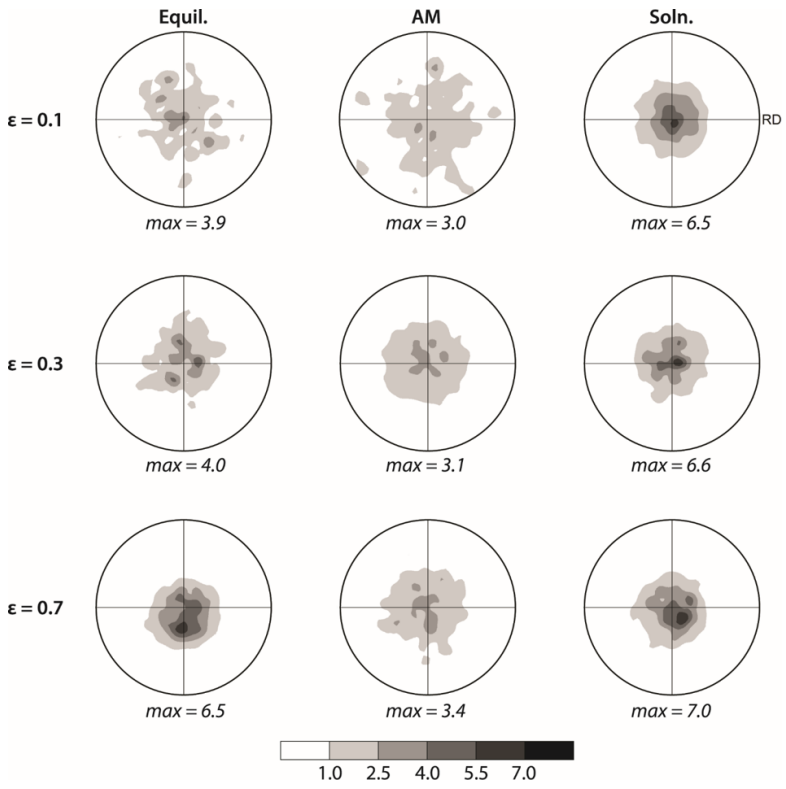

Figure 5.3: Basal pole figures for the three starting microstructures compressed to different strain levels. Reprinted with permission from Reference [96].

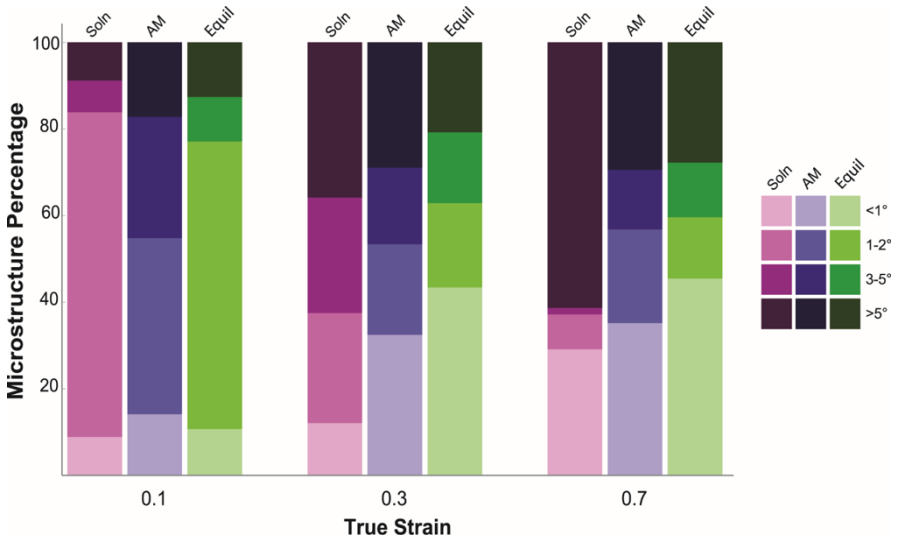

Figure 5.4: GOS evolution of three different microstructural starting conditions at varied strain. Reprinted with permission from Reference [96].

tensity increasing substantially even after 0.1 strain. More modest increases in basal peak strength were observed for the equilibrated and as-molded microstructures. No substantial increase in basal peak intensity was observed between 0.1 and 0.3 strain for any of the microstructural conditions. At 0.7 strain, the peak basal intensity of the solution-treated and AM material increase lightly, while the peak intensity of the as-molded material increases substantially. Overall, the as-molded material, containing intermediate levels of both solute and coarse intermetallic particles, develops the weakest basal peak.

The development and evolution of internal misorientation during deformation within grains was tracked via GOS measurements for each starting condi-

tion. High values of GOS correspond to deformation gradients within the material, whereas values of GOS less than 1° indicate the occurrence of dynamic recrystallization. At 0.1 strain, the solution-treated and equilibrated material have similar GOS distributions, with many grains having GOS values of 1-2°. However, the as-molded material has many more grains with higher GOS values, indicating the presence of numerous low angle boundaries and orientation gradients. At the intermediate strain level, 0.3, the GOS profiles of all three starting conditions indicate a high proportion of the microstructure with GOS greater than 2°. However, the as-molded and equilibrated samples (i.e. the samples with a greater fraction of coarse intermetallic particles) have substantially greater microstructure fractions with GOS values below 1°, indicating that more dynamic recrystallization has occurred. This trend continues at the highest strain level, 0.7, where the solution treated material retains the greatest fraction of unrecrystallized grains. The equilibrated material, with the greatest fraction of coarse intermetallic particles, has the greatest fraction of dynamically recrystallized grains at both the intermediate and high strain levels.

Figures 5.5 and 5.6 show representative examples of grain reference orientation deviation maps at 0.1 and 0.3 strain, respectively. While these maps are from material that originated in the as-molded condition, the effects of intermetallic particles demonstrated are relevant to all three starting microstruc-

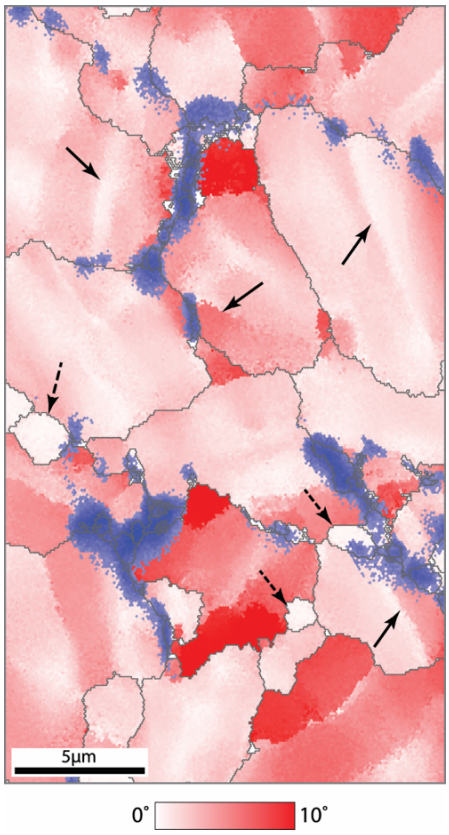

Figure 5.5: GROD map showing examples of LAGBs (solid arrows) frequently observed in association with coarse intermetallic particles. Dashed arrows indicate recrystallized grains. Al EDS data is shown in blue, indicating the locations of intermetallic particles. Image is of the as-molded microstructure compressed to 0.1 strain. Reprinted with permission from Reference [96].

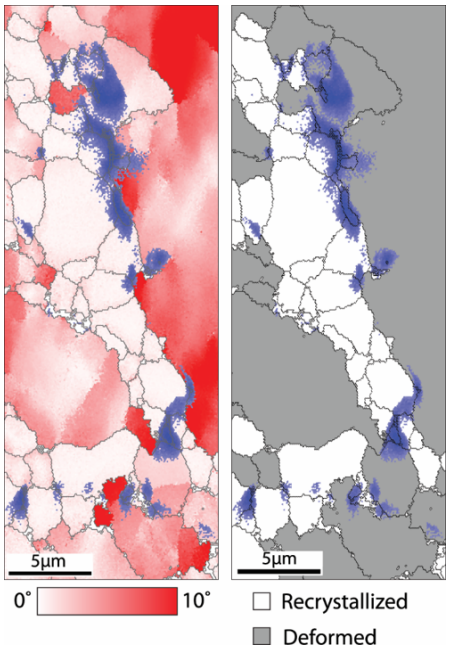

Figure 5.6: Colonies of recrystallized grains nucleating in association with intermetallic particles in as-molded material at 0.3 strain. Al EDS data is shown in blue, indicating the locations of intermetallic particles. Nearly all recrystallized grains occur in colonies associated with intermetallic particles. Reprinted with permission from Reference [96].

tures. Aluminum EDS data is overlaid in blue to visualize the effects of the Al-rich intermetallic particles on the homogeneity of deformation and recrystallization. Narrow solid lines in gray indicate boundaries with misorientation angles greater than 5°.

At 0.1 strain, the most significant features on the GROD maps are the deformation inhomogeneities, indicated with solid arrows. These inhomogeneities are most commonly bands of steep misorientation which span the width of the grain, approximately 5-10μm in length. The bands are typically located adjacent to coarse intermetallic particles and are composed of regions of nearly constant orientation separated by nearly planar LAGBs. A minimum of 30 of these boundaries were characterized for misorientation axis and angle for each microstructural starting condition. In all three sample types, the misorientations present across the boundaries are 1.5-5° about $\langle uvt0 \rangle$, most frequently near $\langle 10\bar{1}0 \rangle$. This indicates that these LAGBs are most likely composed of basal dislocations. Only a small number of these features were observed in the solution-treated material due to the low fraction of intermetallic particles; however, they were still present. A small number of recrystallized grains were also observed, indicated with dashed arrows.

The GROD maps of material strained to 0.3 reveal the spatial distribution of recrystallization nuclei. For clarity, a second map is shown in Figure 5.5 where

the recrystallized (GOS$<1^\circ$) grains are shown in white. These "nuclei" tend to be fine, equiaxed, and with minimal internal misorientation. In the equilibrated and as-molded conditions, the recrystallized grains are most frequently found in colonies near coarse intermetallic particles, further supporting the importance of PSN in influencing recrystallization kinetics. In the solution treated material, some nuclei were observed near the isolated Laves phase particles, but other nuclei were observed without an associated particle. Some of these nuclei may have formed at pre-existing high angle grain boundaries, but this is difficult to verify due to the similarity of grain size in the deformed and recrystallized material.

IGMA data is presented for the three starting microstructures at 0.1 strain in Figure 5.7, alongside the Taylor axes for typical slip systems active in Mg alloys. For simplicity, only data for grains with basal poles inclined 30-45° from the compression axis is shown, because it is representative of the trends observed for all basal pole orientations. As shown, the as-molded and equilibrated states show IGMA peaks around $\langle 0001 \rangle$ and $\langle 10\bar{1}0 \rangle$ with some $\langle uvt0 \rangle$ spread. In contrast, the solution-treated material only shows an intense peak near $\langle 0001 \rangle$. This indicates the presence of substantial populations of both basal and prismatic GNDs in the equilibrated and as-molded material, but only a strong population of prismatic GNDs in the solution treated material. The LAGBs associated with

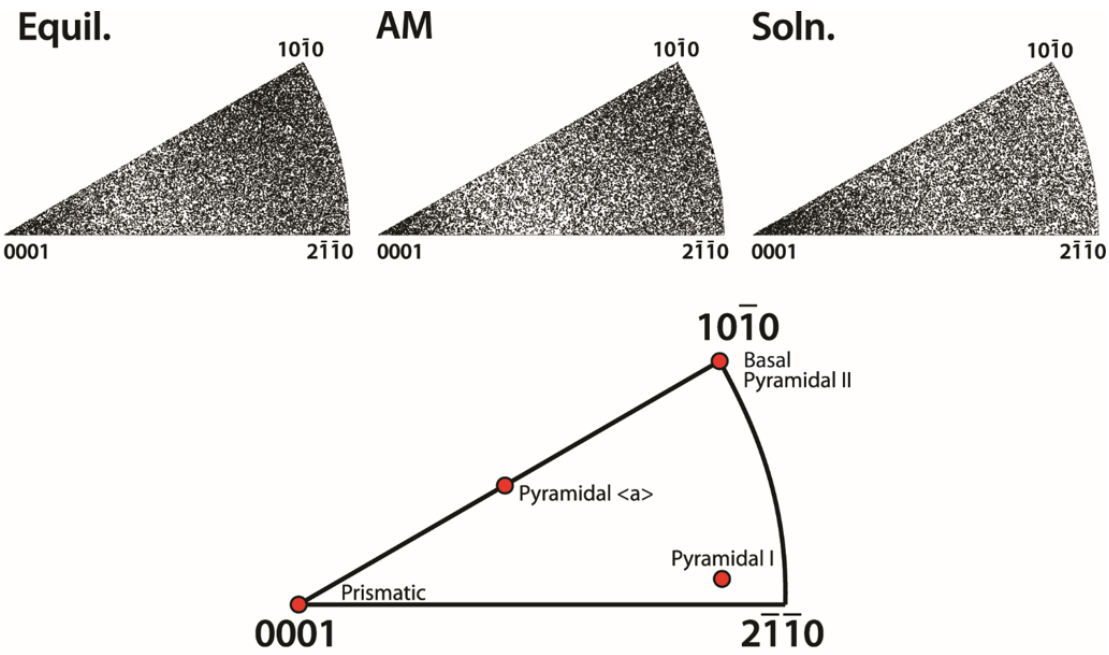

Figure 5.7: IGMA analysis of grains with basal poles inclined by 30-45° to the compression axis material strained to 0.1 in each of the microstructural starting conditions. Taylor axes reference diagram is adapted from References [66, 93]. Reprinted with permission from Reference [96].

coarse particles analyzed in the previous section are also consistent with this trend.

5.1.1 Summary of solute effects on texture evolution

It has been demonstrated by Stanford et al. and later studies that calcium additions can modify texture in the same manner as RE elements [61, 134–136], so the RE texture mechanism should be considered as a possible explanation of the observed texture evolution in the present material. The rare earth mechanism is discussed in detail in Chapter 1, but will be summarized here. Generally, RE solute content has been demonstrated to result in weakened but conventional Mg alloy textures during deformation [83, 86]. This effect is at least partially a result of the alteration of slip system activity [65, 66] and may also be related to the influence of RE additions on stacking fault energy [137]. Upon recrystallization in these alloys, a new RE texture component is formed. Recrystallized grains in the new texture component nucleate from shear bands formed during deformation, which are more diffuse and less severe than shear bands observed in conventional alloys [7, 69, 79]. Additionally, it has been observed that rare earth elements segregate to grain boundaries, limiting boundary mobility [138]. This reduced boundary mobility is thought to restrict the recrystallized grain size

and may also alter which recrystallization mechanisms are active [66]. Each of these rare earth effects is examined in additional detail below.

In the present work, there is no evidence of a new texture component in the deformation or recrystallization textures for any of the examined microstructural conditions. Both the deformation and recrystallization textures are conventional but weak basal textures. The rare earth texture component has been linked to the presence of special shear bands; as no shear bands were observed during deformation in this material, it is not surprising that no new texture component was observed. This raises the question of why shear bands do not form during compression of the AXJ810 material studied here. It has been widely reported that shear bands nucleate in association with twins, and that the presence of RE solute enhances double and compression twinning [6, 139]. However, relatively few twins of any variety were observed in the deformed microstructures, consistent with the absence of shear banding. While the reason for the relative scarcity of twinning is uncertain, it is possible that this is simply an effect of the relatively fine grain size in the starting thixomolded microstructures, because a decreasing grain size has been reported to increase the difficulty of twinning more strongly than it increases the difficulty of slip activity [14, 25, 26, 28, 29].

Even in the absence of characteristic shear banding, other solute effects such as alteration of slip system activity may be operative. It has been sug-

gested that the RE solute effect is similar to that described by Urakami and Fine [140] and further investigated by Sato and Meishi [141], where solute simultaneously strengthens against basal slip and softens prismatic slip. IGMA of conventionally-textured dilute Mg alloys by Hadorn *et al.*[66] showed little to no IGMA intensity near $\langle 0001 \rangle$, which would indicate the operation of prismatic slip systems. In that study, increased RE solute content shifted intensity to being present only near $\langle 0001 \rangle$ [66]. As described in Chapter 4, a strong population of prismatic dislocations allows the formation of multiple, nonparallel dislocation walls which may efficiently form recrystallization nuclei.

In this work, all three microstructural conditions developed IGMA intensity near $\langle 0001 \rangle$, similar to the RE-textured material studied by Hadorn *et al.*. This suggests that the presence of alkaline earth alloying elements is altering the slip activity in all three microstructural states, though not necessarily to an equal extent in each case. However, both of the particle-rich microstructures in this study also contain IGMA intensity near $\langle 10\bar{1}0 \rangle$ indicating a population of basal GNDs. The presence of multiple populations of GNDs in grains of similar orientation was not observed by Hadorn *et al.* and may further enhance the rotational freedom of subgrains during recovery as basal and prismatic walls can function simultaneously to promote polygonization. However, the RE-like alteration of slip system activity alone does not, at least in this alloy, appear to be sufficient

for texture modification because the solution treated material ultimately developed the strongest texture.

The final reported solute effect in RE alloys is solute segregation to grain boundaries [66, 138], which alters their local structure and therefore their mobility and propensity for slip transmission. While it is possible or even likely that solute, particularly Ca and Sr, is segregating to boundaries, further high resolution microscopy would be required to examine this possibility.

5.1.2 Summary of intermetallic particle effects on texture evolution

The data presented in Figure 5.4 demonstrates that the as-molded condition develops the greatest GOS, suggesting that the combined presence of many 1-2μm hard intermetallic particles promotes increased grain orientation spread, an effect which is further enhanced in the presence of increased solute content. Increased GOS in the microstructure will tend to cause a more diffuse deformation texture. The modification of texture by intermetallic particles has been reported in magnesium alloys by Li *et al.* [31]. In this case, it was asserted that the β phase precipitates may have impeded the activity of extension twinning, changing the deformation texture. While it is possible that similar effects help

to explain the relative scarcity of deformation twinning observed in this work, it is unlikely because the intermetallic compounds are generally present as coarse particles, not fine precipitates.

The GROD data presented in Figure 5.5 offers a more plausible mechanism for the particle-induced increase in GOS. The individual particles present on the grain boundaries promote locally inhomogeneous deformation, and this results in the formation of LAGBs. These boundaries increase GOS and promote a more diffuse deformation texture. However, as they are primarily composed of basal dislocations, they do not promote rapid nucleus formation, requiring a more complex deformation structure to develop prior to the onset of dynamic recrystallization. However, once a nucleus successfully forms, they are favorable sites for recrystallization at larger strains due to the high angle boundary and large stored energy.

The particle-induced texture weakening observed in this work is even stronger than that reported by Li *et al.*. Similarly, the texture weakening effect is present at much smaller strains than in the Mg-Zn binary alloys discussed in Chapter 3. In classic PSN literature, intermetallic particles are reported to create a deformation zone that is similar in size to the characteristic dimension of the particle with maximum misorientations on the order of tens of degrees [121, 142]. With the more homogeneous distribution of intermetallic particles

at grain boundaries, larger total fractions of the material are found in the particle deformation zones, resulting in weaker deformation textures.

Other researchers have additionally suggested that PSN is active in Mg alloys (e.g. [65, 87]). PSN is typically defined as recrystallization at or near the surface of coarse ($>1\mu$m diameter) particles caused by the enhanced deformation required to maintain compatibility near the particle. In many metal-intermetallic systems, PSN can result in either texture weakening or the formation of a new texture component depending on the material system and processing [94, 97]. The present work agrees well with results of these other studies in magnesium alloys, where PSN has been reported to generally decrease texture intensity but not to produce new texture components. As shown by Figures 5.3 and 5.4, dynamic recrystallization begins between 0.1 and 0.3 strain for the microstructures with large fractions of coarse particles, but it is not accompanied by significant texture strengthening.

Additionally, Figure 5.4 clearly shows that PSN plays an important role in altering the recrystallization kinetics, promoting more rapid nucleation during dynamic recrystallization thereby reducing the initial recrystallized grain size (Table 5.2). As shown in Table 5.2, this effect is particularly strong in the equilibrated material, which contains the largest particles. Larger particles would tend localize deformation more strongly, resulting in a smaller nucleus size [89].

This activity of PSN in AXJ810 is in contrast to the results presented in Chapters 3 and 4, where the highly inhomogeneous distribution of coarse intermetallic particles resulted in a negligible impact of PDZ formation on texture evolution at small and intermediate strains and PSN on recrystallization kinetics. However, with the highly homogeneous distribution of intermetallic particles in AXJ810 produced by thixomolding PSN is active and the presence of particles does modify the deformation texture. This indicates that the existing body of PSN literature has substantial relevance, even for particles located on grain boundaries instead of embedded within grains.

In addition to PSN, the presence of a larger volume fraction of particles may pin grain boundaries via Zener drag. This reduction of grain boundary mobility by particle pinning and possibly aided by solute segregation may also alter the activity of other recrystallization mechanisms. As discussed in Chapter 1, necklace recrystallization is one of the most frequently reported recrystallization mechanisms in Mg alloys. In this mechanism, nucleation occurs at pre-existing grain boundaries via grain boundary serration and rotation of the resulting subgrains. It has been suggested that this mechanism is inhibited in RE-containing alloys due to reduced boundary mobility caused by solute segregation [66]. In the current work, Ca may play a similar role, and it may be further aided by the intermetallic particles in limiting boundary mobility. No

grain boundary serration was observed in any of the deformed and partially recrystallized microstructures, suggesting that this alloy also sees inhibition of this recrystallization mechanism. Additionally, the internal LAGBs formed are basal, and cannot efficiently subdivide the grain interior to facilitate nucleation. The delay of necklace recrystallization may enhance the role played by alternative nucleation mechanisms (including PSN). This is particularly true for the solution treated material, where the very small number of intermetallic particles would normally prevent PSN from playing any significant role.

5.2 Static recrystallization behavior of TTMP sheet

Additionally, the recrystallization behavior of the as-received thermomechancially processed sheet described in Section 2.2.1 was examined as a function of temperature to verify that these effects also occur at under commercial processing conditions. A secondary electron image and IPF map of the as-TTMP microstructure are shown in Figure 5.8. After the TTMP process, the microstructure is partially recrystallized and additional β has precipitated. The as-TTMP texture possesses a conventionally rolling texture, with a strong split basal peak and a large amount of spread in the basal pole figure toward the TD. This large TD spread is common for microstructures containing relatively large

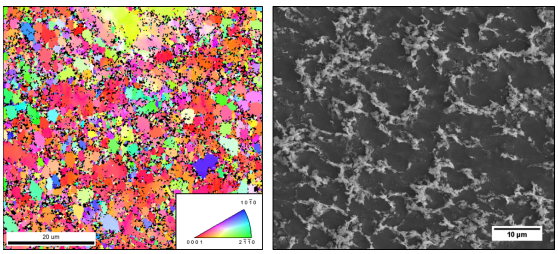

Figure 5.8: Secondary electron image and IPF map referenced to the ND of the as-TTMP AXJ810 microstructure. The sheet normal is out of the plane of the page. Reprinted with permission from Reference [95].

fractions of coarse intermetallic particles, as demonstrated in Chapter 3.

Heat treatments of 5 minute and 24 hour duration were conducted at 300°C and 450°C on the as-TTMP material to investigate the microstructural and texture evolution during recrystallization and grain growth. The resulting microstructures are shown in Figure 5.10. Post-TTMP heat treatment at 300°C results in greater than 80% recrystallized after five minutes of heat treatment, which increases to more than 90% recrystallization after 24 hours. Minimal dissolution of the β phase is observed at the shorter annealing duration. The recrystallized grain size observed after 5 minutes is 4.9μm, with only a slight increase to 5.1μm observed after 24 hours. Substantial texture weakening is observed upon recrystallization, with the peak intensity of the basal pole figure dropping to 3.1 multiples of random after the five minute heat treatment. A slight increase to a peak intensity of 3.3 MRD is observed after 24 hours.

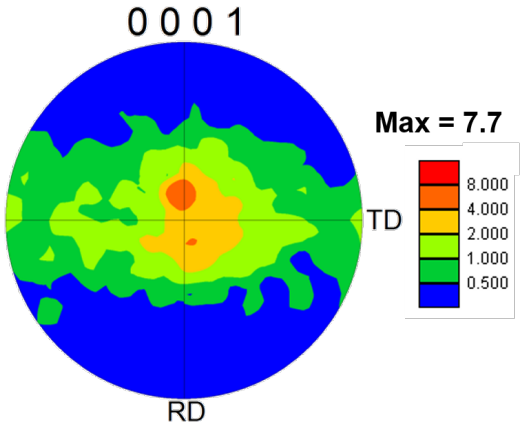

Figure 5.9: Basal pole figure for the as-TTMP AXJ810 sheet. Reprinted with permission from Reference [95].

Heat treatment at 450°C also produces nearly complete recrystallization within the first five minutes. However, as this temperature is above the β solvus, dissolution of that phase was observed and was nearly complete within the first five minutes at temperature (Figure 5.10). The thermally stable Laves phase remained unchanged after heat treatment. The peak texture intensity after 5 minutes is 3.1 multiples of random distribution (MRD), the same value observed after 5 minutes at 300°C. After 24 hours at 450°C, the basal peak intensity had increased to 4.3 MRD.

Severe grain growth was not observed at either heat treatment temperature in this study, even at 450°C, i.e. approximately 95% of the melting point of the alloy. Additionally, only small differences in the extent of grain growth were

Table 5.3: Average recrystallized grain size in TTMP and heat treated AXJ810.

Temperature	d after 5 min	d after 24h
300°C	4.9μm	5.1μm
450°C	4.6μm	7.1μm

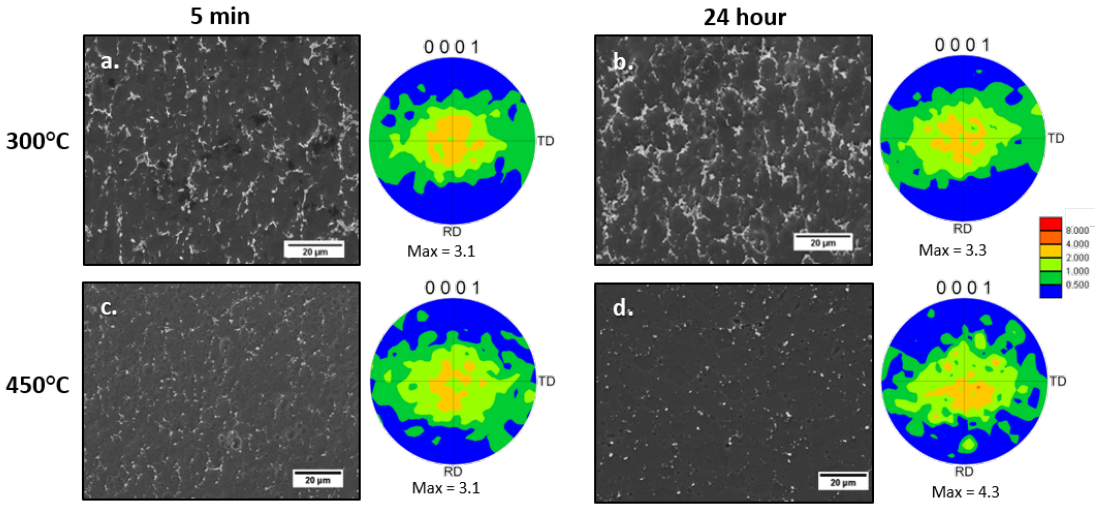

Figure 5.10: Secondary electron micrographs and EBSD (0001) pole figures for TTMP AXJ810 subjected to 5 minute (a, c) and 24 hour (b, d) heat treatments at 300°C(a, b) and 450°C(c, d).

observed between the two heat treatment temperatures despite the complete dissolution of the β phase at 450°C. The thermally stable Laves phase alone is effective at pinning the grain boundaries and stabilizing the fine grain size.

Substantial texture randomization in terms of reduction in the peak intensity of the basal pole figure occurs at both 300°C and 450°C, while only minimal texture weakening during static recrystallization is typical for Mg alloys. As described in Section 5.1, particle stimulated nucleation may play a role in the texture weakening. Grain growth after the completion of recrystallization results in texture strengthening at both temperatures; however, the texture strengthening is substantially more severe at 450°C above the β solvus. Even the relatively small increase in grain diameter from 4.6μm to 7.1μm is accompanied by substantial texture strengthening.

5.3 Recrystallization behavior in the absence of pinning particles

Due to the nature of the thixomolding process, the thixomolded material contains a volume fraction of approximately 10% of 50μm diameter "externally solidified grains" which were either not melted or solidified outside the mold.

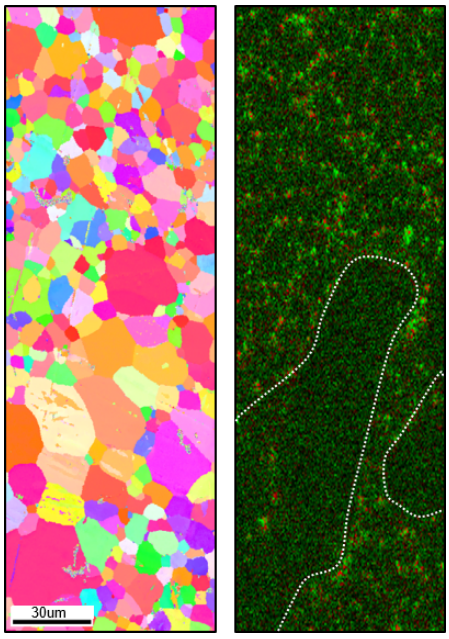

Figure 5.11: Inverse pole figure map (left) and Al/Ca EDS map (right) of material heat treated at 450°C for 24 hours, with the previous location of the externally solidified grain outlined in white on the EDS map. Reprinted with permission from Reference [95].

The presence of these externally solidified grains provides an opportunity to simultaneously examine the deformation and recrystallization behavior in regions with and without the influence of the thermally stable Laves phase present to provide a Zener pinning force. An inverse pole figure and an Al/Ca EDS map of the corresponding region in material that was post-TTMP heat treated for 24 hours at 450°C is shown in Figure 5.11. In the EDS map, green points denote Al-rich regions, while red points denote Ca-rich regions. In the lower portion of a map, a region largely free of coarse intermetallic particles is observed, corresponding to the previous location of an externally solidified grain. As shown in the figure, the previous externally solidified grain has both a coarser grain size and a greater fraction of basal grains than the particle-rich matrix.

Grain size and texture analysis was conducted independently on intermetallic-containing and intermetallic free regions for a combined total of approximately 10,000 grains. Note that the number of grains analyzed from intermetallic-free regions is substantially smaller than that of the intermetallic-containing regions due to the lower volume fraction present in the material. After 5 minute heat treatments at 300°C and 450°C no significant difference in grain size was observed between the intermetallic-containing and intermetallic-free regions. However, substantial differences were observed in the grain sizes after 24 hour heat treatments, which are presented in Table 5.4.

Table 5.4: Average recrystallized grain size in TTMP and heat treated AXJ810 in particle-free and particle-rich regions.

Temperature	d in particle-rich regions	d in particle-free regions
300°C	4.6μm	13.8μm
450°C	7.0μm	15.4μm

Basal pole figures, shown in Figure 5.12, were calculated independently for the intermetallic-free and intermetallic-containing regions of TTMP AXJ810 heat treated at 450°C for 24h. These regions were partitioned using a grain size criterion and were visually correlated with EDS maps to ensure accuracy; extraneous grains were manually removed. The texture calculated from the intermetallic-containing regions has a substantially lower peak intensity and retains substantially more TD spread than that of the intermetallic-free region.

Comparison of regions with and without intermetallic particles demonstrates that these particles play a critical role in texture randomization and stabilization during deformation and recrystallization. Section 5.1 suggests that the lack of intermetallic particles likely leads to locally stronger textures during deformation. Upon recrystallization, some randomization occurs with or without intermetallic particles. However, without the presence of the thermally-stable Laves

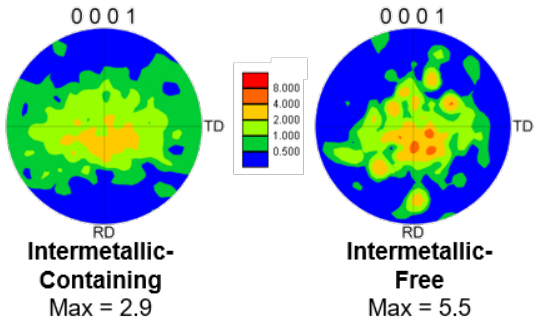

Figure 5.12: Basal pole figures of the intermetallic-free and intermetallic-containing regions in a sample heat treated at 450°C for 24 hours. Reprinted with permission from Reference [95].

phase during heat treatment, the basal texture subsequently strengthens again during grain growth.

5.4 Summary of AXJ810 behavior

In summary, the effects of coarse intermetallic particles during deformation and recrystallization discussed in Chapter 3 and 4, respectively, are also observed during both laboratory and commercial processing. At the laboratory scale, three AXJ810 microstructures, sampling the spectrum of increasing intermetallic particle fraction and decreased solute content were tested in warm uniaxial compression. The weakest basal texture was developed at intermediate levels of both intermetallic particles and solute content. Microstructures

with increased solute content were observed via IGMA measurements to develop greater populations of prismatic GNDs, indicating that the change in solute content altered the relative activity of the available deformation modes.

The starting microstructures containing greater fractions of coarse intermetallic particles developed weaker basal peaks during deformation to at least intermediate strains, in agreement with Chapter 3. However, due to the geometry of the uniaxial compression deformation state, changes in the amount of TD spread were not observed. Under the plane strain compression conditions in the as-TTMP material, substantial TD spread and a split basal peak was present, similar to the rolled Mg-Zn alloys. The peak intensity of the basal pole figure was slightly lower for the TTMP AXJ810 material, likely due to the higher rolling temperature which further altered the balance of deformation modes and enabled dynamic recrystallization. The alteration of recrystallization kinetics by particle stimulated nucleation is in contrast to the results discussed in Chapter 4. This difference may be attributed to the higher deformation temperature enabling dynamic recrystallization, as well as the substantially more homogeneous distribution of intermetallic particles which results from the thixomolding process.

During recrystallization in the TTMP AXJ810, texture strengthening and reduction in TD spread was observed during recrystallization above the β solvus.

These conditions are comparable to the recrystallization of the Mg-9Zn alloy at 300°C, where many of the fine pinning particles have dissolved, where similar texture strengthening is observed. However, the presence of the Laves phase in AXJ810 prevents substantial grain growth and inhibits texture strengthening. The importance of the Laves phase pinning particles for inhibiting grain growth and the associated texture strengthening is particularly evident when comparing the recrystallization behavior of the fine-grained matrix and the externally solidified grains. Under identical deformation and recrystallization conditions, regions rich in fine particles develop a grain size that is finer by a factor of two and substantially weaker basal texture.

Chapter 6

Prediction of formability via polycrystal plasticity simulation

The dependence of ductility and formability on grain size [14, 17, 48, 49] and texture [7, 42, 47, 50–53] is widely reported. However, due to the interdependence of texture and grain size on alloying and processing, it is challenging to isolate these factors experimentally. Polycrystal plasticity simulations offer the opportunity to examine formability as a function of texture characteristics or propensity for a particular deformation mode while guaranteeing all other material and deformation parameters remain constant.

A number of researchers have utilized polycrystal plasticity tools to examine

formability. Forming limit diagrams have been computed using several different polycrystal frameworks in cubic metals (e.g. [45, 143, 144]) and in hcp alloys, including Mg [145–147]. In particular, Wang *et al.* [145] found significantly improved formability with decreasing basal peak strength by simulating forming tests on the same texture in different orientations. Additionally, Neil *et al.* [147] compared the formability of magnesium having a random texture with material having an experimentally measured rolling texture, again highlighting the importance of weak intensity of the basal peak for enhancement of formability. Agnew *et al.* [8, 16] have examined possible sources of plastic anisotropy of magnesium alloy sheet, concluding that the anisotropy is largely attributable to the texture.

In this work, the viscoplastic self-consistent (VPSC) framework developed by Lebensohn and Tomé [109, 110] is used to simulate uniaxial tension tests at room temperature as described in Section 2.4, and the effect of various textures and effective grain sizes are considered. To examine the effect of varied texture characteristics, the single crystal hardening parameters are held constant and the formability of different synthetic textures is evaluated. The effect of grain size on deformation behavior is then considered for different starting textures by altering the critical resolved shear stress for twinning to simulate a varied grain size. In both sections, the changes in stress-strain response, relative slip activity,

r-values, and $\bar{r}$evolution with strain are reported. For all examined textures and effective grain sizes, increased reliance on prismatic slip corresponded to higher r-values, suggesting poorer forming behavior.

6.1 Parameterization to fine-grained AZ61L

Fine-grained thixomolded and thermomechanically processed (TTMP) AZ61L, which demonstrates desirable mechanical behavior in room temperature tensile tests [42], was selected to parameterize the VPSC model for evaluating formability. Basal, prismatic, and pyramidal II slip as well as tensile twinning deformation modes were allowed, and hardening parameters were selected to replicate the in-plane plastic anisotropy of the sheet. The hardening parameters reported in Table 6.1 produced the stress-strain behavior shown in Figure 6.1. As shown, the selected hardening parameters result in an excellent match between the simulated and experimental stress-strain curves along the rolling and transverse directions.

As further verification that the balance of active deformation mechanisms is adequately captured by the parameterized model, the experimental and simulated texture evolution after 10% tensile strain tested along the (RD) and (TD) is compared in Figure 6.2. During uniaxial tension along the RD, in both the sim-

Table 6.1: Voce hardening parameters utilized in all subsequent VPSC simulations.

		τ_0 (MPa)	τ_1 (MPa)	θ_0	θ_1
basal	$\{0001\}\langle 2\bar{1}\bar{1}0\rangle$	63	20	190	100
prismatic	$\{10\bar{1}0\}\langle 2\bar{1}\bar{1}0\rangle$	165	20	300	90
pyramidal	$\{11\bar{2}2\}\langle\bar{1}\bar{1}23\rangle$	230	20	230	90
tensile twin	$\{10\bar{1}2\}\langle\bar{1}011\rangle$	110	0	100	30

ulation and experiment the basal poles spread toward the sheet TD, while the prismatic poles align along the RD. Conversely, during tension along the sheet TD, the basal poles align with the RD while the prismatic poles preferentially align with the loading direction. In both cases, the VPSC model over-predicts texture evolution; this effect is common and has been discussed elsewhere in the literature [115, 116, 118, 119, 148]. Overall, the good qualitative match in texture evolution suggests that the model is successfully capturing the active deformation mechanisms for this material.

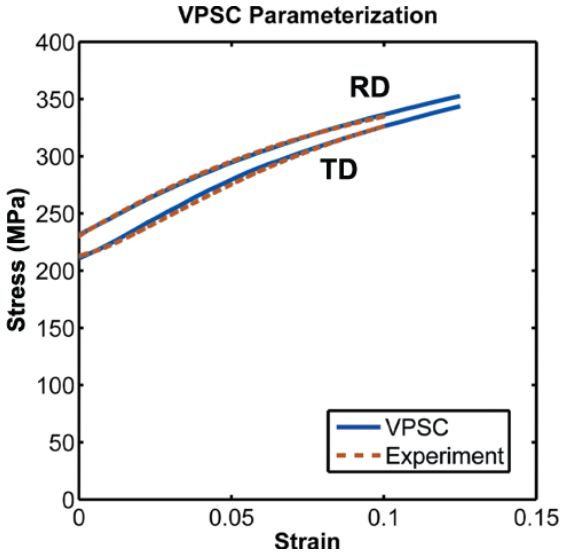

Figure 6.1: Experimental and VPSC-fit stress strain curves for fine-grained AZ61L. Figure reprinted with permission from [113].

6.2 Varied texture characteristics

Synthetic textures were generated for analysis using DREAM.3D Version 5.2 and the Stats Generator auxiliary tool [149]. First, Stats Generator was used to define the target texture and create a starting DREAM.3D data file. A DREAM.3D pipeline that uses the target statistics output by Stats Generator is presented in Table 6.2. Note that this pipeline generates complete three-dimensional microstructures, including information such as grain neighbors, shapes, and size distribution, appropriate for a more rigorous (but computationally costly) crystal plasticity finite element modeling approach. Only the weighted grain orien-

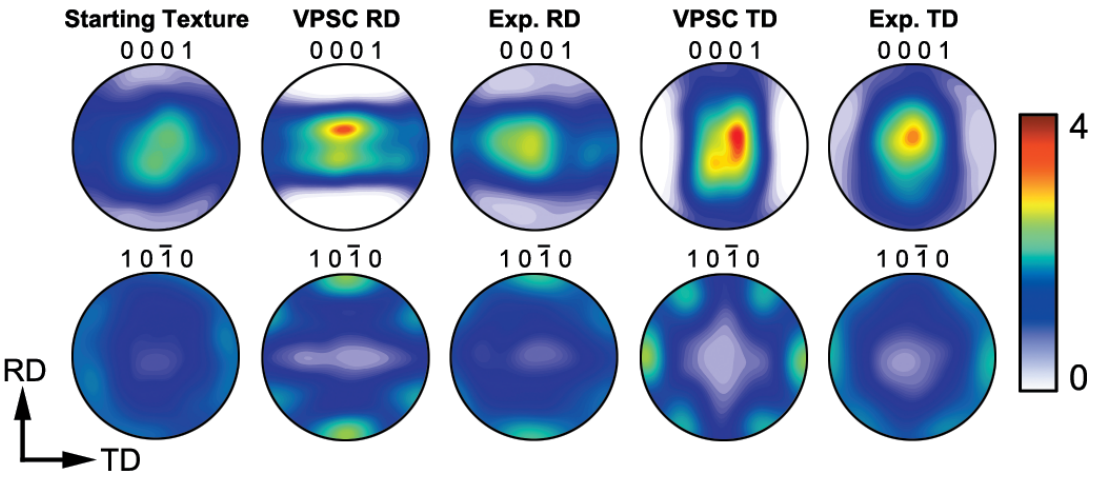

Figure 6.2: Experimental and VPSC-predicted texture evolution for fine-grained AZ61L. Reprinted with permission from Reference [113].

tations were used for the VPSC simulation in this work.

The synthetic volume created was a cube 150 voxels on edge, with a voxel spacing of 0.5μm in all directions. This resulted in volumes containing more than 30,000 grains. The MTEX texture analysis toolbox for Matlab [106] was used to import the DREAM.3D-output text files as orientation density functions (ODFs) and output VPSC texture files with 10,000 orientations. The formability of these synthetic textures was tested as described in Section 2.4.1 using the Voce parameters discussed in Section 6.1.

The texture characteristics selected for examination are those commonly observed in magnesium processing textures. First, the effect of basal peak strength,

which is already known to influence formability, is isolated. Second, the effect of planar anisotropy (i.e. symmetry of the basal peak) is examined. Strong asymmetry or splitting of the basal peak is often observed as the result of alloying [19] or the presence of intermetallic particles [31]. Finally, the symmetry of the prismatic pole figure is considered. A transition from radial symmetry to sixfold symmetry of the prismatic pole figure is frequently observed during deformation processing [42] or during grain growth[73].

6.2.1 Effect of basal peak strength

The effect of varied basal peak intensity on formability was isolated for the textures shown in Figure 6.4, with the differences in deformation behavior shown in Figure 6.3. The stress-strain curves show only slight differences in RD versus TD loading due to the symmetry of the basal peak. The texture evolution during uniaxial tension to 20% elongation in Figure 6.4 as the starting textures, deformed textures, and pole figure difference plots. In all three cases, the peak intensity of the basal pole figure slightly decreased, while the maximum value of the prismatic pole figure increased. The pole figure difference plots show that the c-axis poles spread toward the TD during deformation and the basal peak starts to split toward the RD. The TD spreading of the basal peak

is more pronounced for weaker basal textures, while the strengthening of the sixfold symmetry of the prismatic pole figure is greatest for the strongest basal texture.

The observed texture evolution is a direct result of the deformation mode activity, shown as insets in Figure 6.3. For all three basal textures, deformation was dominated by a combination of basal and prismatic slip, with some activation of pyramidal slip. The weaker basal textures also allowed for some tensile twinning during deformation, with twinning accounting for approximately 7% of the strain in the weakest basal texture at yield. The primary effect of decreasing basal peak intensity is an increasing dominance of basal slip. Grains with perfectly basal orientations have a Schmid factor of zero for basal slip, so the harder prismatic slip mode must accommodate more of the deformation. This reliance on harder slip modes also accounts for the difference in macroscopic yield strength.

These variations in deformation mode activity result in strong variations in the predicted r-values and their evolution with strain, also shown in Figure 6.3. The r-values increased with basal peak strength and remained approximately constant at all orientations within the sheet plane. Stronger basal textures also resulted in greater increases in $\bar{r}$with increased strain.

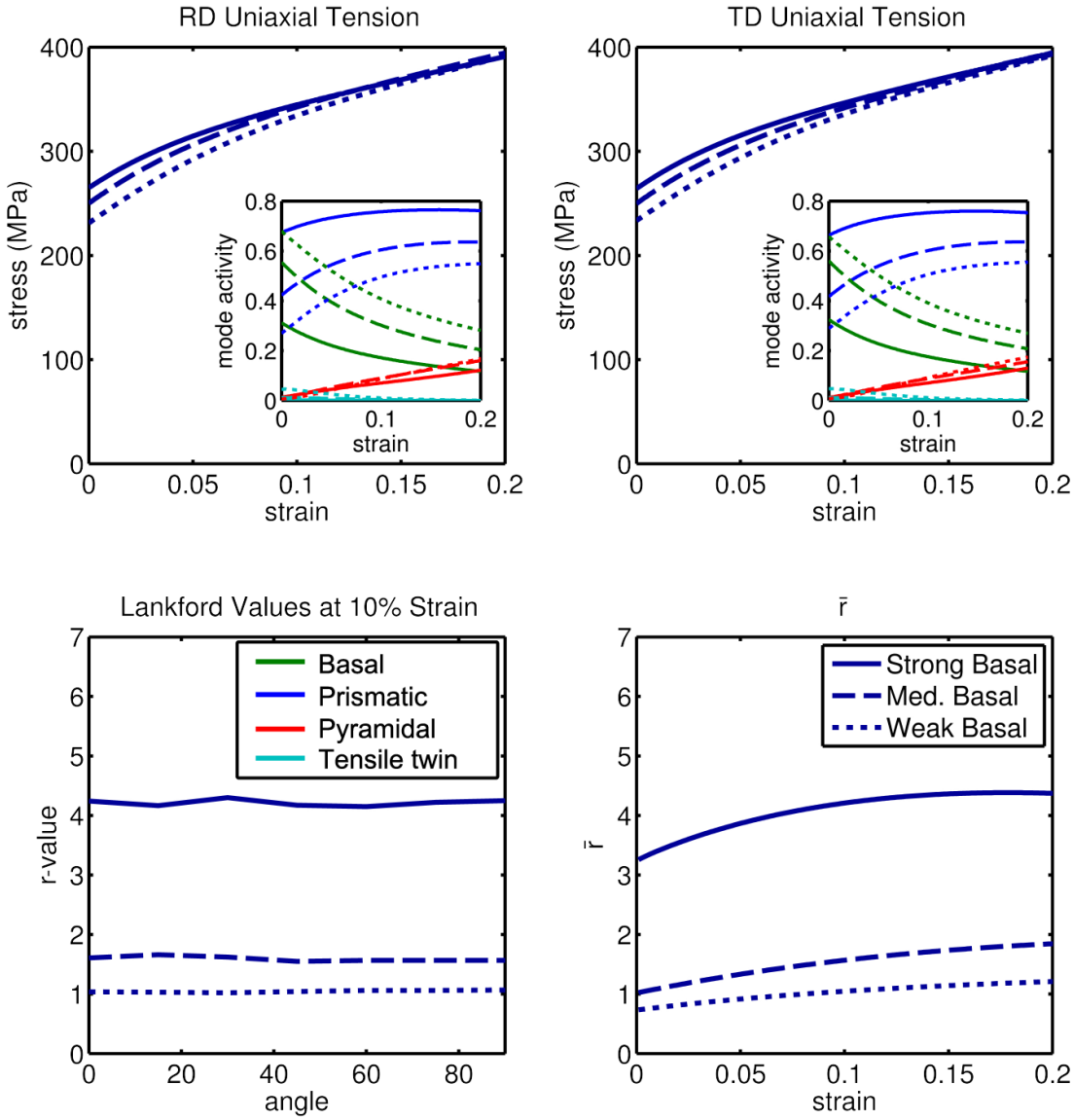

Figure 6.3: Effect of basal peak strength on plastic deformation. Reprinted with permission from Reference [113].

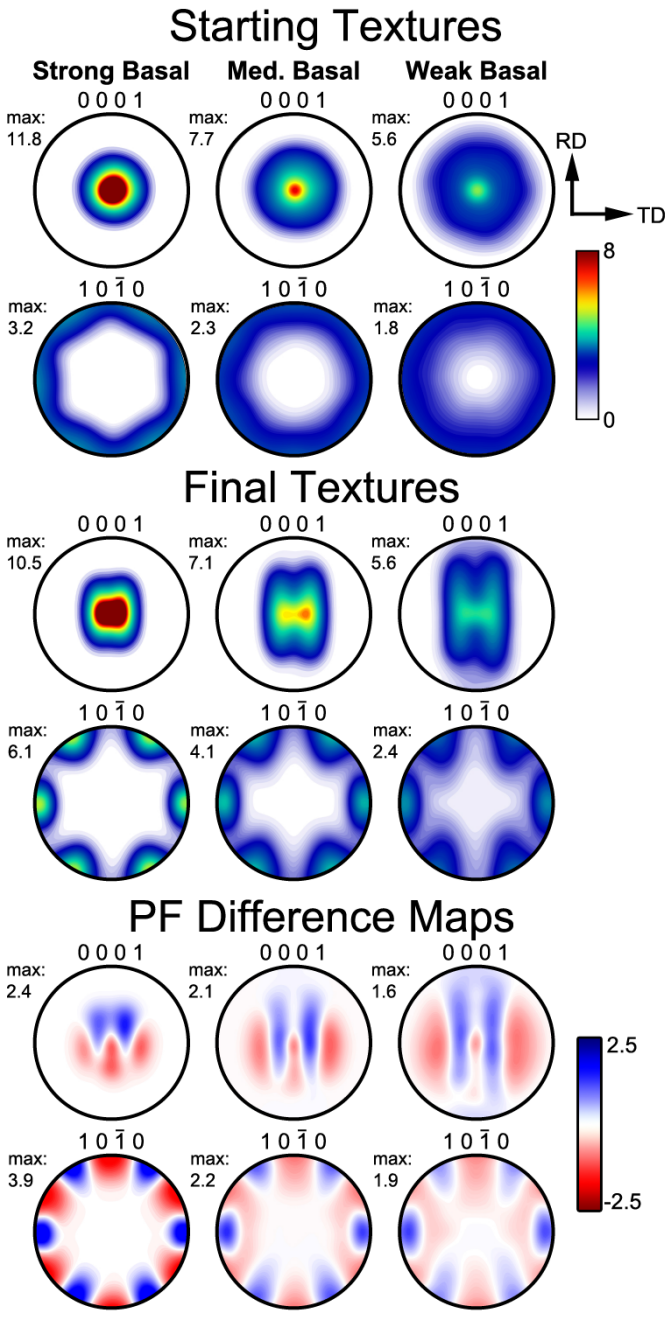

Figure 6.4: Effect of basal peak strength on texture evolution. Reprinted with permission from Reference [113].

6.2.2 Effect of basal peak asymmetry

The effect of basal peak asymmetry on deformation behavior is shown in Figure 6.6. The textures shown in Figure 6.5 vary the amount of spread in the distribution of basal pole tilt toward the TD while maintaining a nearly constant basal peak intensity, a variation which has not been achieved experimentally. This texture variation results in minimal changes in stress-strain behavior along the rolling direction, with the small variations due to increased prismatic and pyramidal slip activity with increasing basal peak asymmetry. No twinning is observed during RD tension.

The basal peak asymmetry results in larger changes in loading along the TD. Increasing basal peak asymmetry, i.e. greater TD spread of the basal peak, results in increased activation of twinning and decreased reliance on prismatic slip at yield. This results in a slight decrease in macroscopic yield strength.

However, the varied symmetry of the basal peak at a constant peak intensity has only a small effect on the r-values in comparison to varied peak strength. For all three conditions, the r-alues fell between 1.0 and 2.0 for all in-plane orientations, with increased asymmetry resulting in slightly higher values of $\bar{r}$.

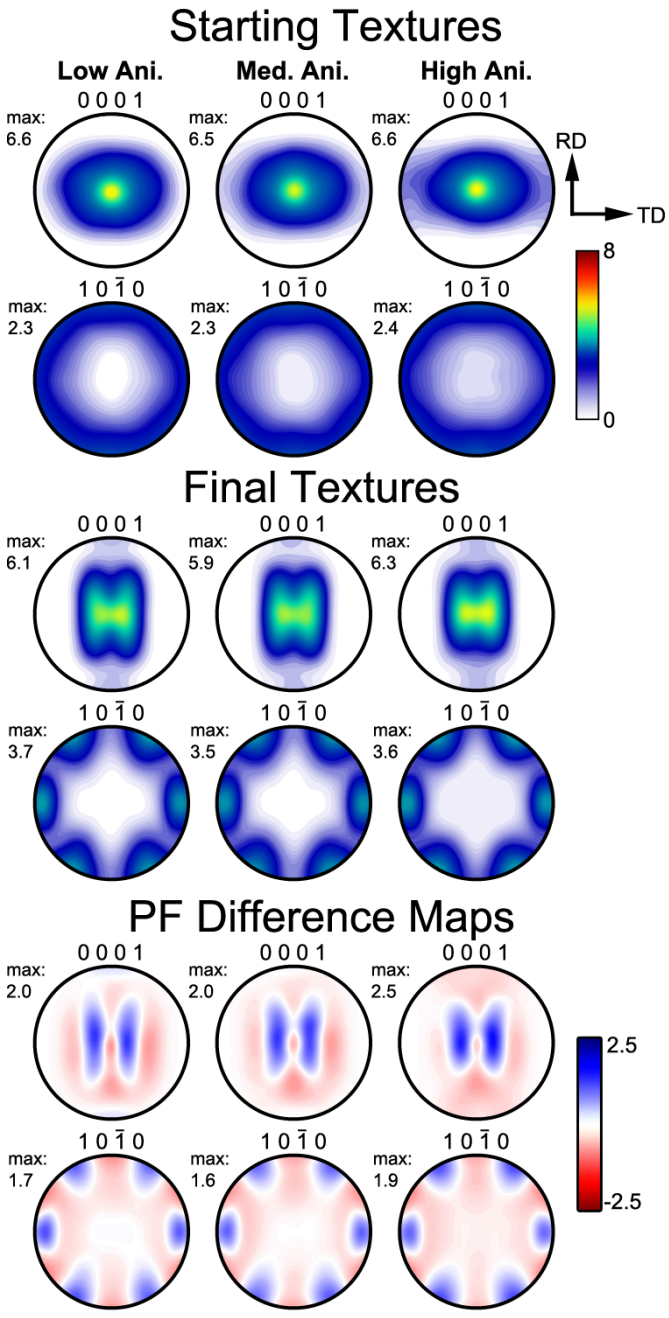

Figure 6.5: Effect of basal peak symmetry on plastic deformation. Reprinted with permission from Reference [113].

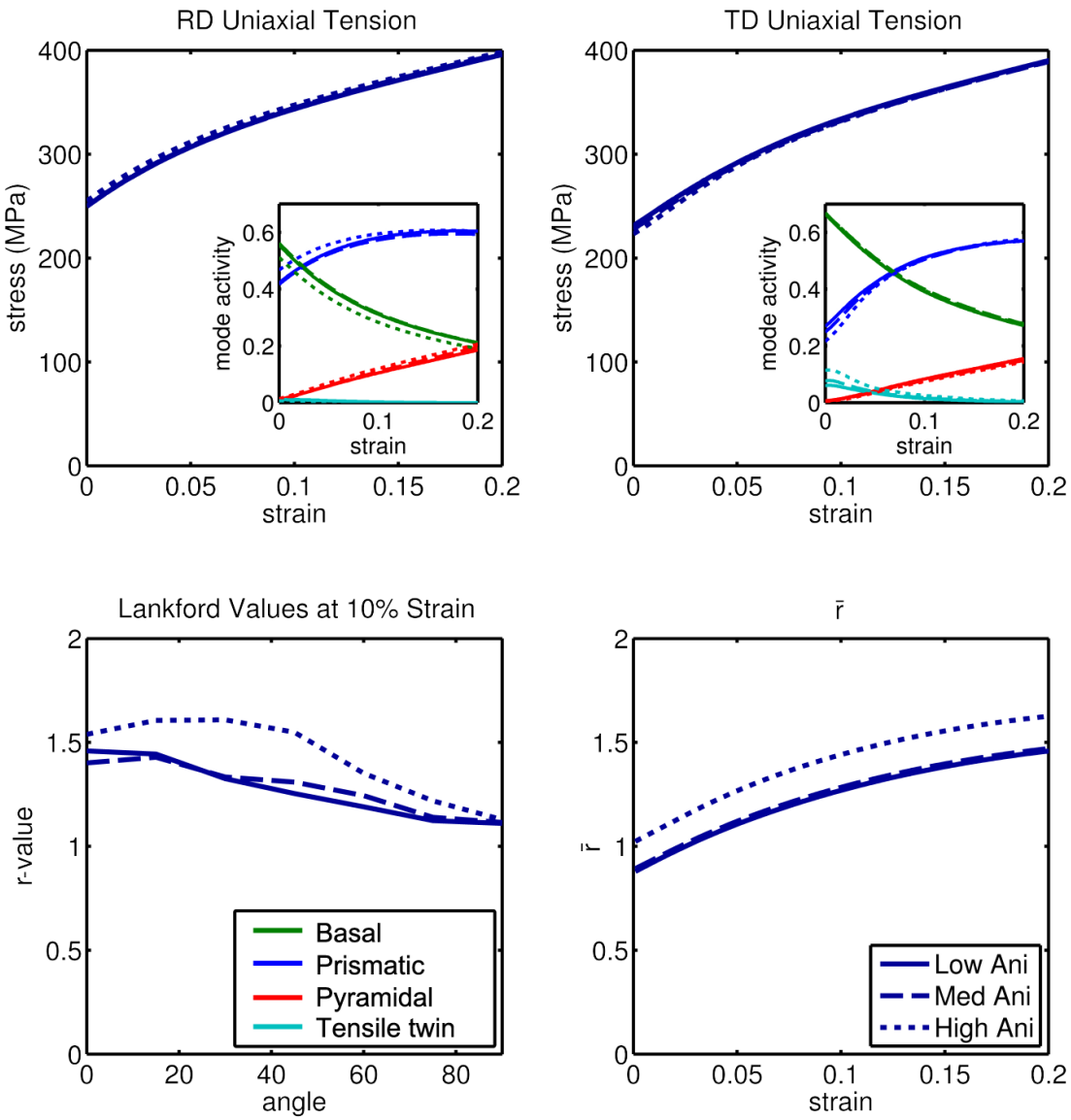

Figure 6.6: Effect of basal peak symmetry on texture evolution. Reprinted with permission from Reference [113].

6.2.3 Effect of prismatic plane distribution symmetry

Finally, the effect of sixfold symmetry versus radial symmetry in the prismatic pole figure, as shown in Figure 6.7 on forming behavior is considered. Minimal differences in deformation behavior are observed, as shown in Figure 6.8. The stress-strain behavior is nearly identical in both the RD and TD configurations, as are the slip activity and r-values. The texture evolution is similar to that of the strong basal texture described in Section 6.2.1, with weakening of the basal peak and strengthening of the sixfold symmetry of the basal pole figure.

6.2.4 Summary of texture and formability

For all of the examined texture characteristics, the predicted formability correlated strongly with the activity of prismatic slip. As discussed by Koike *et al.* [15], in the context of a tensile test of a sheet with a basal texture, geometric argument demonstrate that width strains are primarily accommodated by prismatic slip while thickness strains are accommodated by pyramidal and to a lesser extent by basal slip. As such, high r-values—and the associated poor formability—result from large amounts of prismatic slip relative to the activity of other deformation modes. The trade off between prismatic slip and basal slip is almost entirely determined by the basal pole tilt (angle between the grain c-

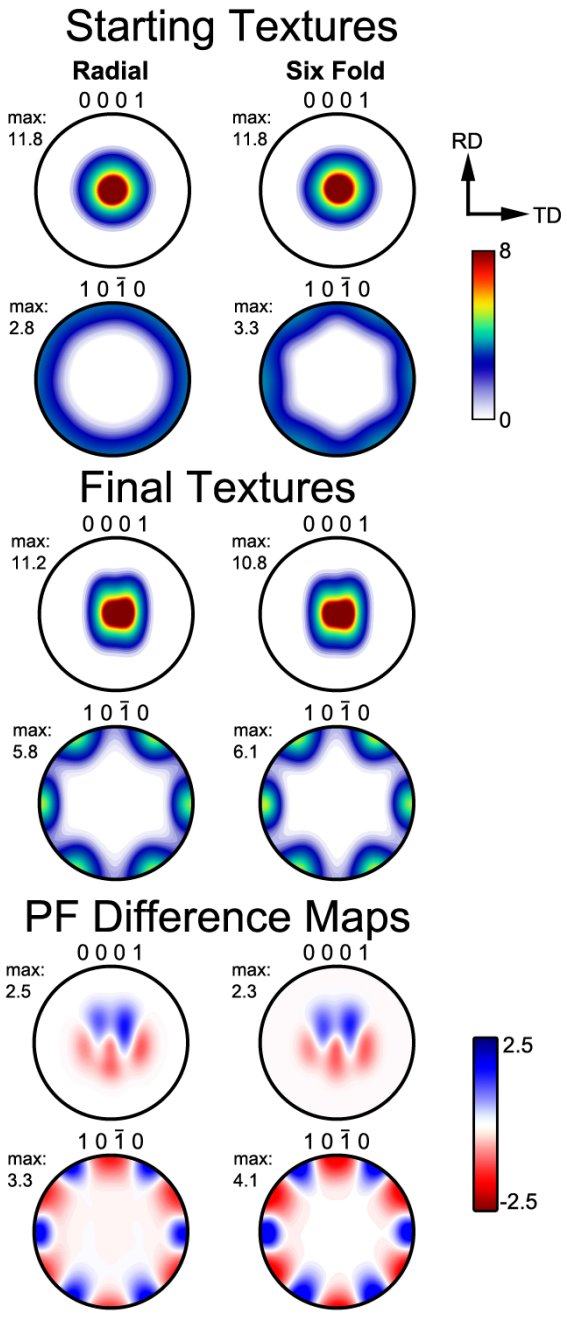

Figure 6.7: Effect of prismatic plane distribution on texture evolution. Reprinted with permission from Reference [113].

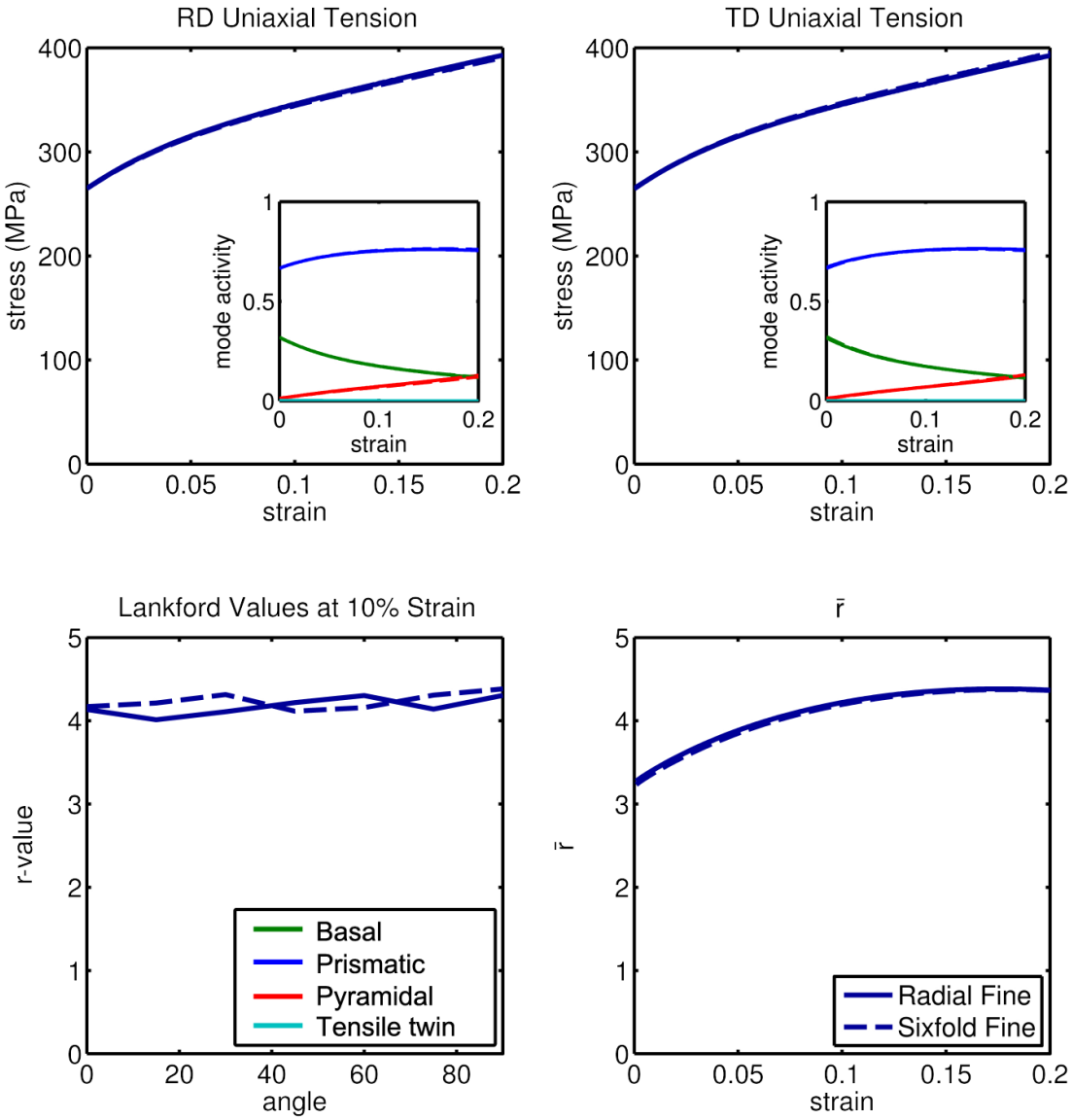

Figure 6.8: Effect of prismatic plane distribution on plastic deformation. Reprinted with permission from Reference [113].

axis and the sheet normal direction). This geometric trade off is the underlying reason for the strong sensitivity of r-value to the peak intensity in the basal pole figure and the dominance of this effect over those arising from the prismatic pole distribution or asymmetry of the basal peak shape.

Additionally, the observed insensitivity to the in-plane orientation of prismatic planes is in contrast to the results of the single crystal experiments performed by Kelley and Hosford [150]. That study examined the deformation behavior of Mg-4wt%Li in plane strain compression with the compression axis parallel to $\langle 10\bar{1}0\rangle$ versus $\langle 1\bar{2}10\rangle$ and constraint along the c-axis, both configurations to promote prismatic slip. Those authors found that the differences in a-axis orientation resulted in substantially different strain hardening behavior as a result of differences in geometric hardening caused by the lattice rotation during deformation. In the present polycrystal work, these differences in geometric hardening behavior are not observed, likely because of the effect of averaging a large number of grains. Comparison with the later polycrystal results of the authors [54] is not possible because only the basal pole figures are reported.

To summarize, the effect of texture on forming behavior is dominated by the strength of the basal peak, with the distribution of prismatic planes and basal peak symmetry having only weak effects. Textures with high basal intensity deform with large amounts of prismatic slip, resulting in high r-values and poor

forming behavior. The effects of prismatic plane distribution are largely averaged out by polycrystal effects. While asymmetry of the basal peak does result in differences in forming behavior, the strength of the peak remains the strongest effect.

6.3 Varied twin strength

As discussed in Section 1.1, the propensity for twinning in Mg alloys is frequently reported to be grain size dependent, especially in the fine grained regime as twinning is partially or completely suppressed. As twinning affects both the texture evolution as well as the dependence on basal versus non-basal slip modes, it will greatly influence formability. To phenomenologically examine this dependence of formability on grain size, the CRSS required for tensile twinning was varied (Table 6.3) while the hardening parameters for slip remained constant and the resulting formability was analyzed. The comparison of varied CRSS for twinning was conducted for a weak basal texture, varied symmetry of the basal peak, and varied symmetry of the prismatic pole figure; however, the observed effects were similar in all cases. Only the case of a high basal peak asymmetry is presented, because the effect is most easily observed.

The deformation behavior for material with a strongly asymmetrical basal

peak is presented in Figure 6.10. In tension along the RD, the small range of c-axis tilts inhibits the twin activity, so the stress-strain response and slip activity is nearly identical for all three effective grain sizes. However, in deformation along the TD the broader spread in c-axis orientation allows for increased twin activation. With increasing effective grain size (and consequently increased propensity for twinning), the flow stress at yield decreases, but increases rapidly as twinning is exhausted. At strains greater than 8%, increasing grain size results in increased flow stresses.

The texture evolution in TD tension to 20% elongation as a function of grain size is presented in Figure 6.9. TD spreading and RD splitting of the basal peak is observed, and coarser effective grain sizes promote the retention of TD spread during deformation.

The r-values for all sheet plane orientations increase for coarser grain sizes, however the *variation* in r-values is smaller for the coarser grains. The r-values of the coarse-grained material also evolve more rapidly with strain. Both of these effects may be attributed to the rapid texture evolution caused by twinning when compared to texture evolution by slip alone.

To summarize, altering the effective grain size by changing the propensity for twinning produces substantial differences in predicted formability. Coarse-

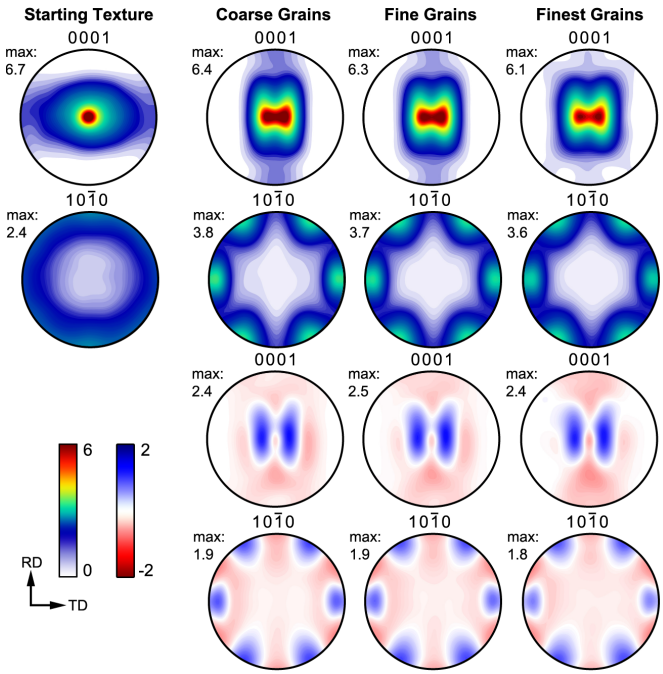

Figure 6.9: Effect of propensity for twinning on texture evolution. Reprinted with permission from Reference [113].

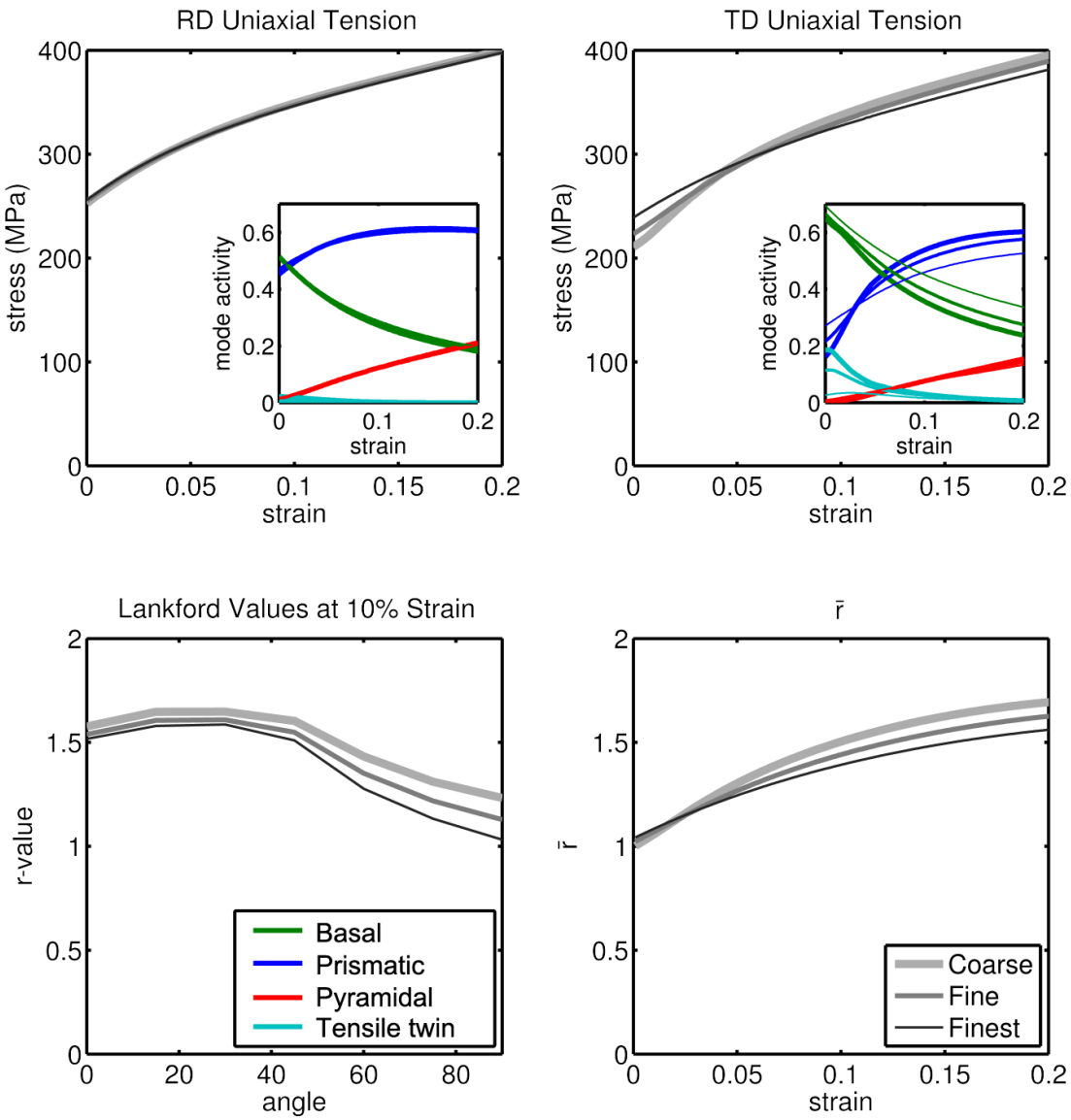

Figure 6.10: Effect of propensity for twinning on plastic deformation. Reprinted with permission from Reference [113].

grained material demonstrated reduced formability because of the increased dependence on prismatic slip after reorientation of the grains by twinning. This offers an alternative explanation for the commonly-reported observation that fine-grained magnesium materials have improved formability.

The conventional argument for enhanced formability is the activation of non-basal slip systems due to grain boundary constraint (e.g. [8, 14, 139]). Many of these studies have relied on transmission electron microscopy (TEM) studies of deformation mode activity performed at low strains. The simulations in the present work show that, while the fine-grained material does exhibit enhanced non-basal (prismatic) slip at low strains, it is not the underlying reason for enhanced formability. In the current study, the enhanced formability with decreasing grain size is the result of the continuing availability of basal slip as strain increases, instead of the observed rapid transition to dominant prismatic slip when twinning is exhausted in coarse grained materials. This effect would be challenging to identify experimentally via TEM due to the difficulty of imaging highly deformed material.

6.4 The importance of prismatic slip activity

The results of this work strongly suggest that poor formability, as predicted by high simulated r-values, is correlated with strong activity of prismatic slip after intermediate and high strains. However, the desirability of prismatic slip for forming behavior is disputed in the literature. This is largely because magnesium material that exhibits high elongation to failure in uniaxial tensile tests does not necessarily exhibit good formability [8].

Alloying and thermomechanical processing may be used to alter the balance between deformation modes, tailoring the mechanical properties. Many common solute strengthening additions for magnesium alloys, including Al and Zn, are reported to soften prismatic slip while hardening against basal slip, effectively reducing the basal:prismatic CRSS ratio [17, 20, 21, 61]. The present results show that this solute effect may or may not be desirable, depending on the grain size range at which the material will be used.

Above the solubility limit, different alloying elements will form precipitates of different morphologies [3] (e.g. plates on prismatic versus basal planes or c-axis rods). These precipitate morphologies have different strengthening effects on each deformation mode based on their likelihood of interaction with particular types of dislocations or twins [70, 71]. Additionally, both solute and

precipitate strengthening effects will be temperature sensitive, as will the CRSS ratios themselves; however, examining the temperature sensitivity is beyond the scope of this work.

The presence or absence of prismatic dislocations during and following deformation may have additional implications for recrystallization behavior. Dogan *et al.* [151] report that greater prismatic slip activity is observed in AZ31 material that resists shear band formation during equal channel angular pressing, in comparison to material where profuse twinning leads to dynamic recrystallization, which in turn leads to shear band formation. These authors suggest, therefore, that prismatic slip is a desirable alternative to profuse twinning under these conditions. Hadorn *et al.* [66] discuss the possibility that populations of dislocations on two orthogonal slip systems, such as basal and prismatic systems, may give subgrains additional degrees of rotational freedom during recrystallization, leading to weakening of the basal texture, which would in turn enhance formability. The effects of shear band formation and dynamic recrystallization would not be be captured by the VPSC model considered in this work. However, the results presented in Chapter 4 suggest that dominance of prismatic slip promotes rapid recrystallization because of the ease of nucleation, as well as the retention of the basal texture during recrystallization. This indicates that prismatic slip is unlikely to be a favorable alternative, and activation of

pyramidal slip would be the necessary alternative.

In summary, room temperature formability as measured by r-values is strongly dependent on the relative activity of prismatic slip. Consequently, alloying and processing strategies aimed at enhancing room temperature formability should emphasize hardening prismatic slip relative to basal slip and retaining a fine grain size to inhibit tensile twinning, as the crystal reorientation caused by twinning results in subsequently enhanced prismatic slip activity.

6.5 Summary of polycrystal plasticity prediction of formability

The formability of magnesium alloys is predicted using r-values calculated via the VPSC polycrystal plasticity model. A range of texture characteristics are examined, and it is verified that basal peak strength is the most important predictor of formability by a wide margin. The effects of basal peak symmetry and prismatic pole figure symmetry are weak in comparison. Additionally, the impact of the strength of the tension twinning mode (as an analog for grain size) on r-values is investigated. Material which requires greater stress to activate tension twinning (corresponding to a finer grain size) is observed to have lower

r-values, suggesting improved forming behavior. In all investigated cases, material with a greater reliance on prismatic slip to accommodate deformation is predicted to have poorer forming characteristics.

Table 6.2: Synthetic microstructure generation DREAM.3D pipeline

Filter #	Filter Name	Filter Purpose
1	Read DREAM.3D Data File	Load goal statistics created by Stats Generator
2	Initialize Synthetic Volume	Create empty volume
3	Establish Shape Types	Assigns shape type (ellipsoid) to grains
4	Pack Primary Phases	Generates individual grains inside empty volume
5	Find Feature Neighbors	Determines number and identity of neighbors for each grain
6	Match Crystallography	Assigns orientations to match orientation density function (ODF)
7	Generate IPF Colors	Generates inverse pole figure colors for each grain
8	Write DREAM.3D Data File	Writes all microstructure attributes to DREAM.3D data file
9	Write Los Alamos FFT File	Writes text file containing voxel locations and orientations

Table 6.3: Voce hardening parameters utilized for twinning as an analog for varied grain size. Hardening parameters for slip remain unchanged from Table 6.1.

		τ_0 (MPa)	τ_1 (MPa)	θ_0	θ_1	Note
tensile twin	$\{10\bar{1}2\}\langle\bar{1}011\rangle$	200	0	100	30	"finest grains"
		110	0	100	30	"fine grains," matched with TTMP AZ61L
		70	0	100	30	"coarse grains"

Chapter 7

Conclusions and Recommendations for Future Work

7.1 Summary and conclusions

Increased use of magnesium alloy sheet is desired in transportation and other applications where low component weight is an important concern. However, one substantial barrier which has inhibited further application of wrought magnesium product is the limited formability near room temperature. The primary factor limiting room temperature formability is the rapid development of a strong crystallographic texture during deformation processing and the persis-

tence of this texture during subsequent thermal processing steps. This strong texture results in insufficient availability of easy deformation mechanisms during forming, leading to fracture-limited forming behavior even at low strains.

Many studies have sought to modify the texture evolution of magnesium alloys, with the most successful efforts including alloying with RE and alkaline earth elements [3]. Proposed mechanisms for the improved texture evolution and mechanical behavior include modification of relative CRSS values, changes in the character of shear bands, and production of a new texture component during recrystallization. However, most of these studies have utilized alloy elements that have exceedingly low solubility in magnesium, resulting in the unintended formation of intermetallic particles. This has lead to convolution of solute effects with the effects of intermetallic particles. The other issue with many of the RE-containing alloys is that the necessary alloy elements are both very expensive and at critical or near-critical supply risk [3].

The objective of this work has been to isolate the effect of intermetallic particles and explore the potential for texture modification in RE-free magnesium alloys. The hypothesis was that the effects of solute and intermetallic particles are separate, and may both be independently exploited to alter processing textures even in a conventional alloy and process window. Texture evolution during deformation and subsequent static recrystallization were first isolated in a

set of binary two phase Mg-Zn alloys with varied Zn content. These investigated effects were also observed to be active in a commercial alkaline earth containing alloy, AXJ810. Finally, the viscoplastic self-consistent polycrystal plasticity model was utilized to investigate the importance of various texture characteristics and the strength of the tensile twinning mode on formability.

During deformation, coarse intermetallic particles were observed to have several possible effects dependent on their distribution. Very large inhomogeneously distributed intermetallic particles were only effective at modifying texture during large strain deformation. Under those deformation conditions, VPSC polycrystal plasticity simulations suggest that particles may have reduced the crystal rotation of the neighboring grains. This resulted in greater retention of TD tilted orientations and reduction in basal peak intensity. During rolling to intermediate strains, the particle stabilization effect of the inhomogeneous distribution was demonstrated to be negligible.

Conversely, the highly homogeneous distribution of coarse intermetallic particles present in thixomolded AXJ810 was highly effective in modifying the deformation texture during uniaxial compression due to the greater fraction of the deforming α-Mg which fell in the particle deformation zone. This led to a more diffuse deformation texture, which persisted through recrystallization.

Recrystallization kinetics in the binary Mg-Zn alloys were found to be highly sensitive to to the recrystallization temperature, with lower temperatures resulting in substantially stronger basal textures with less retained TD spread. Calculated JMAK exponents did not vary significantly with varied Zn content, but decreased with decreasing recrystallization temperature. This indicates that lower heat treatment temperatures result in greater spatial and temporal inhomogeneity during recrystallization.

Microstructural investigation of the 9wt% Zn alloy revealed that grains with off-basal orientations recrystallize substantially after basal grains, with the delay most substantial at lower temperatures. The slower-recrystallizing grains tend to be consumed by the basal recrystallization front, leasing to the observed texture strengthening. Measures of intragranular misorientation suggest no difference in stored deformation energy, but TEM reveals differences in dislocation substructure development. Basal grains contain multiple non-parallel dislocation walls due to the predominance of prismatic slip, allowing for efficient nucleus formation. Conversely, off-basal grains contain only a single population of parallel walls composed of basal dislocations, leading to inefficient nucleation of recrystallization.

Additionally, the presence of a population of approximately 100nm diameter spherical intermetallic particles in the binary Mg-Zn alloys effectively restricted

the grain size during recrystallization, preventing texture strengthening as a result of grain growth. This effect was also observe in the commercial AXJ810 alloy, where the presence of externally solidified grains allowed side-by-side comparison of the recrystallization behavior of particle-free and particle-rich regions. In this alloy, the particle-free regions initially recrystallized to a fine grain size with a weaker texture, but subsequently underwent grain growth and simultaneous texture strengthening.

Comparison of the recrystallization kinetics of AXJ810 and the binary Mg-Zn alloys also highlights the importance of a homogeneous particle distribution for alteration of recrystallization kinetics. In the binary Mg-Zn alloys, increasing the fraction of coarse intermetallic particles had no effect on the JMAK exponent; however, in the particle-containing AXJ810 microstructures recrystallization was accelerated in comparison to the solution treated material. Again, this likely results from a greater fraction of material within particle deformation zones with a homogeneous distribution of particles. This particle-induced acceleration of recrystallization may have a similar texture weakening effect to increased recrystallization temperature.

The experiments utilizing the AXJ810 alloy also highlight the beneficial effect of inexpensive alkaline earth alloy elements for solute modification of slip character during deformation. The solute effects are highly complementary to

the intermetallic particle effects and may be utilized in tandem.

Finally, the viscoplastic self-consistent polycrystal plasticity model was utilized to investigate the importance of observed texture characteristics for formability as reflected by material r-values. Of all the texture characteristics examined, basal peak strength is the most important by a substantial margin. However, in all cases textures which require greater prismatic slip activity in r-value tests are predicted to have poorer forming behavior.

Additionally, the strength of the tensile twinning deformation mode was varied within the VPSC model as an analog for material grain size, as material with finer grains is frequently reported to twin less. Material with easier twin activation (i.e. a coarser effective grain size) was observed to rely more heavily on prismatic slip in r-value tests after twinning reoriented the crystal, leading to predicted r-values which suggest poorer formability.

Throughout this work, the importance of a fine homogeneous microstructure with a substantial fraction of intermetallic particles is developing a weakly-textured formable wrought magnesium product is highlighted. This fine homogeneous microstructure leads to a more diffuse deformation texture and prevents texture strengthening during grain growth post-recrystallization. Additionally, the importance of restricting the activity of prismatic slip is highlighted.

Reliance on prismatic slip during deformation leads to r-values suggesting poor formability. Additionally, prismatic dislocation substructure led to rapid recrystallization of basal orientations, leading to stronger recrystallization textures. This restriction of prismatic slip may be accomplished by the addition of alloying elements which modify relative slip activities.

7.2 Recommendations for future work

While this research clearly identifies several opportunities for alloy and process design for enhanced formability in RE-free magnesium alloys, many unanswered questions remain. The following future work is recommended:

- *Characterization of homogeneity of particle distributions and effects on microstructural evolution.* The distribution of intermetallic particles in both the Mg-Zn alloys and AXJ810 is non-uniform. In the Mg-Zn alloys, the very coarse particles are aligned in stringers which do not have a uniform distribution through the material cross section. Additionally, the fine Mg-Zn intermetallic particles have substantial variations in spatial frequency, which would lead to some regions of material subjected to different particle hardening. The presence of "hard" and "soft" material regions may affect plasticity and texture evolution. In the thixomolded AXJ810, the

presence of the externally solidified grains creates regions which do not contain intermetallic particles and have been demonstrated to undergo less desirable microstructural evolution than the particle-containing matrix. Understanding the macroscopic effects of the presence of these spatial variations in particle distribution on mechanical behavior is critical prior to the implementation of these materials.

The effects of particle inhomogeneity could easily be probed by thixomolding specimens with varied fraction of externally solidified grains, then recrystallizing the material to a fine uniform grain size. The macroscopic mechanical behavior could be compared with more local measures of deformation behavior, such as micro- or nanoindentation. Similarly, the classic Beck experiment [152] could be utilized to examine the differences in recrystallization behavior with spatial variation in particle distribution.

- *Additional mechanical testing.* This work relied heavily on small-scale uniaxial compression tests and polycrystal plasticity simulations to examine mechanical behavior, largely because of the small specimen sizes. Production of larger specimens would enable larger scale mechanical testing. Of particular interest are uniaxial tensile tests where r-values are calculated, which would provide valuable validation of the predicted mechanical behavior. If very specimens were produced, true Erichsen formability exper-

iments could be conducted.

- *"Pinning" effect in the 9wt%Zn alloy.* While the CRSS ratios and post-yield hardening parameters were identical for the Mg-Zn binary alloys, the absolute magnitude of the CRSS values varied by almost 50%. This is too high to be explained by the increased fraction of intermetallic particles alone. The reason for the observed increase in initial yield stress remains to be explained. The higher yield, but similar hardening behavior suggests that the initial stress to move the dislocations is higher, i.e. they are initially "pinned" in some manner.

- *Comparison of effects of coarse intergranular versus intragranular intermetallic particles.* The majority of PSN literature examining the formation of particle deformation zones utilized alloys which contained coarse intragraunular particles, in contrast to the coarse grain boundary particles observed in the alloys used in these studies. In addition to the complications presented by the presence of multiple crystal orientations, the presence of a grain boundary will provide an additional source and sink for dislocations and may alter the nature of particle deformation zone produced. This effect would be best studied via crystal plasticity finite element modeling.

- *Optimization of alloy composition.* In this work, it was demonstrated that

even in simple binary Mg-Zn alloys opportunities for texture modification exist. However, the AXJ810 results clearly show that the texture modification by intermetallic particles can be greatly complemented by solute additions, particularly alkaline earth elements. Other alloy additions, such as Zr, are potent grain refiners [3] and may enable the use of conventional die casting. The Mg-Zn-Ca-Zr alloy space in particular is very promising, and avoids the use of RE elements.

- *Further TEM investigation of substructure development.* While the differences in substructure evolution between basal grains and off-basal grains was demonstrated, further details remain to be clarified. Outstanding questions of substructure development include the role of $\langle c + a \rangle$ dislocations and the interactions between basal and prismatic dislocations during low angle boundary formation.

- *Clarify the interaction of intermetallic particles and twinning.* While the possible interactions between intermetallic particles and dislocations are relatively well-defined, the possible interactions between intermetallic particles and twins are less clear. During twin propagation, the harder particles are likely to alter the local elastic stress field and may impede the propagation of the twin across the grain. During twin thickening, the fine

particles also likely impede the twin expansion by physically pinning the moving boundary. Finally, coarse intermetallic particles present at grain boundaries are less able to accommodate the local strain associated with a twin. This may lead to particle fracture or may prevent the nucleation of an accommodation twin in the adjacent grain. Which, if any, of these mechanisms are active remains to be clarified.

- *Temperature effects on deformation.* While the ultimate goal is to produce magnesium sheet with room temperature formability, the production pathway for that sheet will almost certainly include elevated temperature deformation processing. Hence, the dependence of texture evolution on deformation temperature should be more clearly explored. This will be particularly important in particle-containing alloys, because the dislocation-particle and twin-particle interactions will likely be thermally activated.

- *A holistic approach to alloy and process design.* One of the major conclusions of this study is that the addition of intermetallic particles is an effective strategy for improving the texture evolution during thermomechanical processing, resulting in improved plastic deformation characteristics. However, the impact of introducing these intermetallic particles on other important aspects of material performance (e.g. creep, fatigue, and cor-

rosion) must be carefully considered before this material design strategy may be implemented.

Bibliography

[1] Pandat with PanMagneisum database, 2008.

[2] W. J. Joost. Reducing Vehicle Weight and Improving U.S. Energy Efficiency Using Integrated Computational Materials Engineering. *JOM*, August 2012.

[3] I. Polmear. *Light Alloys: From Traditional Alloys to Nanocrystals*. Butterworth-Heinemann, Burlington, MA, 4 edition, 2006.

[4] K. Y. Xie, Z. Alam, A. Caffee, and K. J. Hemker. Pyramidal I slip in c-axis compressed Mg single crystals. *Scripta Materialia*, 112:75–78, February 2016.

[5] K. Hantzsche, J. Bohlen, J. Wendt, K. Kainer, S. Yi, and D. Letzig. Effect of rare earth additions on microstructure and texture development of magnesium alloy sheets. *Scripta Materialia*, 63(7):725–730, October 2010.

[6] I. Basu and T. Al-Samman. Twin recrystallization mechanisms in magnesium-rare earth alloys. *Acta Materialia*, 96:111–132, September 2015.

[7] N. Stanford and M. Barnett. The origin of "rare earth" texture development in extruded Mg-based alloys and its effect on tensile ductility. *Materials Science and Engineering: A*, 496(1-2):399–408, November 2008.

[8] S. R. Agnew and Ö. Duygulu. Plastic anisotropy and the role of non-basal slip in magnesium alloy AZ31b. *International Journal of Plasticity*, 21(6):1161–1193, June 2005.

[9] B. Bhattacharya and M. Niewczas. Work-hardening behaviour of Mg single crystals oriented for basal slip. *Philosophical Magazine*, 91(17):2227–2247, June 2011.

[10] H. Yoshinaga and R. Horiuchi. Deformation Mechanisms in Mg single crystals compressed in the direction parallel to hexagonal axis. *Transactions of the Japan Institute of Metals*, 4:1–8, 1963.

[11] R. E. Reed-Hill and W. D. Robertson. Deformation of Magnesium single crystals by nonbasal slip. *Journal of Metals Transactions AIME*, 220:496–502, 1957.

[12] A. Couret and D. Caillard. An in situ study of prismatic glide in magnesium—II. Microscopic activation parameters. *Acta Metallurgica*, 33(8):1455–1462, 1985.

[13] W. Hutchinson and M. Barnett. Effective values of critical resolved shear stress for slip in polycrystalline magnesium and other hcp metals. *Scripta Materialia*, 63(7):737–740, October 2010.

[14] J. Koike, T. Kobayashi, T. Mukai, H. Watanabe, M. Suzuki, K. Maruyama, and K. Higashi. The activity of non-basal slip systems and dynamic recovery at room temperature in fine-grained AZ31b magnesium alloys. *Acta materialia*, 51(7):2055–2065, 2003.

[15] J. Koike and R. Ohyama. Geometrical criterion for the activation of prismatic slip in AZ61 Mg alloy sheets deformed at room temperature. *Acta Materialia*, 53(7):1963–1972, April 2005.

[16] S. R. Agnew. Plastic Anisotropy of Magnesium Alloy AZ31b Sheet. In *Magnesium Technology 2002*, pages 351–356, 2002.

[17] N. Stanford and M. Barnett. Solute strengthening of prismatic slip, basal slip and twinning in Mg and Mg–Zn binary alloys. *International Journal of Plasticity*, 47:165–181, August 2013.

[18] B. Raeisinia and S. R. Agnew. Using polycrystal plasticity modeling to determine the effects of grain size and solid solution additions on in-

dividual deformation mechanisms in cast Mg alloys. *Scripta Materialia*, 63(7):731–736, October 2010.

[19] S. R. Agnew, M. H. Yoo, and C. N. Tome. Application of texture simulation to understanding mechanical behavior of Mg and solid solution alloys containing Li or Y. *Acta Materialia*, 49(20):4277–4289, 2001.

[20] A. Akhtar and E. Teghtsoonian. Solid solution strengthening of magnesium single crystals - I. Alloying behaviour in basal slip. *Acta Metallurgica*, 17:1339–1349, 1969.

[21] A. Akhtar and E. Teghtsoonian. Solid Solution Strengthening of Magnesium Single Crystals-II The Effect of Solute on the Ease of Prismatic Slip. *Acta Metallurgica*, 17:1351–1356, 1969.

[22] A. Couret and D. Caillard. An in situ study of prismatic glide in magnesium—I. The rate controlling mechanism. *Acta Metallurgica*, 33(8):1447–1454, 1985.

[23] T. Obara, H. Yoshinga, and S. Morozumi. {11-22}<11-23> Slip system in magnesium. *Acta Metallurgica*, 21(7):845–853, 1973.

[24] B. Raeisinia, S. R. Agnew, and A. Akhtar. Incorporation of Solid Solution Alloying Effects into Polycrystal Modeling of Mg Alloys. *Metallurgical and Materials Transactions A*, 42(5):1418–1430, May 2011.

[25] C. Cepeda-Jiménez, J. Molina-Aldareguia, and M. Pérez-Prado. Origin of the twinning to slip transition with grain size refinement, with decreasing strain rate and with increasing temperature in magnesium. *Acta Materialia*, 88:232–244, April 2015.

[26] M. Barnett, Z. Keshavarz, A. Beer, and D. Atwell. Influence of grain size on the compressive deformation of wrought Mg–3Al–1Zn. *Acta Materialia*, 52(17):5093–5103, October 2004.

[27] P. Dobroň, F. Chmelík, S. Yi, K. Parfenenko, D. Letzig, and J. Bohlen. Grain size effects on deformation twinning in an extruded magnesium alloy tested in compression. *Scripta Materialia*, 65(5):424–427, September 2011.

[28] H. Asgari, J. Szpunar, A. Odeshi, L. Zeng, and E. Olsson. Effect of grain size on high strain rate deformation of rolled Mg–4Y–3RE alloy in compression. *Materials Science and Engineering: A*, 633:92–102, May 2015.

[29] M. A. Meyers, O. Vöhringer, and V. A. Lubarda. The onset of twinning in metals: a constitutive description. *Acta materialia*, 49(19):4025–4039, 2001.

[30] R. Bhattacharya and B. P. Wynne. Hot working and crystallographic texture analysis of magnesium AZ alloys. *Materials Science and Technology*, 27(2):461–477, 2011.

[31] Z. Li, J. Dong, X. Q. Zeng, C. Lu, and W. J. Ding. Influence of Mg17al12 intermetallic compounds on the hot extruded microstructures and mechanical properties of Mg–9al–1zn alloy. *Materials Science and Engineering: A*, 466(1-2):134–139, September 2007.

[32] T. Al-Samman. Modification of texture and microstructure of magnesium alloy extrusions by particle-stimulated recrystallization. *Materials Science and Engineering: A*, 560:561–566, January 2013.

[33] X. Huang, K. Suzuki, and N. Saito. Textures and stretch formability of Mg–6Al–1Zn magnesium alloy sheets rolled at high temperatures up to 793K. *Scripta Materialia*, 60(8):651–654, April 2009.

[34] D. Wu, R. Chen, and E. Han. Excellent room-temperature ductility and formability of rolled Mg–Gd–Zn alloy sheets. *Journal of Alloys and Compounds*, 509(6):2856–2863, February 2011.

[35] Y. Chino, K. Sassa, and M. Mabuchi. Enhanced stretch formability of Mn-free AZ31 Mg alloy rolled by cross-roll rolling. *Journal of Materials Science*, 44(7):1821–1827, April 2009.

[36] X. Huang, K. Suzuki, Y. Chino, and M. Mabuchi. Improvement of stretch formability of Mg–3Al–1Zn alloy sheet by high temperature rolling at finishing pass. *Journal of Alloys and Compounds*, 509(28):7579–7584, July 2011.

[37] Y. Chino and M. Mabuchi. Enhanced stretch formability of Mg–Al–Zn alloy sheets rolled at high temperature (723k). *Scripta Materialia*, 60(6):447–450, March 2009.

[38] E. Yukutake, J. Kaneko, and M. Sugamata. Anisotropy and non-uniformity in plastic behavior of AZ31 magnesium alloy plates. *Materials Transactions*, 44(4):452–457, 2003.

[39] Y. Chino, H. Iwasaki, and M. Mabuchi. Stretch formability of AZ31 Mg alloy sheets at different testing temperatures. *Materials Science and Engineering: A*, 466(1-2):90–95, September 2007.

[40] X. Huang, K. Suzuki, A. Watazu, I. Shigematsu, and N. Saito. Improvement of formability of Mg–Al–Zn alloy sheet at low temperatures using differential speed rolling. *Journal of Alloys and Compounds*, 470(1-2):263–268, February 2009.

[41] H. Zhang, G. Huang, D. Kong, G. Sang, and B. Song. Influence of initial texture on formability of AZ31b magnesium alloy sheets at different temperatures. *Journal of Materials Processing Technology*, 211(10):1575–1580, October 2011.

[42] T. D. Berman, T. M. Pollock, and J. W. Jones. Texture, Second-Phase Particles, and the Anisotropy of Deformation Behavior in TTMP AZ61. *Metallurgical and Materials Transactions A*, 46(7):2986–2998, July 2015.

[43] W. Lankford, S. Snyder, and J. Bauscher. New criteria for predicting the press performance of deep drawing sheets. *Transactions of the American Society for Metals*, 42:1197–1232, 1950.

[44] W. Hosford. *The Mechanics of Crystals and Textured Polycrystals*. Number 32 in Oxford Engineering Science Series. Oxford University Press, New York, 1993.

[45] S.-H. Choi, J. C. Brem, F. Barlat, and K. H. Oh. Macroscopic anisotropy in AA5019a sheets. *Acta materialia*, 48(8):1853–1863, 2000.

[46] J. Bohlen, M. R. Nürnberg, J. W. Senn, D. Letzig, and S. R. Agnew. The texture and anisotropy of magnesium–zinc–rare earth alloy sheets. *Acta Materialia*, 55(6):2101–2112, April 2007.

[47] S. Agnew, J. Horton, T. Lillo, and D. Brown. Enhanced ductility in strongly textured magnesium produced by equal channel angular processing. *Scripta Materialia*, 50(3):377–381, February 2004.

[48] A. Hänzi, F. Dalla Torre, A. Sologubenko, P. Gunde, R. Schmid-Fetzer, M. Kuehlein, J. Löffler, and P. Uggowitzer. Design strategy for microalloyed ultra-ductile magnesium alloys. *Philosophical Magazine Letters*, 89:377–390, June 2009.

[49] A. Yamashita, Z. Horita, and T. G. Langdon. Improving the mechanical properties of magnesium and a magnesium alloy through severe plastic deformation. *Materials Science and Engineering: A*, 300(1):142–147, 2001.

[50] D. Raabe, P. Klose, B. Engl, K.-P. Imlau, F. Friedel, and F. Roters. Concepts for integrating plastic anisotropy into metal forming simulations. *Advanced Engineering Materials*, 4(4):169, 2002.

[51] R. Gehrmann, M. M. Frommert, and G. Gottstein. Texture effects on plastic deformation of magnesium. *Materials Science and Engineering: A*, 395(1-2):338–349, March 2005.

[52] N. Stanford, D. Atwell, A. Beer, C. Davies, and M. Barnett. Effect of microalloying with rare-earth elements on the texture of extruded magnesium-based alloys. *Scripta Materialia*, 59(7):772–775, October 2008.

[53] Y. Wang and H. Choo. Influence of texture on Hall–Petch relationships in an Mg alloy. *Acta Materialia*, 81:83–97, December 2014.

[54] E. Kelley and W. Hosford. The Deformation Characteristics of Textured Magnesium. *Transactions of the Metallurgical Society of AIME*, 242(4):654–661, 1968.

[55] S. Biswas, D.-I. Kim, and S. Suwas. Asymmetric and symmetric rolling of magnesium: Evolution of microstructure, texture and mechanical properties. *Materials Science and Engineering: A*, 550:19–30, July 2012.

[56] A. Ostapovets, P. Seda, A. Jager, and P. Lejcek. Characteristics of Coincident Site Lattice Grain Boudaries Developed During Equal Channel Angular Pressing of Magnesium Single Crystals. *Scripta Materialia*, 64:470–473, 2011.

[57] P. SEDÁ, S. MELZER, A. JÄGER, and P. LEJ\vCEK. INFLUENCE OF CRYSTAL ORIENTATION ON TEXTURE EVOLUTION OF MAGNESIUM SINGLE CRYSTALS AFTER ECAP PROCESSING.

[58] S. Biswas and S. Suwas. Evolution of sub-micron grain size and weak texture in magnesium alloy Mg–3al–0.4mn by a modified multi-axial forging process. *Scripta Materialia*, 66(2):89–92, January 2012.

[59] B. J. Bonarski, E. Schafler, B. Mingler, W. Skrotzki, B. Mikulowski, and M. J. Zehetbauer. Texture evolution of Mg during high-pressure torsion. *Journal of Materials Science*, 43(23-24):7513–7518, July 2008.

[60] J. A. Yasi, L. G. Hector, and D. R. Trinkle. First-principles data for solid-solution strengthening of magnesium: From geometry and chemistry to properties. *Acta Materialia*, 58(17):5704–5713, October 2010.

[61] H. Somekawa, M. Yamaguchi, Y. Osawa, A. Singh, M. Itakura, T. Tsuru, and T. Mukai. Material design for magnesium alloys with high deformability. *Philosophical Magazine*, 95(8):869–885, March 2015.

[62] M. Muzyk, Z. Pakiela, and K. Kurzydlowski. Generalized stacking fault energy in magnesium alloys: Density functional theory calculations. *Scripta Materialia*, 66(5):219–222, March 2012.

[63] T.-W. Fan, L.-G. Luo, L. Ma, B.-Y. Tang, L.-M. Peng, and W.-J. Ding. Effects of Zn atoms on the basal dislocation in magnesium solution from Peierls–Nabarro model. *Materials Science and Engineering: A*, 582:299–304, October 2013.

[64] C. Wang, H.-Y. Zhang, H.-Y. Wang, G.-J. Liu, and Q.-C. Jiang. Effects of doping atoms on the generalized stacking-fault energies of Mg alloys from first-principles calculations. *Scripta Materialia*, 69(6):445–448, September 2013.

[65] T. Al-Samman and X. Li. Sheet texture modification in magnesium-based alloys by selective rare earth alloying. *Materials Science and Engineering: A*, 528(10-11):3809–3822, April 2011.

[66] J. P. Hadorn, K. Hantzsche, S. Yi, J. Bohlen, D. Letzig, J. A. Wollmershauser, and S. R. Agnew. Role of Solute in the Texture Modification During Hot Deformation of Mg-Rare Earth Alloys. *Metallurgical and Materials Transactions A*, 43(4):1347–1362, October 2011.

[67] N. Stanford. Micro-alloying Mg with Y, Ce, Gd and La for texture modification—A comparative study. *Materials Science and Engineering: A*, 527(10-11):2669–2677, April 2010.

[68] N. Stanford and M. Barnett. Effect of composition on the texture and deformation behaviour of wrought Mg alloys. *Scripta Materialia*, 58(3):179–182, February 2008.

[69] I. Basu, T. Al-Samman, and G. Gottstein. Shear band-related recrystallization and grain growth in two rolled magnesium-rare earth alloys. *Materials Science and Engineering: A*, 579:50–56, September 2013.

[70] J. Nie. Effects of precipitate shape and orientation on dispersion strengthening in magnesium alloys. *Scripta Materialia*, 48:1009–1015, 2003.

[71] J. Robson, N. Stanford, and M. Barnett. Effect of precipitate shape on slip and twinning in magnesium alloys. *Acta Materialia*, 59(5):1945–1956, March 2011.

[72] T. D. Berman. *Microstructure Evolution and Tensile Deformation in Mg Alloy AZ61 Through Thixomolding and Thermomechanical Processing*. Doctoral Thesis, University of Michigan, Ann Arbor, 2014.

[73] J. Bhattacharyya, S. Agnew, and G. Muralidharan. Texture enhancement during grain growth of magnesium alloy AZ31b. *Acta Materialia*, 86:80–94, March 2015.

[74] M. R. Barnett, N. Stanford, P. Cizek, A. Beer, Z. Xuebin, and Z. Keshavarz. Deformation mechanisms in Mg alloys and the challenge of extending room-temperature plasticity. *Jom*, 61(8):19–24, 2009.

[75] C. Bettles and M. Gibson. Current wrought magnesium alloys: strengths and weaknesses. *Jom*, 57(5):46–49, 2005.

[76] A. Galiyev, R. Kaibyshev, and G. Gottstein. Correlation of plastic deformation and dynamic recrystallization in magnesium alloy ZK60. *Acta materialia*, 49(7):1199–1207, 2001.

[77] R. K. Nadella, I. Samajdar, and G. Gottstein. Static Recrystallisation and Textural Changes in Warm Rolled Pure Magnesium. In *Proceedings of the 6th International Conference on Magnesium Alloys and Their Apllications*, page 1052. Wiley-VCH Verlag GmbH & Co. KGaA, 2004.

[78] S. E. Ion, F. J. Humphreys, and S. H. White. Dynamic recrystallisation and the development of microstructure during the high temperature deformation of magnesium. *Acta Metallurgica*, 30(10):1909–1919, 1982.

[79] M. Barnett, A. Sullivan, N. Stanford, N. Ross, and A. Beer. Texture selection mechanisms in uniaxially extruded magnesium alloys. *Scripta Materialia*, 63(7):721–724, October 2010.

[80] P. Changizian, A. Zarei-Hanzaki, and H. R. Abedi. On the recrystallization behavior of homogenized AZ81 magnesium alloy: the effect of mechanical twins and< i> γ</i> precipitates. *Materials Science and Engineering: A*, 2012.

[81] M. Jiang, H. Yan, and R. Chen. Twinning, recrystallization and texture development during multi-directional impact forging in an AZ61 Mg alloy. *Journal of Alloys and Compounds*, 650:399–409, November 2015.

[82] E. Dogan, M. Vaughan, I. Karaman, G. Proust, G. Ayoub, and A. Benzerga. Microstructural Design of Mg Alloys for Lightweight Structural Applications. In *TMS Middle East - Mediterranean Materials Congress on Energy and Infrastructure Systems (MEMA 2015)*. John Wiley & Sons, Inc., 2015.

[83] J. W. Senn and S. R. Agnew. Texture randomization of magnesium alloys containing rare earth elements. In M. O. Pekguleryuz, N. R. Neelameggham, R. S. Beals, and E. A. Nyberg, editors, *Magnesium Technology*, pages 153–158. TMS (The Minerals, Metals & Materials Society), 2008.

[84] L. W. F. Mackenzie, B. Davis, F. J. Humphreys, and G. W. Lorimer. The deformation, recrystallisation and texture of three magnesium alloy extrusions. *Materials Science and Technology*, 23(10):1173–1180, October 2007.

[85] L. Mackenzie and M. Pekguleryuz. The influences of alloying additions and processing parameters on the rolling microstructures and textures of magnesium alloys. *Materials Science and Engineering: A*, 480(1-2):189–197, May 2008.

[86] E. Ball and P. Prangnell. Tensile-Compressive Yield Asymmetries in High Strength Wrought Magnesium Alloys. *Scripta Metallurgica et Materialia*, 31(2):111–116, 1994.

[87] J. Robson, D. Henry, and B. Davis. Particle effects on recrystallization in magnesium-manganese alloys: Particle-stimulated nucleation. *Acta Materialia*, 57(9):2739–2747, 2009.

[88] X. Yang, H. Miura, and T. Sakai. Dynamic Nucleation of New Grains in Magnesium Alloy during Hot Deformation. *Materials Science Forum*, 419-422:515–520, 2003.

[89] F. Humphreys and M. Hatherly. *Recrystallization and related annealing phenomena*. Pergamon, 2004.

[90] N. Stanford, I. Sabirov, G. Sha, A. La Fontaine, S. P. Ringer, and M. R. Barnett. Effect of Al and Gd Solutes on the Strain Rate Sensitivity of Magne-

sium Alloys. *Metallurgical and Materials Transactions A*, 41(3):734–743, January 2010.

[91] J. Bohlen, S. Yi, D. Letzig, and K. U. Kainer. Effect of rare earth elements on the microstructure and texture development in magnesium–manganese alloys during extrusion. *Materials Science and Engineering: A*, 527(26):7092–7098, October 2010.

[92] L. Mackenzie and M. Pekguleryuz. The recrystallization and texture of magnesium–zinc–cerium alloys. *Scripta Materialia*, 59(6):665–668, September 2008.

[93] J. P. Hadorn, K. Hantzsche, S. Yi, J. Bohlen, D. Letzig, and S. R. Agnew. Effects of Solute and Second-Phase Particles on the Texture of Nd-Containing Mg Alloys. *Metallurgical and Materials Transactions A*, 43(4):1363–1375, February 2012.

[94] F. J. Humphreys. The nucleation of recrystallization at second phase particles in deformed aluminium. *Acta metallurgica*, 25(11):1323–1344, 1977.

[95] V. M. Miller and T. M. Pollock. Recrystallization Behavior of a MgAlCa Alloy During Thermomechanical Processing and Subsequent Heat Treatment. *Magnesium Technology 2013*, page 205, 2013.

[96] V. M. Miller and T. M. Pollock. Texture Modification in a Magnesium-Aluminum-Calcium Alloy During Uniaxial Compression. *Metallurgical and Materials Transactions A*, 47(4):1854–1864, 2016.

[97] U. Köster. Recrystallization involving a second phase. *Metal Science*, 8(1):151–160, 1974.

[98] A. S. H. Kabir, J. Su, M. Sanjari, I. H. Jung, and S. Yue. Effect of Precipitation on Texture Evolution during Dynamic Recrystallization in Mg-Al-Sn Alloys. *Advanced Materials Research*, 922:304–309, May 2014.

[99] M. Pekguleryuz and A. Kaya. Creep Resistant Magnesium Alloys for Powertrain Applications. *Advanced Engineering Materials*, 5(12):866–878, December 2003.

[100] A. A. Luo, B. R. Powell, and M. P. Balogh. Creep and microstructure of magnesium-aluminum-calcium based alloys. *Metallurgical and Materials Transactions A*, 33(3):567–574, 2002.

[101] K. Hirai, H. Somekawa, Y. Takigawa, and K. Higashi. Effects of Ca and Sr addition on mechanical properties of a cast AZ91 magnesium alloy at room and elevated temperature. *Materials Science and Engineering: A*, 403(1-2):276–280, 2005.

[102] A. Suzuki, N. Saddock, J. Jones, and T. Pollock. Phase equilibria in the Mg- Al- Ca ternary system at 773 and 673 K. *Metallurgical and Materials Transactions A*, 37(12):975–983, 2006.

[103] A. Suzuki, N. Saddock, J. Jones, and T. Pollock. Structure and transition of eutectic (Mg, Al) 2ca Laves phase in a die-cast Mg-Al-Ca base alloy. *Scripta materialia*, 51(10):1005–1010, 2004.

[104] MATLAB Image Processing Toolbox Releasse R2015b.

[105] N. Otsu. A threshold selection method from gray-level histograms. *Automatica*, 11(285-296):23–27, 1975.

[106] F. Bachmann, R. Hielscher, and H. Schaeben. Texture Analysis with MTEX – Free and Open Source Software Toolbox. *Solid State Phenomena*, 160:63–68, February 2010.

[107] L. N. Brewer, D. P. Field, and C. C. Merriman. Mapping and assessing plastic deformation using EBSD. In *Electron Backscatter Diffraction in Materials Science*, pages 251–262. 2009.

[108] Y. B. Chun, M. Battaini, C. H. J. Davies, and S. K. Hwang. Distribution Characteristics of In-Grain Misorientation Axes in Cold-Rolled Commercially Pure Titanium and Their Correlation with Active Slip Modes. *Metallurgical and Materials Transactions A*, 41(13):3473–3487, October 2010.

[109] R. A. Lebensohn and C. Tomé. A self-consistent anisotropic approach for the simulation of plastic deformation and texture development of polycrytsals: application to zirconium alloys. *Acta Metallurgica et Materialia*, 41(9):2611–2624, 1993.

[110] C. N. Tomé. Self-consistent polycrystal models: a directional compliance criterion to describe grain interactions. *Modelling and Simulation in Materials Science and Engineering*, 7(5):723, 1999.

[111] C. N. Tome, G. Canova, U. Kocks, N. Christodoulou, and J. Jonas. The relation between macroscopic and microscopic strain hardening in F.C.C. polycrystals. *Acta Metallurgica*, 32(10):1637–1653, 1984.

[112] C. Tomé, R. A. Lebensohn, and U. Kocks. A model for texture development dominated by deformation twinning: applicatoin to zirconium Alloys. *Acta Metallurgica et Materialia*, 39(11):2667–2680, 1991.

[113] V. M. Miller, T. D. Berman, I. J. Beyerlein, J. W. Jones, and T. M. Pollock. Prediction of formability in magnesium alloys using a polycrystal plasticity model. *Materials Science and Engineering A*, Submitted, 2016.

[114] V. M. Miller, T. D. Berman, I. J. Beyerlein, and T. Pollock. Prediction of Formability in Magnesium Alloys: The Role of Texture. In *Magnesium Technology 2016*, volume Accepted, Nashville, TN, 2016. TMS (The Minerals, Metals & Materials Society).

[115] J. S. Carpenter, R. J. McCabe, S. J. Zheng, T. A. Wynn, N. A. Mara, and I. J. Beyerlein. Processing Parameter Influence on Texture and Microstructural Evolution in Cu-Nb Multilayer Composites Fabricated via Accumulative Roll Bonding. *Metallurgical and Materials Transactions A*, 45(4):2192–2208, April 2014.

[116] S. Li, I. J. Beyerlein, C. T. Necker, D. J. Alexander, and M. Bourke. Heterogeneity of deformation texture in equal channel angular extrusion of copper. *Acta Materialia*, 52(16):4859–4875, September 2004.

[117] S. Li, I. J. Beyerlein, D. J. Alexander, and S. C. Vogel. Texture evolution during equal channel angular extrusion: Effect of initial texture from experiment and simulation. *Scripta Materialia*, 52(11):1099–1104, June 2005.

[118] S. G. Vogel, D. J. Alexander, I. J. Beyerlein, M. A. Bourke, D. W. Brown, B. Clausen, C. Tomé, B. Von Dreele, C. Xu, and T. G. Langdon. Investi-

gation of texture in ECAP materials using neutron diffraction. *Materials Science Forum*, 426-432:2661–2665, 2003.

[119] S. C. Vogel, I. J. Beyerlein, M. A. Bourke, C. Tomé, P. Rangaswamy, C. Xu, and T. G. Langdon. Texture in equal-channel angular pressed aluminum and nickel. *Materials Science Forum*, 408-412:673–678, 2002.

[120] V. M. Miller, M. P. Echlin, I. J. Beyerlein, and T. M. Pollock. Polycrystal plasticity simulation of microtextured titanium. In *Titanium 2015*, volume Accepted, San Diego, CA, 2015. TMS (The Minerals, Metals & Materials Society).

[121] F. J. Humphreys. Local lattice rotations at second phase particles in deformed metals. *Acta Metallurgica*, 27(12):1801–1814, 1979.

[122] F. J. Humphreys and M. G. Ardakani. The deformation of particle-containing aluminium single crystals. *Acta metallurgica et materialia*, 42(3):749–761, 1994.

[123] F. J. Humphreys and P. N. Kalu. The plasticity of particle-containing polycrystals. *Acta Metallurgica et Materialia*, 38(6):917–930, 1990.

[124] C. Schäfer, J. Song, and G. Gottstein. Modeling of texture evolution in the deformation zone of second-phase particles. *Acta Materialia*, 57(4):1026–1034, February 2009.

[125] R. A. Vandermeer and P. Gordon. The influence of recovery on recrystallization in aluminum. Technical report, DTIC Document, 1962.

[126] M. Luton, R. Petkovic, and J. J. Jonas. Kinetics of recovery and recrystallization in polycrystalline copper.

[127] A. Rosen, M. Burton, and G. Smith. Recrystallization of high-purity iron. *Trans. Metall. Soc. A.I.M.E.*, 230(1):205, 1964.

[128] N. Hansen, T. Leffers, and J. K. Kjems. Recrystallization kinetics in copper investigated by in situ texture measurements by neutron diffraction. *Acta Metallurgica*, 29(8):1523–1533, 1981.

[129] R. A. Vandermeer and B. B. Rath. Modeling recystallization kinetics in a deformed iron single crystal. *Metallurgical Transactions A*, 20(3):391–401, 1989.

[130] C. Smith. *Trans. Metall. Soc. A.I.M.E.*, 175:15, 1948.

[131] P. Manohar, M. Ferry, and T. Chandra. Five Decades of the Zener Equation. *ISIJ International*, 38(9):913–924, 1998.

[132] T. D. Berman, W. Donlon, V. M. Miller, R. Decker, J. Huang, T. M. Pollock, and J. W. Jones. MICROSTRUCTURE MODIFICATION AND DEFORMATION BEHAVIOR OF FINE GRAINED AZ61l SHEET PRODUCED BY THIXOMOLDING® AND THERMOMECHANICAL PROCESSING. *Magnesium Technology 2012 w/CD*, page 339, 2012.

[133] T. D. Berman, W. Donlon, C. Hung, P. Milligan, R. Decker, T. M. Pollock, and J. W. Jones. Microstructure Characterization of Weakly Textured and Fine Grained AZ61 Sheet. In *Magnesium Technology 2013*, page 113. TMS (The Minerals, Metals & Materials Society), 2013.

[134] N. Stanford. The effect of calcium on the texture, microstructure and mechanical properties of extruded Mg–Mn–Ca alloys. *Materials Science and Engineering: A*, 528(1):314–322, November 2010.

[135] T. Wang, L. Jiang, R. K. Mishra, and J. J. Jonas. Effect of Ca Addition on the Intensity of the Rare Earth Texture Component in Extruded Magnesium Alloys. *Metallurgical and Materials Transactions A*, 45(10):4698–4709, September 2014.

[136] J. Bohlen, J. Wendt, M. Nienaber, K. U. Kainer, L. Stutz, and D. Letzig. Calcium and zirconium as texture modifiers during rolling and annealing of magnesium–zinc alloys. *Materials Characterization*, 101:144–152, March 2015.

[137] S. Sandlöbes, M. Friák, S. Zaefferer, A. Dick, S. Yi, D. Letzig, Z. Pei, L.-F. Zhu, J. Neugebauer, and D. Raabe. The relation between ductility and stacking fault energies in Mg and Mg–Y alloys. *Acta Materialia*, 60(6-7):3011–3021, April 2012.

[138] N. Stanford, G. Sha, J. Xia, S. Ringer, and M. Barnett. Solute segregation and texture modification in an extruded magnesium alloy containing gadolinium. *Scripta Materialia*, 65(10):919–921, November 2011.

[139] S. Sandlöbes, S. Zaefferer, I. Schestakow, S. Yi, and R. Gonzalez-Martinez. On the role of non-basal deformation mechanisms for the ductility of Mg and Mg–Y alloys. *Acta Materialia*, 59(2):429–439, January 2011.

[140] A. Urakami and M. Fine. urakami fine yield drop effects for basal and prismatic slip.pdf. *Acta Metallurgica*, 19:887–894, 1971.

[141] A. Sato and M. Meshii. Solid solution softening and solid solution hardening. *Acta Metallurgica*, 21(6):753–768, 1973.

[142] O. Engler. Influence of Particle Stimulated Nucleation on the Recrystallization Textures in Cold Deformed Al Alloys Part II-Modelling of Recrystallization Textures. *Scripta Materialia*, 37(11):1675–1683, 1997.

[143] L. Delannay, M. Melchior, J. Signorelli, J.-F. Remacle, and T. Kuwabara. Influence of grain shape on the planar anisotropy of rolled steel sheets – evaluation of three models. *Computational Materials Science*, 45(3):739–743, May 2009.

[144] G. Charca Ramos, M. Stout, R. Bolmaro, J. Signorelli, M. Serenelli, M. Bertinetti, and P. Turner. Study of a drawing-quality sheet steel. II: Forming-limit curves by experiments and micromechanical simulations. *International Journal of Solids and Structures*, 47(17):2294–2299, August 2010.

[145] H. Wang, P. Wu, K. Boyle, and K. Neale. On crystal plasticity formability analysis for magnesium alloy sheets. *International Journal of Solids and Structures*, 48(6):1000–1010, March 2011.

[146] J. Lévesque, K. Inal, K. Neale, and R. Mishra. Numerical modeling of formability of extruded magnesium alloy tubes. *International Journal of Plasticity*, 26(1):65–83, January 2010.

[147] C. Neil and S. R. Agnew. Crystal placicity-based formin limit prediction for non-cubic metals: Application to Mg alloy AZ31b. *International Journal of Plasticity*, 25:379–398, 2009.

[148] S. Li, I. J. Beyerlein, D. J. Alexander, and S. C. Vogel. Texture evolution during multi-pass equal channel angular extrusion of copper: Neutron diffraction characterization and polycrystal modeling. *Acta Materialia*, 53(7):2111–2125, April 2005.

[149] M. A. Groeber and M. A. Jackson. DREAM. 3d: a digital representation environment for the analysis of microstructure in 3d. *Integrating Materials and Manufacturing Innovation*, 3(1):1–17, 2014.

[150] E. Kelley and W. Hosford. Plane strain compression of Mg and Mg alloy single crystals. *Trans. Metall. Soc. A.I.M.E.*, 242(1):5–13, 1968.

[151] E. Dogan, M. Vaughan, S. Wang, I. Karaman, and G. Proust. Role of starting texture and deformation modes on low-temperature shear formability and shear localization of Mg–3Al–1Zn alloy. *Acta Materialia*, 89:408–422, May 2015.

[152] P. A. Beck, P. R. Sperry, and H. Hu. The Orientation Dependence of the Rate of Grain Boundary Migration. *Journal of Applied Physics*, 21(5):420, 1950.